Development of combined operando diagnostics

Applications in heterogeneous catalysis and electrochemistry

Rämisch, Lisa

2024

Document Version:
Publisher's PDF, also known as Version of record

Development of combined operando diagnostics

Applications in heterogeneous catalysis and electrochemistry

LISA RÄMISCH
DEPARTMENT OF PHYSICS | FACULTY OF ENGINEERING | LUND UNIVERSITY

Development of combined operando diagnostics

Development of combined operando diagnostics

Applications in heterogeneous catalysis and electrochemistry

by Lisa Rämisch

LUND
UNIVERSITY

Thesis for the degree of Doctor of Philosophy
Thesis advisors: Dr. Johan Zetterberg, Prof. Edvin Lundgren, Dr. Hampus Nilsson
Faculty opponent: Prof. Gareth Parkinson

To be presented, with the permission of the Faculty of Engineering of Lund University, for public criticism in the Rydberg lecture hall at the Department of Physics on Friday, the 26th of April 2024 at 09:15.

Organization
LUND UNIVERSITY

Department of Physics
Box 188
SE–221 00 LUND
Sweden

Author(s)
Lisa Rämisch

Document name
DOCTORAL DISSERTATION

Date of disputation
2024-04-26

Sponsoring organization

Title and subtitle
Development of combined operando diagnostics: Applications in heterogeneous catalysis and electrochemistry

Abstract
With the aim to bridge the pressure gap between traditional surface science and industrial applications, heterogeneous catalytic reactions on model catalysts are increasingly studied at near-ambient pressures. Under those conditions, the gas phase has been shown to play an important role during the interaction at the gas-surface interface making it complex to study. This complexity can be captured by simultaneously measuring different properties of the gas-surface interaction *operando* while the reaction takes place . Since each diagnostic tool offers unique information, combining them provides a fuller understanding of the reaction.

This thesis presents a combination of three laser- and optical-based *operando* techniques that have been combined in a versatile in-house setup. We have shown that planar laser-induced fluorescence (PLIF), two dimensional-surface optical reflectance (2D-SOR) and polarization modulation-infrared reflection absorption spectroscopy (PM-IRRAS) can be combined, either simultaneously or in various configurations, to study CO oxidation on different Pd-based model catalysts. Thereby, chemical and structural information about the surface and chemical information about the gas phase can be obtained in space and temporally resolved.

Moreover, some of the in-house optical techniques are combined with synchrotron-based techniques to extract more chemical and structural information than can be obtained from one measurement. This is demonstrated with simultaneous measurements combining PM-IRRAS and ambient pressure X-ray photoelectron spectroscopy (AP-XPS) for different gas-phase catalysis reactions and 2D-SOR combined with High Energy Surface X-ray Diffraction (HESXRD) for electrochemical studies.

Key words
Infrared Surface Spectroscopy, Planar Laser Induced Fluorescence, Surface Optical Reflectance, X-ray Photoelectron Spectroscopy, Ambient Pressure Heterogeneous Catalysis, CO oxidation, Operando Techniques

Classification system and/or index terms (if any)

Supplementary bibliographical information

Language
English

ISSN and key title

ISBN
978-91-8039-998-2 (print)
978-91-8039-999-9 (pdf)

Recipient's notes

Number of pages
268

Price

Security classification

Development of combined operando diagnostics

Applications in heterogeneous catalysis and electrochemistry

by Lisa Rämisch

LUND
UNIVERSITY

Cover illustration front: Impressionist adaptation of the combined AP-XPS and PM-IRRAS spectra and MS trends of CO oxidation on Pd(100) generated by *Deep Dream Generator*. The original data is found in section 5.1.2 in this thesis.

Cover illustration back: Blender illustration showing the combination of three optical- and laser-based signals on a single crystal surface adapted from the graphical abstract of paper III).

Funding information: This work was financially supported by the Knut and Alice Wallenberg foundation (KAW)-funded project "Atomistic design of new catalysts" (no. KAW 2015.0058) and the Swedish Foundation for Strategic Research (project no. ITM17-0045).

Faculty of Engineering, Department of Physics

ISBN: 978-91-8039-998-2 (print)
ISBN: 978-91-8039-999-9 (pdf)
LRCP: LRCP-253
ISSN: 1102 – 8718

Printed in Sweden by Media-Tryck, Lund University, Lund 2024

Dedicated to my parents
Karin and Gerald Rämisch

Contents

List of publications

I L. Rämisch, S.M. Gericke, S. Pfaff, E. Lundgren and J. Zetterberg. **Infrared surface spectroscopy and surface optical reflectance for operando catalyst surface characterization**. *Appl. Surf. Sci.*, **578**, 152048 (2022)

II S. Pfaff, L. Rämisch, S.M. Gericke, A. Larsson, E. Lundgren and J. Zetterberg. **Visualizing the Gas Diffusion Induced Ignition of a Catalytic Reaction**. *ACS Catal.*, **12**, 6589–6595 (2022)

III L. Rämisch, S. Pfaff, S.M. Gericke, E. Lundgren and J. Zetterberg. **Ambient pressure operando catalytic characterization by combining PM-IRRAS with planar laser-induced fluorescence and surface optical reflectance imaging**. *Cat. Tod.*(2024)

IV L. Rämisch, R. Temperton, S.M. Gericke, S. Pfaff, E. Lundgren, J. Zetterberg and F. García-Martínez. **Combined time-resolved Infrared and X-ray spectroscopic operando studies of NO reactions on Rh**(111). Manuscript in preparation.

V F. García-Martínez, L. Rämisch, K. Ali, I. Waluyo, R.C. Bodero, S. Pfaff, I.J. Villar-García, A.L. Walter, A. Hunt, V. Pérez-Dieste . **Structure Matters: Asymmetric CO Oxidation at Rh steps with Different Atomic Packing.**. *J. Am. Chem. Soc.*, **144**, 15363-15371 (2022)

VI S. Pfaff, A. Larsson, D. Orlov, G.S. Harlow, G. Abbondanza, W. Linpé, L. Rämisch, S.M. Gericke, J. Zetterberg and E. Lundgren. **Operando Reflectance Microscopy on Polycrystalline Surfaces in Thermal Catalysis, Electrocatalysis, and Corrosion.**. *ACS Appl. Mater. Interfaces*, **16**, 19530–19540 (2021)

VII S. Pfaff, A. Larsson, D. Orlov, L. Rämisch, S.M. Gericke, E. Lundgren and J. Zetterberg. **A Polycrystalline Pd Surface Studied by Two-Dimensional Surface Optical Reflectance during CO Oxidation: Bridging the Materials Gap**. *ACS Appl. Mater. Interfaces*, **16**, 444-453 (2024)

VIII C. Preger, L. Rämisch, S. Blomberg, J. Zetterberg, R. Westerström, M. Messing. **Magnetic-field-assisted nanochain formation of intermixed catalytic CoPd nanoparticles** . Manuscript submitted to *ACS Appl. Mater. Interfaces* on 2024-03-01.

IX W. Linpé, G.S. Harlow, A. Larsson, G.Abbondanza, **L.Rämisch**, S. Pfaff, J. zetterberg, J. Evertsson and E.Lundgren. **An electrochemical cell for 2-dimensional surface optical reflectance during anodizaion and cyclic voltammetry**. *Rev. Sci. Instrum.*, **91**, 044101 (2020)

X W. Linpé, **L. Rämisch**, G. Abbondanza, A. larsson, S. Pfaff, L. Jacobse, J. Zetterberg, L. Merte, A. Stierle, Z. Hegedues, U. Lienert, E. Lundgren and G.S. Harlow. **Revisiting Optical Reflectance from Au**(111) **Electrode Surfaces with Combined High-Energy Surface X-ray Diffraction**. *J. Electrochem. Soc.*, **168**, 096511 (2021)

Related Work

A A. Larsson, G. Abbondanza, L. Rämisch, W. Linpé, D.V. Novikov, E. Lundgren and G.S. Harlow. **In-situ scanning x-ray diffraction reveals strain variations in electrochemically grown nanowires**. *J. Phys. D: Appl. Phys.*, **54**, 235301 (2021)

B S.M. Gericke, M.M. Kauppinen, M. Wagner, M. Riva, G. Franceschi, A. Posada-Borbón, L. Rämisch, S. Pfaff, E. Rheinfrank, A.M. Imre, A.B. Preobrajenski, S. Appelfeller, S. Blomberg, L.R. Merte, J. Zetterberg, U. Diebold, H. Grönbeck, and E. Lundgren. **Effect of Different In_2O_3(111) Surface Terminations on CO_2 Adsorption**. *ACS Appl. Mater. Interfaces*, **15**, p. 45367-4537715 (2023)

Acknowledgements

Research and education is about the ”we” not the ”I”. Team work makes the dream work and the team behind this thesis needs to be acknowledged from top to bottom.

Firstmost, my main supervisor **Johan**. You have trusted me throughout my thesis to work independently. I hope that I could live up to your expectations because you definitely lived up to mine in terms of being a great supervisor! You were exactly what I was looking for, no micromanaging, social skills and always an open door with an opinion to be shared. A big life lesson you have given me is to present myself properly, professionally and comprehensively. If someone genuinely cares about the quality of education, it's you and that has definitely inspired me. Thanks for giving me all the opportunities to go to conferences, workshops and beamtimes.

Thank you **Edvin**, for always being so enthusiastic about my work, and being the joyful and knowledgeable person about surface science that you are. I am super happy and grateful that you organized afterworks and opened up doors for lots of collaborations. Thank you **Hampus** for sharing your IR knowledge and helping us to get going.

What were the odds of me ending up with a bunch of german. **Sebastian**, the times we performed experiments in the lab are one of the greatest memories of my PhD. I miss your enthusiasm. Your knowledge about IT and software development has helped me immensely throughout my PhD. **Sabrina**, no one can deny that you are an XPS expert. Thank you for opening up the synchrotron world to me and for being a german companion throughout my PhD. **Sam**, it never felt like you were new to the PhD world. I am impressed by your independence, speed of learning and your ease to take on new tasks.

The people connected to the **synchrotron division** made up an essential part of my work: Weronica, Giuseppe, Alfred, Andrea, Ulrike, Hanna, Estephania, Jan and Johan G. opened up for great collaborations. The **Hippie beamline**, Rob, Mattia and Andrey should be thanked for granting us in-house beamtime and letting us get started on the PM-IRRAS measurements, Dora and Harald, for sharing the SurfCAT summer school adventure, **Sara B.& Co.** that I got the chance to hang out with on beamtimes and collaborated with in a lot of ways.

There wasn't just one one dream team, but a lot of different ones. Thank you **Fernando** for being a work horse and incredibly fun to work with. **Calle**, after four years we did it, thanks for the glimpse at the nanoworld. **Jason** Weaver, thanks for being so enthusiastic and for letting me study other catalytic samples and reactions. I got the chance to collaborate with **Hilde** and **Ingeborg** from NTNU, both in the lab and at Max IV. Thanks for being inspiring female researchers. Thanks **Olaf Brummel** for letting me explore Erlangen and electrochemistry.

The people are at least half of the motivation why I come to work every day and I am happy to say that I didn't loose motivation until the end. The work environment at the division of **combustion physics** is unique, I would recommend it to anyone. It meant a lot to have such a welcoming atmosphere with a mix of nationalities giving me the opportunity to dust off my rusty chinese from time to time. There are so many colleagues to thank and I will make sure to all hand you a personal note. Some colleagues turned out to become close friends of mine and I am very thankful for that. You won't get rid of me that easily!

I studied physics because of my numerous inspiring middle-/high-school **Physics teachers**. They might never read this but still deserve to be mentioned: Frau Nordman, Herr Völker, Herr Wiegmann and Mr Sanjeev.

I want to thank my best friends **Vanessa**, **Luisa** and **Finja** for being solid rocks in my life since Kindergarten, my close friends in Lund for making me a pub quiz nerd and the **Rydbergs-gang** for adopting me into the world of Fysikum. Thanks to the joy of a few beers and a patient Daniel Persson, I started speaking swedish. I want to thank all my friends around the globe, from France to the Philippines, for your inspiration and support.

For several reasons, without the **Lugi Lions R.F.C.**, I would probably not have stayed in Lund. I know that wherever in the world I go, rugby will be like a second home! This team, sport and club have given me a community, lots of sisters, the best parties, a scheduled hobby and of course physical activity that I needed to ventilate my stress and get some dopamine!

Thank you **LAJF**, Lunds Akademiska Jaktförening and all its (board-)members, there are too many names to list. It has opened the world of hunting for me including friendships, lots of outdoor activities and great food.

Early on during my stay in Sweden, I was lucky to meet the most genuine, straight-forward person that I know. Thank you **Truls** for sharing all your abilities with me that I sometimes lack: Sarcasm, banter, extreme good general knowledge, love for your home region and a way to always "sudda bort min sura min". Lucky me, his mom **Marie** is the kindest person who always jumps in and helps out when needed. Tusen tack, Marie!

Last but not the least of all, I want to thank my family starting off with my grandparents **Marianne**, **Bärbel**, **Erhard** and **Hans-Joachim** (all still standing strong) for laying the ground work. Most importantly, I want to thank my parents, **Karin** und **Gerald**. I simply couldn't have wished for better parents. You supported me to go down my own road, believed in me and always gave me useful realistic advice. You're my biggest role models! I want to thank my siblings, **Sofie** and **Justus**, my soulmates, my band members, my left-handers, my smarter mini-mes. I am so proud of you and inspired by all the things you do!

Abstract

With the aim to bridge the pressure gap between traditional surface science and industrial applications, heterogeneous catalytic reactions on model catalysts are increasingly studied at near-ambient pressures. Under those conditions, the gas phase has been shown to play an important role during the interaction at the gas-surface interface making it complex to study. This complexity can be captured by simultaneously measuring different properties of the gas-surface interaction *operando* while the reaction takes place . Since each diagnostic tool offers unique information, combining them provides a fuller understanding of the reaction.

This thesis presents a combination of three laser- and optical-based *operando* techniques that have been combined in a versatile in-house setup. We have shown that planar laser-induced fluorescence (PLIF), two dimensional surface optical reflectance (2D-SOR) and polarization modulation-infrared reflection absorption spectroscopy (PM-IRRAS) can be combined, either simultaneously or in various configurations, to study CO oxidation on different Pd-based model catalysts. Thereby, chemical and structural information about the surface and chemical information about the gas phase can be obtained in space and temporally resolved.

Moreover, some of the in-house optical techniques are combined with synchrotron-based techniques to extract more chemical and structural information than can be obtained from one measurement. This is demonstrated with simultaneous measurements combining PM-IRRAS and ambient pressure X-ray photoelectron spectroscopy (AP-XPS) for different gas-phase catalysis reactions and 2D-SOR combined with High Energy Surface X-ray Diffraction (HESXRD) for electrochemical studies.

Popular summary in English

Most of us have heard about a catalyst converter in connection to combustion engine cars. Before the exhaust gases from the engine are blown into the air through the exhaust pipe, they pass by a catalyst converter that makes sure that the for us toxic gases like carbon monoxide get converted to a less poisonous gas, for example to CO_2: A process called CO oxidation. However, we are all aware that CO_2 is "poisonous" for the environment and a main contributor to climate change. Even here, catalysts can give an answer. Certain catalytic materials can convert CO_2 to for example methanol and other chemicals and thereby reduce CO_2 emissions. To produce better catalysts and more energy efficient catalytic reactions is therefore essential for a greener future. But before we produce better catalysts, we first need to understand how they work on a fundamental level. More specifically, how atoms and molecules interact with the catalyst.

A catalyst comes in the form of metallic nanoparticles. You can imagine these nanoparticles like an accumulation or a cluster of hundred to millions of atoms. They are arranged in a variety of surface structures, making these nanoparticles very complex to study. In order to obtain an in depth understanding on the level of single atoms and molecules, we can look at one such surface structure at a time. These so-called single crystal surfaces are less complex and only mimic the real industrial catalyst. They are therefore referred to as model catalysts.

During the catalytic reaction, gases interact with this model catalyst that comes in a metallic solid state form. Since two phases of matter are present here (gas, solid) and interact, we speak about a *hetero*geneous catalytic reaction. To shed light onto this reaction and study it, measurement techniques are required. There are two main challenges when measuring heterogeneous catalytic reaction that we address in this thesis: First of all, we want to understand the interaction at the model catalyst while the reaction takes place at close to atmospheric pressures in order to come as close to industrial conditions as possible. We need to therefore look at the catalyst while it is "at work" (*operando*), thus we require *operando* techniques. In the case of a car engine and exhaust, you could think of the catalyst being *operando* when the engine has been warmed up and is running. Secondly, since this interaction includes a surface, some gases and the interaction of the two, the aim is to retrieve as much information as possible from one single measurement about the surface and the gas. We want to capture how the large amount of gas molecules at higher pressure influences the surface and vice versa. Since this reaction is a dynamic process that varies with time, it is important to follow the reactions with time-resolved methods.

This thesis tries to answer the two challenges by presenting studies where several *operando* measurement techniques have been combined. A unique and compact lab setup has been developed where three optical- and laser-based techniques simultaneously study the same catalytic reaction. The studies are performed close to 1 bar, thus at near-ambient pressures.

We use laser- and optical-based signals (based on LED and infrared light) because they can easily produce a signal at these pressures, they don't disturb the environment where we measure and they can be combined in a compact in-house lab setup. Moreover, they allow us to follow the reactions with good time resolution.

In our combined lab setup, we have used a laser imaging technique to study the produced CO_2 molecules, an optical microscopy technique to monitor whether the metal surface becomes oxidized and finally an infrared reflection technique that can show us what molecules are attached to the surface. That way, we could observe that when the CO_2 production above the catalyst is maximized, we can no longer detect any molecules sitting on the surface and at the same time we detect the formation of a very thin surface oxide layer.

In another study, we have combined the infrared reflection technique with an X-ray spectroscopic technique that provides us chemical information about what atomic and molecular species are present on the surface. By adding the infrared reflection spectroscopic technique, the interpretation of the AP-XPS data is facilitated and higher signals at high time resolution can be achieved.

Finally, we have extended our technique development work to also look at reactions at solid-liquid interfaces, so-called electrochemical reactions. Here, instead of heating a sample and initiating a reaction with an increase in temperature, a potential difference is applied at the sample that then drives a current. Such reactions lie at the heart of batteries for example.

All in all, we have shown that by combining different *operando* techniques, complementing, unique information can be gained from one single measurement which opens up the doors for more interesting science.

Populärwissenschaftliche Zusammenfassung auf Deutsch

Die meisten von uns haben schonmal von einem Katalysator in Verbindung mit Verbrennungsmotoren gehört. Bevor die Abgase des Motors durch den Auspuff in die Luft geblasen werden, passieren sie einen Katalysator. Dieser stellt sicher, dass die für uns giftigen Gase, wie Kohlenmonoxid in ein weniger giftiges Gas umgewandelt werden, zum Beispiel zu CO_2: Ein Prozess, der als CO-Oxidation bezeichnet wird. Wir sind jedoch alle darüber im Klaren, dass CO_2 für die Umwelt schädlich und ein Hauptbeiträger zur Klimaveränderung ist. Auch hier können Katalysatoren eine Antwort geben. Bestimmte katalytische Materialien können CO_2 zum Beispiel in Methanol und andere Chemikalien umwandeln und damit die CO_2-Emissionen reduzieren. Die Entdeckung besserer Energie effizienterer katalytischer Reaktionen ist daher für eine grünere Zukunft unerlässlich. Doch bevor wir bessere Katalysatoren herstellen können, muss man verstehen, wie sie auf einer grundlegenden Ebene funktionieren, genauer gesagt, wie Atome und Moleküle mit dem Katalysator interagieren.

Ein Katalysator betsteht aus metallischen Nanopartikeln. Man kann sich diese Nanopartikel wie eine Ansammlung oder einen Cluster von Hunderten bis Millionen von Atomen vorstellen. An ihrer Oberfläche sind sie in einer Vielzahl von Oberflächenstrukturen angeordnet, was diese Nanopartikel sehr komplex macht. Um ein tiefgreifendes Verständnis auf der Ebene einzelner Atome und Moleküle zu erlangen, können wir deren Komplexität verringern und uns eine einzige solche Oberflächenstruktur nach der anderen ansehen. Diese sogenannten Einzelkristalloberflächen sind weniger komplex und ahmen nur den echten industriellen Katalysator nach. Sie werden daher als Modellkatalysatoren bezeichnet.

Während der katalytischen Reaktion interagieren Gase mit diesem Modellkatalysator, der in einem metallischen Feststoffzustand vorliegt. Da hier zwei Phasen der Materie vorliegen (Gas, Feststoff) und interagieren, sprechen wir von einer *heterogenen* katalytischen Reaktion. Um diese Reaktion genauer zu untersuchen, sind Messverfahren und -techniken erforderlich. Beim Messen heterogener katalytischer Reaktionen gibt es zwei Hauptprobleme, die diese Arbeit versucht zu lösen: Erstens möchten wir die Wechselwirkung am Modellkatalysator verstehen, während die Reaktion unter erhöhtem Druck stattfindet, um so nahe wie möglich an industrielle Bedingungen heranzukommen. Die Messung muss daher passieren während der Katalysator ärbeitet"(*operando*). Daher benötigen wir so genannte *operando*-Messtechniken. Im Fall eines Automotors mit Auspuff kann man sich vorstellen, dass der Katalysator sich unter *operando*-Bedingungen befindet, wenn der Motor aufgewärmt ist und schon länger läuft. Die zweite Herausforderung ist die Komplexität von der Wechselwirkung zwischen der Metalloberfläche und Gase zu fangen. Das Ziel ist, so viel Informationen wie möglich aus einer einzigen Messung zu gewinnen. Wir möchten erfassen, wie die große Menge von Gasen bei höherem Druck die Oberfläche beeinflusst und umgekehrt. Da die Reaktion ein dynamischer Prozess ist, der sich mit der Zeit ändert, ist

es wichtig, die Reaktionen mit zeitlich aufgelösten Methoden zu verfolgen.

Diese Arbeit versucht, die beiden Herausforderungen zu beantworten, indem sie Studien vorstellt, bei denen mehrere *operando*-Messmethoden kombiniert wurden. Ein einzigartiger und kompakter Laboraufbau wurde entwickelt, in dem drei optische und laserbasierte Techniken gleichzeitig eingesetzt wurden, um denselben Katalysator zu untersuchen. Die Studien werden nahe bei 1 bar durchgeführt, also bei annähernd Umgebungsdruck. Wir verwenden Laser- und optikbasierte Signale (basierend auf LED- und Infrarotlicht), weil sie leicht ein Signal bis zu mehreren 10 bar erzeugen können, sie die Umgebung, in der wir messen, nicht stören und sie in einem kompakten hausinternen Laboraufbau kombiniert werden können. Darüber hinaus ermöglichen sie es uns, die Reaktionen mit guter zeitlicher Auflösung zu verfolgen.

In unserem kombinierten Laboraufbau haben wir eine Laserbildgebungstechnik verwendet, um die produzierten CO_2-Moleküle zu untersuchen, eine optische Mikroskopietechnik, um zu überwachen, ob die Metalloberfläche oxidiert wird, und schließlich eine Infrarotreflexionstechnik, die uns zeigen kann, welche Moleküle an der Oberfläche haften. Auf diese Weise konnten wir beobachten, dass, wenn die CO_2-Produktion über dem Katalysator maximiert wird, keine Moleküle mehr auf der Oberfläche nachgewiesen werden können und sich eine dünne Oxidschicht bildet.

In einer anderen Studie haben wir die Infrarotreflexionstechnik mit einer Röntgenspektroskopietechnik kombiniert, die uns chemische Informationen darüber liefert, welche atomaren und molekularen Arten auf der Oberfläche vorhanden sind. Durch Hinzufügen der Infrarotreflexionsspektroskopietechnik wird die Interpretation der AP-XPS-Daten erleichtert und ein höheres Signal mit hoher Zeitauflösung erreicht.

Schließlich haben wir unsere Technikentwicklungsarbeit ausgeweitet, um auch Reaktionen an der Grenzfläche zwischen einem Festkörper und einer Flüssigkeit zu untersuchen. Bei sogenannten elektrochemische Reaktionen, wird die metallische Probe nicht erhitzt um eine Reaktion durch einen Temperaturanstieg einzuleiten, sondern eine Spannung wird an die Probe angelegt und dadurch fließt ein Strom. Solche Reaktionen finden beispielsweise in Batterien statt.

Alles in allem haben wir gezeigt, dass durch die Kombination verschiedener *operando*-Techniken ergänzende, einzigartige Informationen aus einer einzigen Messung gewinnen können. Dies öffnet Türen für neue interessante Messungen von unerforschten katalytischen Reaktionen.

Populärvetenskaplig sammanfattning på svenska

De flesta av oss har hört talas om en katalysatoromvandlare i samband med förbränningsmotorer. Innan avgaserna från motorn blåses ut i luften genom avgasröret, passerar de genom en katalysatoromvandlare som ser till att för oss giftiga gaser som kolmonoxid omvandlas till en mindre giftig gas, till exempel CO_2: En process som kallas CO-oxidation. Vi är dock alla medvetna om att CO_2 är giftigt för miljön och en huvudsaklig bidragare till klimatförändringarna. Även här kan katalysatorer ge ett svar. Vissa katalytiska material kan omvandla CO_2 till exempelvis metanol och andra kemikalier och därigenom minska CO_2-utsläppen. Att producera bättre katalysatorer och mer energieffektiva katalytiska reaktioner är därför avgörande för en grönare framtid. Men innan vi kan producera bättre katalysatorer måste vi först förstå hur de fungerar på en grundläggande nivå, mer specifikt, hur atomer och molekyler interagerar med katalysatorn.

Katalysatorer består av metalliska nanopartiklar. Man kan tänka sig att nanopartiklarna är en ansamling eller en klunga av hundratals till miljontals atomer. Nanopartiklar är ordnade i en mängd olika ytstrukturer, vilket gör de komplexa att studera. För att få en djupare förståelse på en atomär nivå kan vi titta på en sådan ytskyrktur i taget. Enskilda kristallytor är mindre komplexa och bara ger en representativ bild av den verkliga industriella katalysatorn. De kallas därför modellkatalysatorer.

Under den katalytiska reaktionen interagerar gaser med modellkatalysatorarna som befinner sig i ett metalliskt fast tillstånd. Eftersom två faser av materie (gas, fast) interagerar i det här fallet, talar vi om en *heterogen* katalytisk reaktion. För att studera denna reaktion krävs mätmetoder. Vid mätning av heterogena katalytiska reaktioner finns det två huvudutmaningar som adresseras i detta arbete: För det första vill vi förstå interaktionen vid modellkatalysatorn medan reaktionen äger rum under förhöjt tryck för att komma så nära industriella förhållanden som möjligt. Detta kräver att man betraktar katalysatorn medan den är ”i arbete”(*operando*). Detta gör vi med så-kallade *operando*- mättekniker. I fallet av en bilmotor kan man tänka sig att katalysatorn arbetar under *operando*-förhållanden när motorn har värmts upp och är igång. För det andra, eftersom interaktionen inkluderar en yta, gaser och interaktionen vid yt-gas gränssnittet, är målet att få så mycket information som möjligt från en enda mätning. Vi vill fånga hur den stora mängden gasmolekyler vid högre tryck påverkar ytan och vice- versa. Reaktionen är en dynamsik process, vilket innebär att den varierar med tiden. Detta medför att det är viktigt att följa reaktionerna med tidsupplösta metoder.

Detta arbete försöker svara på de två utmaningarna genom att presentera studier där flera *operando*-mätningsmetoder har kombinerats. En unik och kompakt labbuppställning har utvecklats där tre optiska och laserbaserade tekniker har kombinerats samtidigt för att studera heterogena katalys reaktioner. Studierna utförs nära 1 bar, alltså nära omgivningstryck.

Vi använder laser- och optikbaserade signaler (baserade på LED- och infrarött ljus) eftersom de lätt kan skapa en signal upp till flera 10 bar, de stör inte miljön där vi mäter och de kan kombineras i en kompakt inomhuslaboratorieuppställning. Dessutom gör de det möjligt för oss att följa reaktionerna med god tidsupplösning.

I vår kombinerade labbuppställning har vi använt en laser avbildningsteknik för att studera de producerade CO_2-molekylerna, en optisk mikroskopiteknik för att övervaka om metallytan oxideras och slutligen en infraröd reflektionsteknik som kan visa oss vilka molekyler som är fästa vid ytan. På så sätt kunde vi observera det följande: När CO_2-produktionen över katalysatorn är maximal kan vi inte längre upptäcka några molekyler som sitter på ytan och en av mätteknikerna är känslig för bildningen av ett mycket tunt oxidyta.

I en annan studie har vi kombinerat den infraröda reflektionstekniken med en röntgenspektroskopisk teknik som ger oss kemisk information om vilka atomer och molekyler som finns på ytan. Genom att lägga till den infraröda tekniken underlättas tolkningen av röntgenspektroskopisk data och en signal med högre tidsupplösning kan uppnås.

Slutligen har vi utökat vårt teknikutvecklingsarbete till att även titta på reaktioner vid ytvätske gränssnitt, så kallade elektrokemiska reaktioner. Istället för att värma ett prov och initiera en reaktion med en temperaturökning, appliceras en potential vid provet som driver en ström. En sådan reaktion ligger till grund för batterier.

Sammantaget har vi visat att genom att kombinera olika *operando* tekniker kan kompletterande, unik information erhållas från en enda mätning som öppnar dörrar för mer intressant vetenskap för att studera outforskade reaktioner.

Chapter 1

Introduction

Chemical processes based on heterogeneous catalytic and electrochemical reactions lie at the heart of many of our everyday life applications: Batteries [1], emission control, such as the three-way catalysts inside our vehicles [2, 3] and the food that we eat thanks to the fertilizers that rely on the Haber-Bosch process [4]. Most importantly, catalytic reactions will play an important role in securing the future energy supply and in reducing CO_2 emissions [5].

The reason behind the abundance of catalysts is that they can lower the energy needed to perform a chemical reaction without being consumed itself [6]. By making heterogeneous catalytic processes more efficient, they can becomes less energy consuming and more climate friendly. However, in order to modify and tailor those processes, a detailed and fundamental understanding on the atomistic level is required. For that purpose, measurements performed by diagnostic techniques are useful [7]. They shed light on the interaction at the surface-gas or surface-liquid boundary since this is where the reaction takes place.

An industrial catalyst is made of deposited nanoparticles on an oxide substrate. To reduce the complexity of these industrial particles, each of the nanoparticles surface facets can be mimicked by single crystal surfaces or deposited nanoparticles, so-called model catalysts [8]. While interactions between model catalysts and gases have been studied over the past 100 years in controlled environments, the challenge for fundamental research has long been to draw conclusions closer to industrially relevant cases. Hence, there has been an urge to bridge two main gaps between fundamental surface science studies and the industrial applications: The material and the pressure gaps [9, 10]. This can be achieved by studying the catalytic reaction while it takes place. As a result, the term *operando* emerged describing the studies of catalytic activity under realistic conditions while the catalyst is "working" [11, 12].

Different *operando* techniques are suitable to study different model catalysts. The exper-

imental techniques used when studying powder catalysts or deposited nanoparticles may differ significantly from the techniques used when studying flat single crystal surfaces. Even though studies on model catalysts are traditionally performed in a well-controlled environment in (ultra-)high vacuum, some of the techniques have been extended to near-ambient pressures in the mbar range with the intention to bridge the pressure gap. Examples are Ambient Pressure- X-Ray Photoelectron Spectroscopy (AP-XPS) [13] and High-Pressure Scanning Tunneling Microscopy (HP-STM) [14]. Moreover, there exists a range of techniques that do not face strong constraints when bridging the pressure gap to ambient pressures up to 1000 mbar. Those are so-called photon-in - photon-out techniques and their advantages for the field of catalysis are plenty:

- They can measure properties right at the catalyst surface without perturbing the reaction zone or damaging the catalyst.
- Photon-in - photon-out techniques have been shown useful when measuring in the pressure range from 10^{-1} mbar towards 1000 mbar. Thus, these techniques are helpful in bridging the pressure gap towards atmospheric pressures.
- Depending on the technique, sub-second to nanosecond (10^{-9} s) temporal resolution and μm spatial resolution can be achieved.

Examples of these photon-in - photon-out techniques commonly used in the field of *operando* catalyst characterization at near-ambient pressures are X-ray Absorption Spectroscopy (XAS) [15], Diffuse Reflectance InfraRed Fourier Transform Spectroscopy (DRIFTS) [16], Polarization Modulation- InfraRed Reflection Absorption Spectroscopy (PM-IRRAS) [17] , Sum Frequency Generation (SFG) [18], High Energy Surface X-ray Diffraction (HESXRD) [19] and Ultraviolet-Visible spectroscopy (UV-vis) [20].

Most of the aforementioned techniques are based on a line of sight measurement where an average along the beam path across the sample is recorded. The development of imaging techniques based on laser imaging, using Planar Laser-Induced Fluorescence (PLIF) [21], or optical microscopy, such as Two Dimensional- Surface Optical Reflectance (2D-SOR) [22, 23], makes it possible to acquire two dimensional information about the gas phase and the surface morphology respectively. First of all, this allows us to study spatial variances in inhomogeneous samples such as curved crystal, deposited nanoparticles and polycrystalline samples on the μm level. Secondly, at near-ambient and ambient pressures, the contribution of the local gas phase becomes more significant due to the increase of gas density above the sample. By imaging the gas phase in two-dimensions right above the catalytically active surface, an understanding of its contributions to the reaction can be gained.

Beyond their imaging possibility, laser- and optical-based *operando* diagnostics exhibit high time resolution. By using pulsed-laser technologies in the nano- to femtosecond range,

very short events can be measured. The use of pulsed lasers also allows for the continuous measurement of well-defined events which can be synchronized to a continuous detection with cameras.

Each previously presented technique often provides one piece of information : Structural or chemical information, either about the surface or the gas phase. Often, the different pieces of information correlate and are complementary. Combining them simultaneously allows us to have a more complete picture of the reaction mechanism. It also avoids the retake of the measurement in a different reactor environment with the risk of the conditions having slightly changed during the retake. Experimental efforts have been made to develop setups where different in-situ and *operando* techniques are combined simultaneously, using synchrotron- and lab-based setups, both for gas phase catalysis [24, 25, 26, 27, 28, 29] , and electrochemical studies [30, 31]. In gas-phase catalysis, both the gas phase, the surface and the gas-surface interface play an important role during the reaction. By measuring all of these properties through a combination of techniques, the range of conclusions that can be drawn from a single measurement expands. This helps in understanding how changes of the surface correlate to the changes in the gas phase and vice versa.

This thesis

The main focus of this thesis is to combine several *operando* techniques to study different model catalysts as well as electrochemical systems. One of the novelties has been to develop a unique experimental lab-based setup that can simultaneously measure the gas phase (fluorescence imaging), the adsorbed species at the surface (infrared surface spectroscopy) and the surface morphology (surface optical reflectance) of model catalysts. The setup relies on optical and laser-based techniques capable of achieving millisecond (ms) and micrometer (μm) temporal and spatial resolution, even at near-ambient pressures of several hundred millibars. The advantage of this in-house setup is to have continuous access which makes it possible to investigate the repeatability and the feasibility of an experiment. Since the focus of the thesis work is technique development, CO oxidation has consistently been employed as a benchmark reaction across various model catalysts, including Pd(100) and polycrystalline Pd.

Another key achievement of this thesis has been to combine optical-, lab-based techniques with synchrotron-based techniques. By simultaneously measuring PM-IRRAS spectra with AP-XPS, we have shown that infrared (IR) spectroscopy is more sensitive when assigning adsorption site under sub-min time resolution and thereby complements AP-XPS that helps us to identify IR-inactive species at the surface such as atomic species and oxide formation.

Outline

The thesis is organized as follow:

- In **Chapter 2**, all experimental techniques and equipment used in the scope of this thesis are described. The end of this chapter focuses on how to combine different *operando* techniques.
- Gas-phase catalysis is the topic of **Chapter 3**. At the beginning, the necessary background and theory knowledge based on surface science and heterogeneous catalysis is provided. Then, some experimental highlights of the thesis work based on gas-phase catalysis are explained.
- Finally, in **Chapter 4**, the use of *in-situ* 2D-SOR in electrochemical environments together with some fundamental concepts is presented.
- **Chapter 5** summarizes the work and elaborates on future studies.
- In **Chapter 6**, the author contributions for the different publications are presented.

Chapter 2

Operando Techniques and Equipment

In this thesis work, laser-, optical- and synchrotron-based measurement diagnostics have been used to study reactions at the gas-surface as well as at the liquid-surface interface. This chapter highlights the different techniques by introducing their light-matter-interaction principle, their respective experimental setup and the data acquisition and analysis process. The main focus of the thesis has been the combined use of different techniques. How this can be realized is explained at the end of the chapter.

1 Optical- and Laser-based techniques

A major part of this work has been to build a combined optical- and laser-based diagnostics setup in the Enoch Thulin laboratory facility at Combustion Physics. Three different diagnostic techniques have been incorporated: Planar-Laser Induced Fluorescence (PLIF), Two Dimensional Surface Optical Reflectance (2D-SOR) and Polarization Modulation-InfraRed Reflection Absorption Spectroscopy (PM-IRRAS). They surround a reactor unit that is introduced at the start of this section. Some of the techniques have been taken out of the in-house lab context and been brought to synchrotron facilities where they were combined with X-ray techniques. This combination is presented in section 4.

1.1 Laboratory Reactor environment

The reactor environment used for combined optical- and laser-based measurements is designed by Leiden Probe Microscopy (LPM). This reactor unit incorporates a bottom part through which water, gas and electrical connections are wired. At the top, these connec-

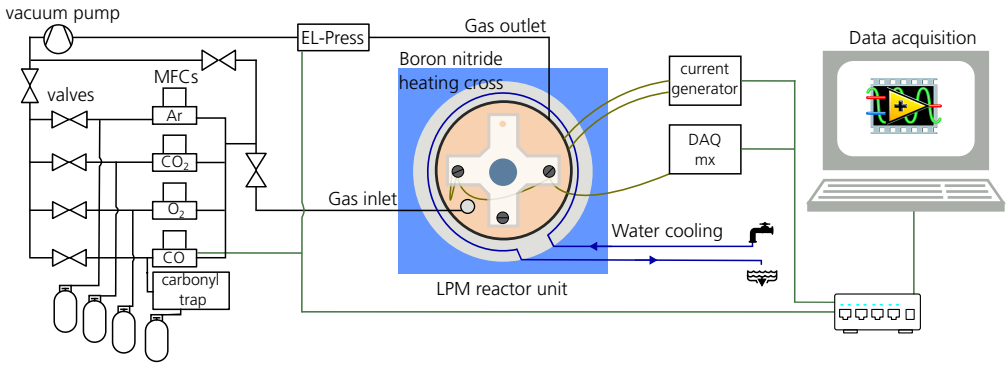

Figure 2.1: Schematic of the reactor and gas-flow system. It can be divided into three parts: The gas flow system (left), the LPM reactor unit (middle) and a software control and acquisition unit (right). On the left side, a schematic of the gas flow system, including Mass Flow Controllers (MFCs), is shown. The four main gases used are Ar, CO_2, O_2 and CO where it is made sure that CO passes by a carbonyl trap first to avoid the accumulation of carbonyls at the catalyst surface. The gas mix then reaches the reactor unit shown in the middle of the picture. Here, the sample is positioned on a Boron nitride resistive holder cross (white) that is heated with the help of an applied voltage. The reactor is water cooled. A thermocouple is connected to one of the screws and read out together with other important devices by a DAQmx (data acquisition) software unit. A control and acquisition unit programmed in Labview collects and controls the measurement parameters.

tions reach to a pressurized chamber with a volume of 18.5 mm^3 that includes the sample holder as shown in the middle of Fig.2.1 [32, 33]. The sample temperature, the total and partial gas flows, the total pressure and different gas species are the parameters that can be controlled with the reactor setup.

In total, there are six mass-flow controllers (MFCs) that can flow the gases Ar, CO, CO_2, O_2, NO and H_2, but mainly the four presented ones in Fig.2.1 are used in this thesis. Each MFC is limited by a maximum flow, ranging from 40 ml/min for the lowest maximum limit to the highest at 200 ml/min. In return, this limits the partial pressure that can be achieved for each gas inside the reactor which depends on their volumetric fraction in the reactor volume (V) and can be approximated by using the ideal gas law $pV = nRT$. Given a constant temperature T, the partial flow (Fl_{part}) in comparison to the total flow (Fl_{tot}) and the total pressure are used to determine the partial pressure of each gas (p_{part}), given by

$$\frac{p_{part}}{P_{tot}} = \frac{Fl_{part}}{Fl_{tot}}.$$

The total pressure P_{tot} is controlled at the reactor output by a digital electronic pressure meter (Bronkhorst El-Press) which adjusts the flow speed to match the correct pressure. By reading off a pressure gauge right at the MFCs output and the set pressure at the El-Press pressure meter, the pressure inside the reactor can be estimated to be the average due to a known gas gradient through the reactor.

Prior to measurements in the high pressure cell, the sample undergoes several cycles of sputtering in Ar+ and annealing procedures in a UHV chamber. Afterwards, the sample

is transferred through air into the reaction chamber by venting the reactor top with Ar. Before any gas-phase catalysis measurement, the sample is heated in reducing conditions, e.g. CO, to desorb adventitious carbon and adsorbed oxygen.

Inside the reactor top, an enclosed sample holder made of a Boron nitride resistive heating cross can be found. The sample is placed on top of the heating cross, as shown in Fig.2.1. The sample temperature has been calibrated to a thermocouple at the heating cross using thermographic phosphors [34, 35]. A detailed temperature calibration and its dependency on the total flow can be found in the SI of paper III. Another schematic of the setup and gas flow can be found in Refs. [36, 23]. A reactor top made of stainless steel encloses the sample holder. It is sealed off by O-rings. Optical access is guaranteed by either a quadratic or an octagon shape reactor top with four or eight side optical windows respectively and one top window.

The most common conditions used throughout this thesis are the following: 150 mbar total pressure, 100 ml/min total flow, 6 mbar partial pressure of CO and O_2. Thanks to the large amount of optical access, the sample can be probed from different directions with a range of *operando* experimental techniques which are presented in the upcoming sections.

1.2 Polarization Modulation - InfraRed Reflection Absorption Spectroscopy (PM-IRRAS)

PM-IRRAS originates from the reflection of mid-infrared (MIR) light from a metal surface. Part of the light is absorbed, by molecules in the gas phase and at the surface, and this absorption results in a vibrational spectrum. Without modulating the polarization, the technique is referred to as IRRAS [37]. In that case, one polarization direction of the IR light (s- or p- linearly polarized) is chosen or the IR light is randomly polarized.

1.2.1 InfraRed Reflection Absorption Spectroscopy

The interaction of a broadband MIR beam with metal surfaces is governed by the selection rule of IR absorption and reflection at metal surfaces [37, 38]. As the name suggests, InfraRed Absorption Reflection Spectroscopy (IRRAS, also known as RAIRS) is based on those selection rules. When IR light hits a metal surface, it can get absorbed by the molecules that sit on top of the surface, so-called adsorbed molecules. They absorb the electromagnetic radiation if they start oscillating which makes their molecular bonds expand and contract. In return, their charge distribution oscillates. In other words, their dipole moment $\overrightarrow{\mu}$ needs to change along the vibrational normal coordinate Q_k ,

$$\frac{\partial \overrightarrow{\mu}}{\partial Q_k} \neq 0.$$

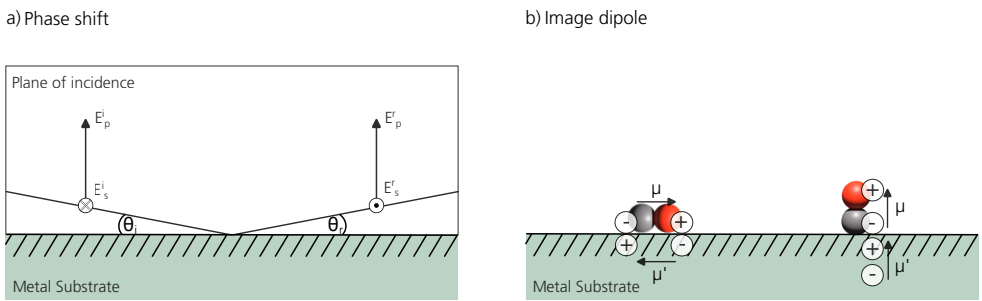

Figure 2.2: Schematic of the metal surface selection rule. (a) The electric field of the incident beam at a grazing incidence angle (θ_i), indicated by an arrow, can either be polarized parallel (E_p^i) or perpendicular (E_s^i) to the plane of incidence. Upon reflection from the surface of a metal substrate (green), the E_s field component experiences a π phase shift while the E_p field experiences only a $\pi/2$ phase shift. (b) The adsorbed diatomic molecule (indicated in grey/red) is polar. If the electropositive charge comes close to the surface, it transfers an electron to the substrate which results in a negative charge right below the surface plane, a so-called image charge. For the direction parallel to the surface, this image dipole cancels out the dynamic real dipole moment while it is enhanced in the direction perpendicular to the surface.

Whether the incoming IR radiation creates a change in dipole moment depends on the orientation of the dipole moment with respect to the polarization of the incident electric field E^i. There are two selection rules that explain why the adsorbed molecules on metal surfaces only experience a change in dipole moment in the direction perpendicular to the surfaces, thus in the p-polarized direction:

- Upon reflection at the metal surface, the IR electric field experiences both a change in amplitude and phase. At grazing incidence, the incoming electric field component E_s^i, that is perpendicular ($\perp$) to the plane of incidence, experiences a phase shift close to 180° upon reflection (see Fig.2.2 a)) leading to a cancellation of that field component. On the contrary, E_p^i experiences a phase shift of 90° leading to a field enhancement [37].

- Upon adsorption, the valence electrons of the substrate surface atoms respond to the presence of the adsorbate. If the adsorbate is electropositive, it will transfer an electron to the substrate which creates a negative charge right below the surface and vice-versa for the electronegative atom as shown in Fig.2.2 b). This creates an image charge and an image dipole moment (μ'). When the IR radiation creates an oscillating dipole (μ), the charge of the image dipole will equally start oscillating. However, only in the case of the dipole being aligned perpendicularly to the surface will this result in an enhancement of the dynamic dipole moment. For the dipole moment parallel to the surface, the oscillation of the image dipole has a cancelling effect [39].

Consequently, if the light remains randomly polarized, only a very small fraction of the

signal will come from the surface. Hence, if the surface is probed, the electromagnetic field properties of the IR photons need to be modified.

1.2.2 Polarization Modulation

Through modulating the polarization of the MIR beam, the contributions in the spectra that merely come from the surface adsorbed species can be extracted [40]. After having passed two plane alignment mirrors, the MIR beam is focused by a first parabolic gold mirror (PGM) (f = 154 mm) onto the sample at a grazing incidence angle. Right after the PGM, a grid polarizer linearly polarizes the beam before it passes through a PhotoElastic Modulator (PEM, Hinds Instruments). Inside the PEM, a piezoelectric actuator is used to compress and stress a birefringent crystal (ZnSe) at a rate of 42 kHz. Thereby, the internal crystal structure changes which in return varies the polarization direction of the IR beam between s- and p-polarized light. An electronic head controller is used to control the PEM with the following settings: $\nu = 2400\,\mathrm{cm}^{-1}$, $\Delta\lambda = 0.5$ and f = 42 kHz. The phase shift δ_m induced by the PEM can be given by

$$\delta_m = \delta_0(\cos(\omega_m t)) = \frac{\lambda_0}{\lambda}\pi\cos(\omega_m t) \tag{2.1}$$

where $\omega_m = 42\,\mathrm{kHz}$ is the modulation frequency of the PEM, λ_0 a reference wavelength and λ any probing wavelength of the MIR beam. Finally, a second PGM collimates the beam before it is focused by a third PGM of shorter focal length onto a liquid-nitrogen cooled IR point detector.

1.2.3 Fourier Transform Interferometer

At the source of PM-IRRAS lies a Fourier Transform Interferometer (FT-IR) (IR cube, Bruker) that incorporates a Michelson Interferometer. It provides a non-coherent broad-band mid-infrared (MIR) signal ranging from 6000-800 cm^{-1} which originates from a heated filament. Thanks to the interferometric nature of the FT-IR, a wider range of species can be detected, also known as Fellgett's advantage [41]. Consequently, the speed of detection is limited by the movable mirror M2 in the interferometer (see Fig.2.3). The MIR output beam has a diameter of roughly 1 cm and is collimated, although slightly diverging. With the help of the interferogram of an overlapping HeNe laser (633 nm, 1.5 mW) inside the FT-IR, the position of M2 and thereby the wavenumbers can be calibrated.

By scanning the movable mirror at velocity v_i (25-200 mm/s), an interference signal is created as a function of the difference in optical path length. This is also referred to as retardation between the beams that travel by the stationary mirror M1 and the movable

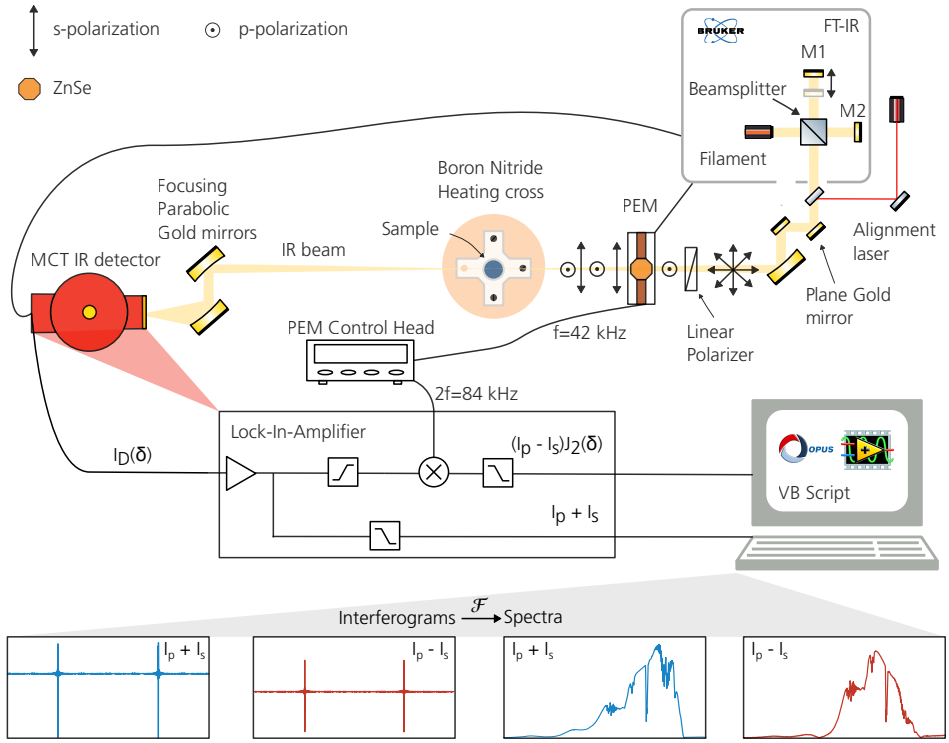

Figure 2.3: Schematic of the PM-IRRAS setup. The setup consists of an FT-IR, with a Michelson interferometer, an alignment laser, a set of gold focusing parabolic mirrors, a linear polarizer, a photoelastic modulator (PEM), an MCT detector with a lock-in amplifier and an acquisition software (OPUS) with a custom-written VBScript acquisition script. The OPUS software acquires both the interferograms (I_p + I_s) and (I_p - I_s). The continously acquired PM-IRRAS spectra are displayed in the custom-written Labview software.

mirror M2. When M2 is continuously scanned, the resulting interferogram is modulated at the following frequency (Fourier frequency) for each wavenumber ν,

$$\omega_i = 2v_i\nu.$$

The result is an interferogram as a function of the retardation δ_M. At an equal optical path length for both mirror arms, at retardation $\delta_M = 0$, a point of zero path difference (ZPD) occurs which results in maximum constructive interference and a clear peak signal in the interferogram. Since the MIR beam remains invisible to our eyes, we installed a diode laser (0.7 mW, 650 nm) that serves as an aligment tool. Using one alignment mirror, a CaF_2 window placed in front of the FT-IR for near- and far-field alignment and several apertures, the red laser beam can be overlapped with the MIR beam for rough alignment.

1.2.4 Detection

A Mercury Cadmium Telluride (MCT) infrared point detector (InfraRed Associates) is used to collect the intensity of the transmitted and refocused MIR beam. It is sensitive to a wavenumber range from 14000-600 cm^{-1}. The detection at the MCT detector is based on two frequency components: A low-frequency component, ω_i, namely the sampling frequency of the interferogram which is determined by the scanning speed of M2, and a high frequency component base on the modulation of the PEM at ω_m.

When the polarization is modulated between s- and p-polarization, the intensity at the detector I_D as a function of the PEM-induced phase shift δ_m can be described mathematically as follows:

$$I_D(\delta_m) = \frac{1}{2}\left(I_s(1+\cos(\delta_m)) + I_p(1-\cos(\delta_m))\right)$$

which can be rewritten into a DC-component (left part) and an AC-component (right part),

$$I_D(\delta_m) = \frac{I_s + I_p}{2} + \frac{I_s - I_p}{2}\cos\delta_m. \tag{2.2}$$

If we insert the expression for δ_m from equation 2.1, the cosine term in equation 2.2 can be expanded as follows into a Fourier series,

$$\cos\ \delta_m = \cos[\delta_0(\cos(\omega_m t))] = J_0(\delta_0) + 2\sum_{n=1}^{\infty}(-1)^n J_{2n}(\delta_0)\cos(2n\omega_m t)$$

where $J_0(\delta_0)$ and $J_{2n}(\delta_0)$ are the zeroth and second order Bessel function respectively. By inserting the expression for $cos\,\delta_m$ back into equation 2.2, the intensity can again be expressed as the sum of an AC and a DC term,

$$I_D(\delta_m) = \frac{I_s + I_p}{2} + \frac{I_s - I_p}{2}J_0(\delta_0) - (I_s - I_p)J_2(\delta_0)\cos(2\omega_m t) \tag{2.3}$$

where the AC and DC intensity components terms are expressed as follows:

$$I_{DC} = \frac{I_s + I_p}{2} + \frac{I_s - I_p}{2}J_0(\delta_0) \approx \frac{I_s + I_p}{2} \tag{2.4}$$

$$I_{AC} = (I_s - I_p)J_2(\delta_0)\cos(2\omega_m t) \tag{2.5}$$

where $\frac{I_s+I_p}{2} >> \frac{I_s-I_p}{2}J_0(\delta_0)$.

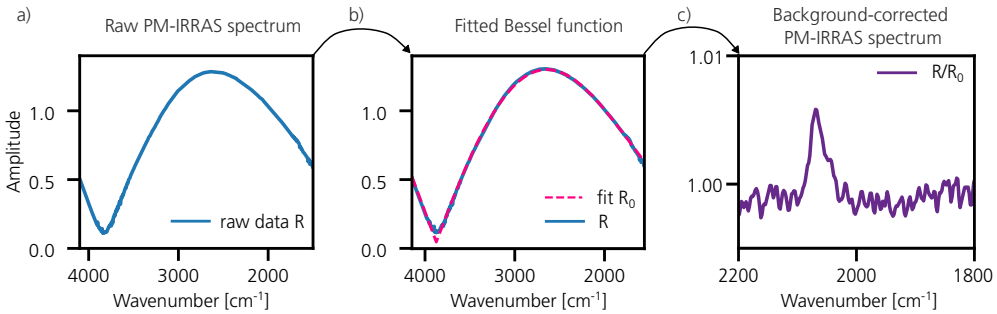

Figure 2.4: Visualization of the algorithm behind PM-IRRAS spectral data analysis. In (a), the raw PM-IRRAS spectrum is shown in blue as it is acquired with the OPUS software cut to the wavenumber range from 4100 to 1500 cm^{-1}. (b) Here, the same raw data as in (a) is shown with the fitted Bessel function (plotted in pink) according to equation 2.7. Finally, in (c), the corrected data is plotted (purple) for a smaller wavelength range from 2200 to 1800 cm^{-1} equal to the division of the raw data R and the fitted Bessel function background R_0. A vibrational peak can be observed in the spectrum at 2060 cm^{-1}.

The DC-signal is filtered out by a low-pass filter while the AC signal is filtered out using a high-pass filter followed by demodulation of the signal using twice the PEM modulation frequency (2f = 84 kHz). This procedure is performed inside the lock-in-amplifier positioned at the back of the MCT detector as indicated in Fig.2.3. Finally, two output channels containing the difference and sum of I_s and I_p are acquired in OPUS. By dividing the two channels, the final PM-IRRAS signal is extracted,

$$I_{PMI} = \frac{I_{diff}}{I_{sum}} \approx \mathrm{C}\frac{(I_s - I_p)J_2(\delta_0)}{I_s + I_p} \tag{2.6}$$

Now, the reason behind the Bessel function shape of the raw PM-IRRAS spectra is understood. In the next section, the removal of this background is explained.

1.2.5 Data Acquisition and Analysis

The PM-IRRAS spectra are plotted as a function of wavenumber

$$\nu = \frac{1}{\lambda}$$

which is the inverse of wavelength (λ), expressed in cm^{-1} and conventionally used in IR spectroscopy. It is proportional to the vibrational energy. The acquisition of PM-IRRAS spectra is controlled via the OPUS software. An experimental file (.xpm) defines the parameters, such as resolution, mirror scanning speed, file name and many more. A custom-written VB Script continuously performs the following steps:

1. It acquires the interferograms of $I_s - I_p$ and $I_s + I_p$ by sychronization of the lock-in amplifier to the PEM modulation frequency.

2. It performs the Fast-Fourier-Transform (FFT) of the two interferograms which then creates two spectra. The FFT includes additional steps such as Apodization, Phase correction algorithm and more [41].

3. It computes the PM-IRRAS spectrum.

To acquire as *operando* as possible without the need to perform any background reference measurements, the background is fitted computationally using the python package *lmfit*. The following function including the second-order Bessel function is used as a background function,

$$\frac{\nu}{\nu_0} J_2\left(\frac{\pi}{\nu_0}\nu\right). \tag{2.7}$$

This is demonstrated in Fig.2.4 and allows us to extract the final surface infrared spectrum as shown in Fig.2.4 c). To ensure the accuracy of the fits, several fits are performed and the one with the lowest residual or chi-square is selected. A Gaussian function can then be fitted to the background corrected peaks using pythons *lmfit* library to extract the peak position and the width.

1.3 Planar Laser-Induced Fluorescence

PLIF is based on two processes: The absorption of laser light by a molecule and the spontaneous emission of a fluorescent signal. In order for the laser energy to be absorbed, the laser wavelength needs to match a transition between two electronic or rotational-vibrational levels of the targeted molecule [42]. Often, the de-excitation occurs at a different wavelength than the excitation and can thus be detected with the help of a filter. While a lot of species are excited with an UV signal using the electronic transition (e.g. CO, NO, CH) [43], certain molecules are more accessible by targeting their ro-vibrational transitions in the mid-IR. CO_2 is an example of such a molecule [44].

1.3.1 Mid-Infrared Laser-Induced Fluorescence

The choice of the molecular transition is crucial for the resulting PLIF intensity. In this thesis, the vibrational transition of CO_2 is denoted by the Herzberg notation of a vibrational state,

$$(v_1 v_2^{l_2} v_3)$$

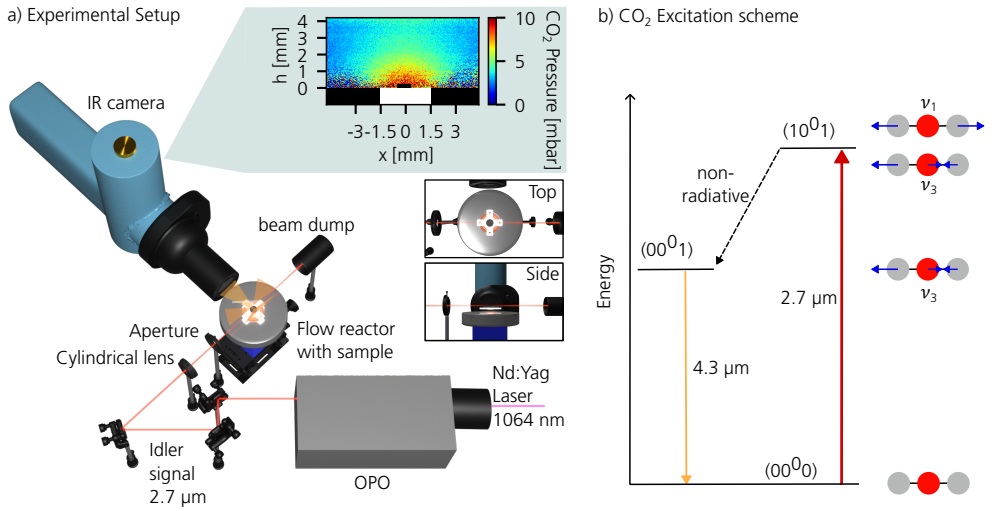

Figure 2.5: Schematic of PLIF principle. (a) A schematic of the experimental setup for PLIF measurements is presented. The fundamental of a Nd:Yag laser at 1064 nm is used to pump a crystal in an OPO. The resulting Idler at 2.7 μm is directed towards a cylindrical lens that focuses the laser only in one direction which results in a planar laser sheet shown as a zoomed-in view from the top and the side. In (b), the excitation scheme based on the Herzberg notation is illustrated.

where v_1 represents the symmetric stretching, v_2 the bending mode (l_2, the degenerate bending mode) and v_3 the assymmetric stretching mode. In this thesis, the transition from the ground state to the first excited symmetric and asymmetric vibration, $(00^00) \rightarrow (10^01)$, at 2.7 μm is chosen to excite the CO_2 molecules. The molecules de-excite at the fundamental wavelength at 4.3 μm as depicted in Fig.2.5 b). However, only the vibration of the asymmetric stretch leads to a change in dipole moment and is therefore IR active. This excitation scheme is chosen for its absorption cross section that is strong enough to obtain a rather good signal, but weak enough to not be severely influenced by absorption through air [32].

1.3.2 Experimental Setup

In order to probe the $(00^00) \rightarrow (10^01)$ transition, an infrared laser signal at 2.7 μm is required which can be achieved by using the fundamental 1064 nm signal of a Nd:Yag laser in combination with an Optical Parametric Oscillator (OPO, GWU versaScanL 1064). We use the Nd:Yag fundamental output at 1064 nm, pulsed at 10 Hz, to pump an OPO crystal with an input energy of 350 mW. The output idler signal at 2.7 μm (30 mW) is then used to excite the ro-vibrational transition to the (10^01) level from where it de-excites in form of fluorescent light at 4.26 μm.

With a cylindrical lens that focuses the round laser beam in only one direction (either

horizontal or vertical), a planar laser sheet of 100 μm thickness can be formed. This allows us to image the CO_2 fluorescence signal distributed over two dimensions. An IR camera (Santa Barbara Focalplane 134) placed perpendicular to the laser sheet images the CO_2 fluorescence by using a lens and a filter centered at 4.26 μm. The IR camera is triggered to the Q-switch of the Nd:Yag laser with a delay of 10 μs to image the peak of the fluorescence decay at an exposure time of 20 μs.

1.3.3 Data analysis

In order to obtain quantitative data from the PLIF images, we need to make sure that we are in the linear regime where the PLIF signal is linearly proportional to the number density of gas molecules in the reactor where quenching and self-absorption can be negligible.

The PLIF signal intensity in the linear regime can be expressed as follows [32][33],

$$I_{PLIF} = \eta_c E g f(T) \sigma_0 N \phi \tag{2.8}$$

where η_c is the collection efficiency, E the laser energy, g the spectral overlap, $f(T)$ the Boltzmann distribution, σ_0 the absorption cross section, N the gas number density and ϕ the quantum yield. This equation shows that the PLIF intensity depends on a lot of factors that can contribute to its signal variations.

The data analysis of each PLIF image is based on the subtraction of the thermal background and a calibration step to a known concentration. In order to calibrate the measurement, a reference measurement needs to be taken at a known product gas concentration at identical experimental conditions.

- **Background subtraction**: In order to extract the weak fluorescence signal and account for variations in temperature and gas composition, the background light which could originate from thermal background needs to be subtracted. For that purpose, the camera is triggered at 20 Hz to capture an image without laser-induced fluorescence in between each laser pulse (at 10 Hz). The background image taken is then subtracted from the image at each laser pulse with a resulting fluorescence signal [45].
- Finally, a **profile measurement** is taken to correct for the variations in temperature ($f(T)$), number density and for calibration purposes. The profile measurement is a replica of the reaction measurement, but only with the measured gas inside the reactor at a known concentration, CO_2 in this case.

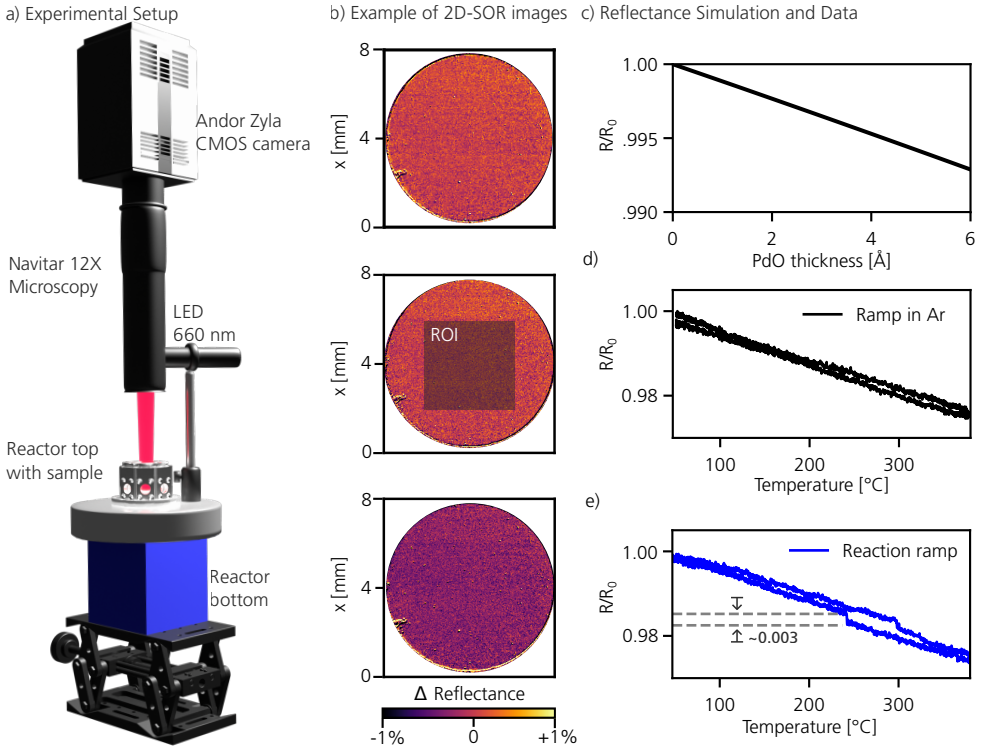

Figure 2.6: Overview of the SOR experimental setup and data analysis. In (a), the experimental setup including the reactor, the LED source, the microscope unit and the CMOS camera is shown. (b) Three reflectance images at different temperatures are shown and the region of interest (ROI) used to create the trends in c) are shown. Note that these images are corrected for signal changes caused by changes in temperature. In c), the simulated reflectance signal, in d) the raw reflectance without reaction conditions and finally in e) the reflectance signal during CO oxidation are shown. All reflectance images (R) are normalized to the reflectance of the first image (R_0).

1.4 Two Dimensional Surface Optical Reflectance

As the name states, Two Dimensional- Surface Optical Reflectance (2D-SOR) images the changes in reflectivity coming from optical light in the visible range off a catalyst surface [22]. In this thesis, it is used in combination with other techniques to provide information about structural changes on the surface such as oxide formation [46, 47], surface reconstructions [48] and roughening.

1.4.1 Surface reflection

2D-SOR is based on changes in reflectance (ΔR) from reflected light off a metal surface. The reflectance of light from surfaces is governed by the Fresnel equations [49]. We consider a three-phase system with different refractive indices: The metal-substrate n_3, a thin film on

top of the metal n_2, such as a thin oxide layer , and the air above n_1. The total reflectance at the interface (n_2) of thickness d is then given by:

$$R_{123} = \left| \frac{r_{12} + r_{23}e^{2i\beta}}{1 + r_{12}r_{23}e^{2i\beta}} \right|^2 \tag{2.9}$$

where $\beta = n_2 \frac{d}{\lambda}$ is the phase change acquired by the transmission through the thin layer n_2 of thickness d. This equation has been simulated for the case of a PdO surface layer on a Pd metal and is shown in Fig.2.6 c).

The reflectivity of metal samples depends on how flat the crystal surface is, on the refractive index of the surface layer n_2, but also on other variables, such as on the amount of free electrons at the surface. The conductivity of a metal increases with the amount of freely moving electrons. From the Hagens-Ruben equation and the Lorentz-Drude model we know that the reflectivity increases with conductivity [50],

$$R \propto 1 - \frac{1}{\sigma}, \tag{2.10}$$

and in return with the amount of free electrons. Since the conductivity is inversely proportional to the temperature [50], we can observe a decrease in reflectivity with increasing temperature as shown in Fig.2.6 d).

1.4.2 Experimental Setup

A red LED lamp at a wavelength of 660 nm is used as the light source for the 2D-SOR measurements in this thesis, as illustrated in Fig.2.6 a). The light is collimated right behind the LED source using a diffuser lens. At the LED output, right above the sample, sits a beamsplitter at 45 degrees that reflects the LED light onto the sample where it bounces back at normal incidence. It is then collected and transmitted by the same beamsplitter, followed by a microscopy unit (Navitar 12X Series) and a CMOS camera (Andor Zyla) as shown in Fig.2.6 a). The resulting images in Fig.2.6 b) show an intensity value per pixel with a pixel resolution of roughly 10 μm. The CMOS camera can both be triggered by an internal or external trigger and can be synchronized to the Q-switch of the Nd:Yag laser, similar to the IR camera used for PLIF. For most measurements in this thesis, the trigger frequency is set to 10 Hz and the exposure time to 10^{-5}-10^{-3} s depending on the samples reflectivity.

1.4.3 Data Analysis

The reflectance trends shown in Fig.2.6 d) and e) are the mean value of a region of interest (ROI) chosen on the 2D-SOR images as shown in Fig.2.6 b). Here, the absolute reflectance

R has been normalized to the value of the first image R_0 at $t = 0$. In order to extract the change in reflectance caused merely by the reaction (ΔR_{reac}), the overall reflectance signal (ΔR_{tot}) needs to be normalized to the reflectance changes merely caused by a temperature change (ΔR_{temp}) ,

$$\Delta R_{reac} = \frac{\Delta R_{tot}}{\Delta R_{temp}},$$

as seen in Fig.2.6 d) and e).

1.4.4 Sensitivity

The 2D-SOR technique is surprisingly sensitive to a range of changes at the surface. One of them is the oxidation of metals. In Fig.2.6 b), 2D-SOR images from before and after the ignition of the CO oxidation reaction over a Pd(100) surface are shown and their corresponding trend from a ROI in Fig.2.6 e). It can be seen that the change in reflectance is approximately 0.3 %. In Fig.2.6 c), we show the calculated reflectance change from the Fresnel equation in 2.9 for a PdO film from 0 to 6 Å, using the complex reactive indices for PdO, Pd and air. It can be seen from Fig.2.6 c) that a 0.3 % change in reflectance from 1.00 to 0.997 corresponds to a thickness of approximately 2-3 Å. This is in good agreement with the formation of a surface oxide, which has been observed in similar reaction conditions on a Pd(100) single crystal [51, 52] and its structure has been determined with LEED [53] as well as with HESXRD under reaction conditions [54]. The formation of thick epitaxial oxides results in losses of reflectance up to 20 % as observed at a high CO/O_2 ratio by [23] and in paper VII.

1.4.5 Resolution

The lateral resolution is described in paper I, II, VI, VII, IX as the distance covered by one pixel and is equal to 10 μm, 15 μm, 5 μm, 100 μm in these papers respectively. One should note that in paper I, II, a 2×2 binning of the images has been used to reduce the size of the acquired data and thereby also the lateral spatial resolution.

There is a trade-off between the field-of-view ($F.o.V.$) and the spatial resolution. In other words, there is a trade-off between how large of a sample we can look at in one image (the "viewed field") and how small a portion of the sample we can resolve. This is often controlled by the magnification (M)

$$F.o.V \propto \frac{1}{M}$$

As an example, in paper VI, the highest resolution of 5 μm has been achieved but by accessing an area of 1.43×1.26 mm^2. Another limiting factor of the 2D-SOR technique is the

small field of view, making it unsuitable for curved crystals for example. The collection of the reflective signal in normal incidence configuration makes it difficult for 2D-SOR to be employed on samples with low initial reflectivity.

2 Synchrotron-based techniques

The measurements presented in paper IV and X were performed at synchrotron facilities using X-ray radiation. Thanks to their high energies (100-10^4 eV) and short wavelengths (0.1-20 Å), X-rays have the advantage of penetrating deep into matter and interacting strongly with atoms and molecules.

In this case, synchrotron facilities are used as X-ray sources, such as MAX IV in Lund, Sweden and DESY in Hamburg, Germany, because of their high photon flux and energy tunability. The high photon flux allows for increased time resolution which is beneficial when following chemical processes *operando*. Inside a synchrotron, electron bunches are accelerated in a so-called storage ring with the help of bending magnets. By being deflected perpendicularly with respect to their velocity, electrons emit high energy radiation in the X-ray regime [55]. Here, the two X-ray techniques used in this thesis based on the processes of diffraction and X-ray-based photoemission are introduced.

2.1 High Energy Surface X-ray Diffraction

High Energy Surface X-ray Diffraction has been combined with 2D-SOR as part of this thesis in paper X for electrochemical measurements. It is based on the diffraction of Hard X-rays ($>$ 10 keV) on a flat crystalline surface [19]. Thanks to its photon-in - photon-out nature, it can be employed at higher pressures [56]. To increase the surface sensitivity, the X-rays impinge onto the sample at a grazing angle below the critical angle, resulting in total external reflection. The interference signal of all diffracted signals is collected by a two-dimensional Perkin-Elmer scintillator detector where the very intense Bragg-peaks from the bulk contribution are covered to study the crystal-truncation rods (CTRS) that originate from the top-most surface layer.

Similar to PM-IRRAS, HESXRD is based on the concept of the Fourier Transform ($\mathcal{F}$). However, instead of looking at $\mathcal{F}$ in the time-frequency domain, HESXRD is based on the concept of spatial frequencies. Every well-defined spatial frequency of the bulk crystal appears as a point in the Fourier domain, also referred to as the far-field image. The periodic structure of a bulk crystal appears as so-called Bragg peaks. If this periodic structure is truncated in one direction by a plane 2D-structure (like a surface), the disturbance of the well-defined spatial frequencies along that direction appears as a rods in the reciprocal

space [57]. Moreover, when the surface structure is disturbed, a change in the diffraction pattern will be observed, such as during surface oxide or island formations. A more detailed description of the technique and data analysis can be found in [19, 57].

2.2 Ambient Pressure- X-ray Photoelectron Spectroscopy

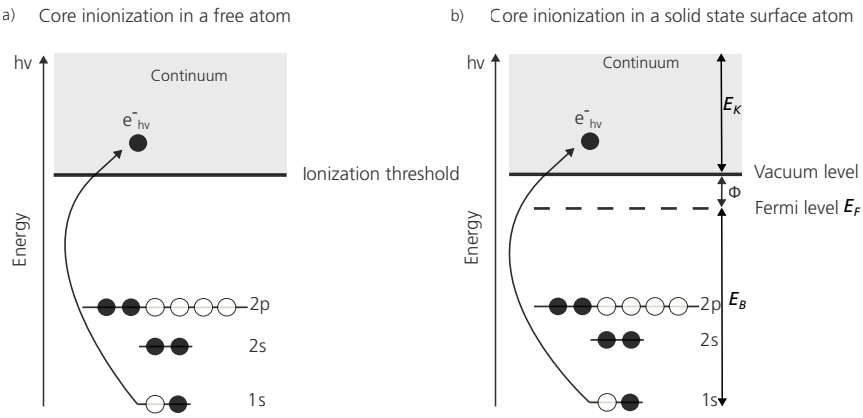

Figure 2.7: Schematic of XPS principle. Here, a simplified energy diagram of the photoionization process used in XPS is presented. As an example, a Carbon atom with the electronic configuration of $1s^2 2s^2 2p^s$ is chosen. In a), the case of a free atom in the gas phase is presented with ionization occurring if the incoming photon has enough energy to overcome the ionization threshold. In a solid, as presented in b), the binding energy E_B of a bound electron is defined with respect to the Fermi level E_F that needs to be calibrated before the kinetic energy (E_K) of the photoelectron can be determined.

Awarded with the Nobel Prize in Physics to Kai Siegbahn in 1981, X-ray Photoelectron Spectroscopy (XPS) is based on the photoelectric effect explained by Albert Einstein. Compared to other techniques presented in this chapter, XPS is a photon-in - electron-out technique where X-ray photons are used to excite photoelectrons from atoms and molecules that can be captured. By analyzing the kinetic energy of these electrons, information about the chemical environment at the sample surface can be obtained. In this thesis, XPS has been used in at near-ambient pressures in the mbar range, a technique called AP-XPS, that was combined with PM-IRRAS to study the chemical composition of catalyst surfaces. The presented AP-XPS measurements were performed at the MAX IV synchrotron, at the gas-phase endstation of the HIPPIE beamline [58].

For AP-XPS, photons in the wavelength range of 0.5-10 nm and energy range from roughly 100-2500 eV, considered as soft X-rays, are commonly used. They can interact with atoms and molecules through absorption. During this process, if photons have enough energy, they can ionize atoms and molecules. In other words, the excess energy from the photon upon absorption transfers into kicking out an electron from one of their atomic or molecular orbitals. The higher the photon energy ($h\nu$), the deeper into the atom or molecule this

electron can sit. This concept is illustrated in Fig.2.7. The specific core-levels from where the electrons are ejected are defined by their species X and electron configuration

$$X\,nl_j$$

where n stands for the electron shell and l for the subshell with a specific angular momentum ($l = 0 \rightarrow s, l = 1 \rightarrow p$). Due to spin-orbit coupling, electrons from one state might give rise to different binding energies due to a coupling of the spin angular momentum $\mathbf{s}$ to the angular momentum $\mathbf{l}$, given by $\mathbf{j} = \mathbf{s} + \mathbf{l}$.

As shown in Fig.2.7 a), for free atoms and molecules in the gas phase, the kinetic energy of electrons (E_k) is referenced to a so-called ionization threshold (ϕ). However, if electrons are ejected from solids, this schematic looks slightly different as shown in Fig.2.7 b). If the electrons are located at core-levels deeper down in atoms in the solid state, an additional potential energy barrier needs to be overcome (Φ). The binding energy of these electrons is then defined with respect to the Fermi level E_F,

$$E_k = h\nu - (E_F + \phi). \tag{2.11}$$

Once the photoelectron reaches beyond the vacuum level, it travels freely and can be collected by an analyzer inside the spectrometer using electrostatic lenses. By referencing the sample and the spectrometer (SP) to the same ground, the kinetic energie of the electron measured with the spectrometer (E^k_{SP}) can then be used to determine the binding energy of the electrons [59],

$$E_B = h\nu - E^{SP}_k - \phi_{SP} \tag{2.12}$$

where ϕ_{SP} is the spectrometer specific work function. By measuring the offset of the electron density of states around zero binding energy, ϕ_{SP} is determined and E_B extracted since the photon energy $h\nu$ is known and E^{SP}_k is measured.

Shifts in binding energy can originate from a change in the chemical environment, so-called chemical shifts, as illustrated in Fig.2.8. They have been shown useful to differentiate contributions of the surface from those of the bulk and help to identify differences in adsorption sites and in oxidation states, as shown by Fig.2.8 a). The amount of bonds also play a role. If NO is bound to three metal atoms (M), its binding energy is lower than if only bound to one metal atom. Another shift that has been observed as part of this thesis is a shift of the samples work function which can be observed when a change in coverage at the surface occurs [60].

At near-ambient pressures in the mbar range, an increased number of electron interactions with gas molecules leads to strong scattering and therefore a loss in signal. A solution for that is to limit the distance that the electron has to travel through the gas by using a nozzle

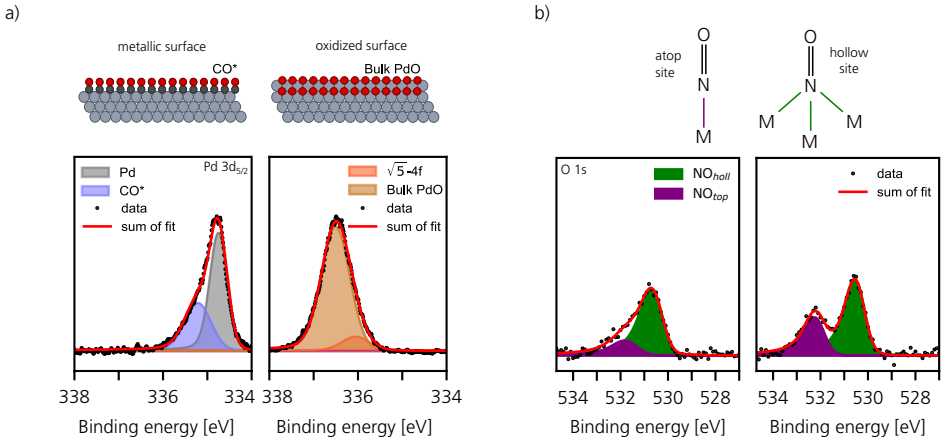

Figure 2.8: **Illustration of chemical shifts**. In a), two spectra of the Pd $3d_{5/2}$ core-level during CO oxidation are shown. While the Pd signal from the metallic surface is at lower binding energy, the oxidized Pd signal can be found at higher binding energies. In b), two O 1s core-levels spectra during CO-NO reaction on Rh(111) are shown with one peak indicating NO adsorption on an atop site (purple) and another one showing adsorption on a hollow site (green).

opening to the analyzer in combination with differential pumping along the electrostatic lens paths before hitting the detector.

Data analysis of the AP-XPS spectra has been performed using the *lmfit* python library. At the start of the data analysis, a Shirley background is removed and finally, the total signal is de-convoluted by fitting its different contributions indicated by the differently coloured peaks in Fig.2.8. More details can be found in paper IV.

3 Mass Spectrometry

To support the gas phase measurements with PLIF and to gain an overview of the gas composition in the reactor, we use a Quadropole Mass Spectrometer (MS, PrismalPlus QMG 220, Pfeiffer Vacuum) to support our optical measurements. The MS setup is placed roughly one meter away from the reactor at the output gas line. Here, a leak valve is leaking part of the output gas mixture from the reactor to the mass spectrometer. An eletric field is then used to direct the ionized species onto an ion detector: Four electrodes are placed parallel to each other in a square formation. By applying a D.C. and A.C. current component between the electrodes, ions of a specific mass are stably directed onto a Faraday detector. By scanning the voltage, ions of different m/z ratios follow this trajectory and can thereby be filtered out. The data is analyzed as a function of the mass-to-charge ratio of the molecules, denoted m/z. Since the signal for each mass comes in units of nA, the current needs to be calibrated to a signal of a species of known concentration. The main molecular masses studied with MS within the scope of this thesis are CO_2 (mass 44), CO (mass 28),

NO (mass 30) and Ar (mass 40).

4 Combination of operando techniques

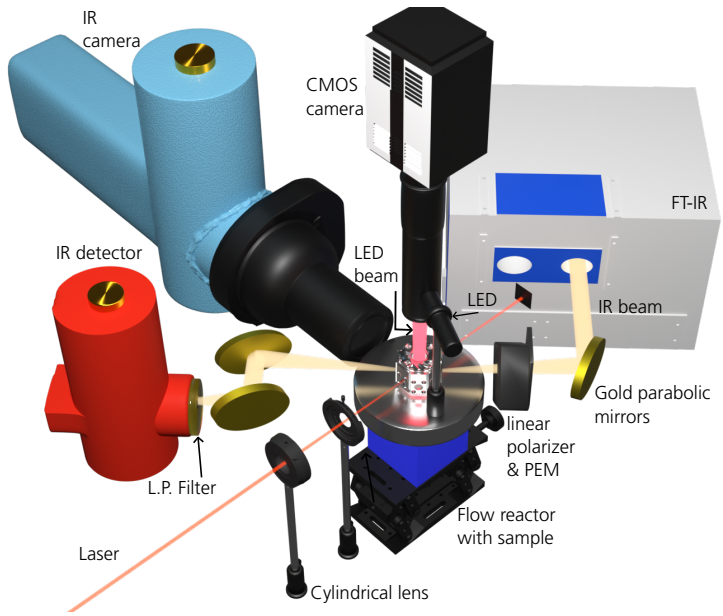

Figure 2.9: Schematic of the combined in-house optical and laser-based setup. The combined optical setup of PM-IRRAS, 2D-SOR and PLIF is positioned around the LPM reactor including the blue reactor foot and the stainless steel reactor top. All three techniques with its light sources and detectors can be identified: The FT-IR and IR detector for PM-IRRAS, the OPO idler laser signal and IR camera for PLIF and the LED source and the CMOS camera for 2D-SOR.

A major part of this thesis work has been dedicated to the development of a combined setup in the catalysis laboratory at combustion physics that allows to measure PM-IRRAS simultaneously with 2D-SOR and PLIF. Most of the presented results in this thesis are a combination of at least two of these three techniques. Another focus of the thesis has been to combine one optical-based technique with one synchrotron-based technique: PM-IRRAS has been combined with AP-XPS in two studies and 2D-SOR with HESXRD in an electrochemical study. The technical challenges and solutions are presented below from a hardware and software perspective.

4.1 Combination of optical- and laser-based techniques

There are some practical requirements that need to be fulfilled in order to combine three optical- and laser-based techniques:

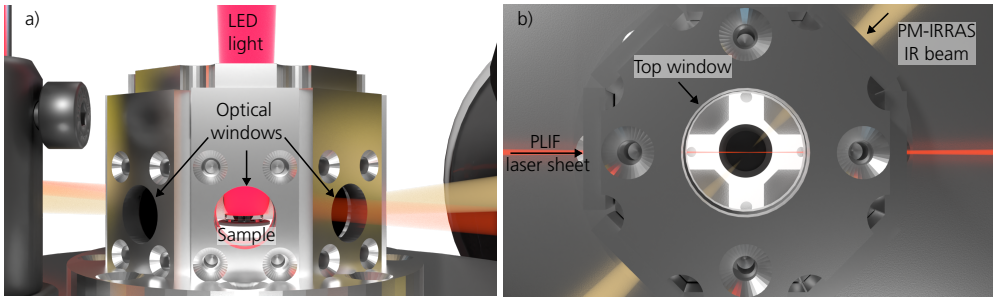

Figure 2.10: **Illustration of custom-designed reactor top**. (a) The sideview of the reactor top shows 3 of the 8 side windows and the incoming 2D-SOR signal. (b) The view from the top shows the different sides of the reactor where 5 windows are used in total for the PLIF and PM-IRRAS signals.

- Optical access for all techniques.
- No interferences. The data of one technique should not be influenced or falsified by the signal of another technique.
- Synchronisation. The data from each technique need to be analyzed using the same timestamp.

The two problems that were faced before the realization of a combined setup were the lack of optical access and the interference of the laser signal with the PM-IRRAS MIR signal. This interference arises because the transmission curve of the IR detector, used for PM-IRRAS measurements, is sensitive to the Nd:Yag fundamental and CO_2 excitation wavelengths as shown in Fig.2.11 a). This leads to noisy PM-IRRAS spectra with insufficient signal-to-noise rations (SNR). Below the solutions to these problems are presented.

While our 2D-SOR setup only uses a single optical window above the sample, PM-IRRAS requires two and PLIF even three optical windows for the in- and outgoing excitation beam and for the camera to image the fluorescence. A custom-designed reactor top that fits the LPM reactor top connections is used for the combined experiments. It incorporates 8 optical side windows (CaF_2 0.5 inch in diameter) compared to 4 side windows (1 inch in diameter). The choice of 8 windows even leaves room for one more incoming and outgoing beams. O-rings are used to seal the reactor volume from the atmosphere.

4.1.1 Hardware filter

In Fig.2.11 a), the transmission curve for the IR detector is shown. We can see that except for the LED λ, all signals involved in the PLIF measurement will be detected by the IR detector and therefore interfere with the PM-IRRAS spectra as shown in Fig.2.11 b). This leads to

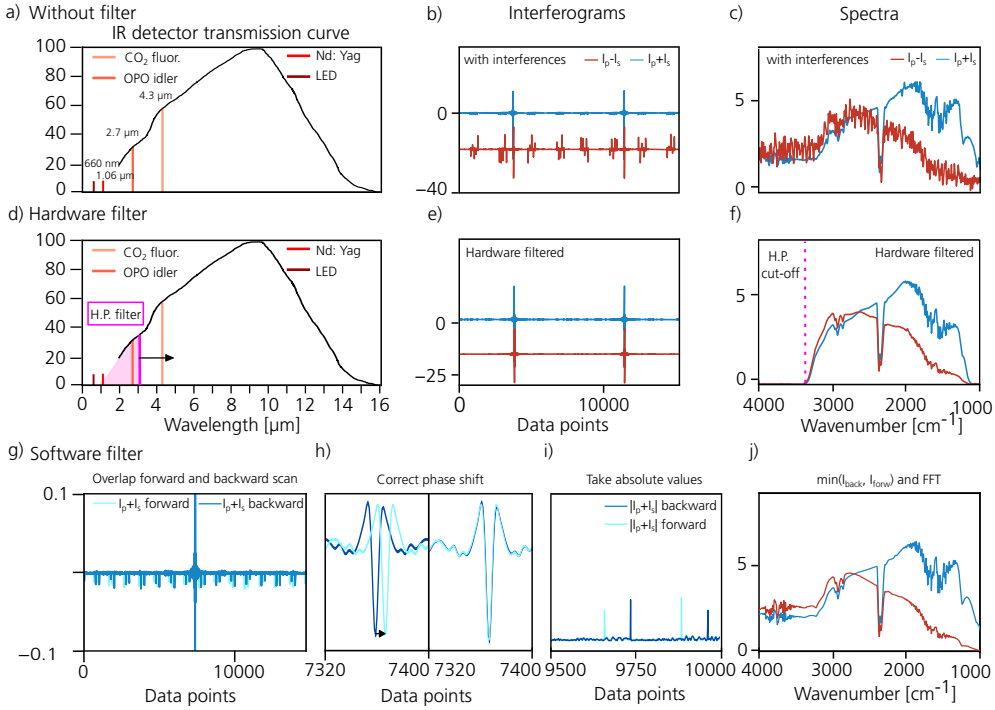

Figure 2.11: Illustrations of the effect of a hardware and software filter.(a) The MCT IR detector response as mentioned in the user manual is plotted as a function of wavelength in μm. The signals that can interfere are plotted as lines in the spectrum: The CO_2 fluorescence at 4.3 μm, the CO_2 excitation at 2.7 μm, the Nd:Yag fundamental wavelength at 1.06 μm and finally the LED wavelength at 0.6 μm. The hardware high-pass (H.P.) filter (LP-3000 nm, Spectrogon) is indicated at 3.05 μm in d). In b) and c), the PM-IRRAS interferograms and spectra for the sum and difference of I_p and I_s are plotted with laser interferences and in e) and f) with the hardware filter being positioned in front of the IR detector. Finally from g) to j), the different steps of the software filter are illustrated, including the overlap of the forward and back scan in g), the correction of the phase shift in h), taking the absolute value in i) and finally choosing the minimum value and taking the Fourier transform to arrive at j), the final spectra.

noisy spectra where the IR vibrational peaks cannot be resolved. By using a high-pass filter (LP-3000nm, Spectrogon) with a cut-off at roughly 3 μm, the Nd:Yag fundamental at 1064 nm and the OPO idler signal to excite the CO_2 molecules are blocked by the filter (see the pink area in Fig.2.11 d). However, the fluorescence signal at 4.3 μm is transmitted. Since the fluorescence signal is neither collimated, nor coherent and much less intense compared to the Nd:Yag fundamental and the OPO idler at 2.7 μm, no more interferences are observed in the interferograms as shown in Fig.2.11 e) and the signal-to-noise ratio in the spectra is acceptable (see Fig.2.11 f)). As expected, a cut-off in the spectra can be observed at 3300 cm^{-1}.

4.1.2 Software filter

Filtering out the unwanted frequencies with a hardware filter can be one solution. However, in order to access a wider range of wavenumbers and avoid a cut-off in the spectra, a software filter can also be employed. This requires a range of post-processing steps that consists of eliminating the peaks in the interferograms originating from laser interferences as shown in Fig.2.11 b).

For that purpose, the double-sided nature of the interferograms has been used. Inside the FT-IR, the movable mirror M2 passes past the ZPD point twince before getting back to its initial position, resulting in an interferogram for the scan forward and backward, $I_{forw.}$ and I_{back} respectively. Except for a phase shift between the two paths, due to a short delay at the turning point of the mirror, both interferograms should be identical and contain the same information. First, the two interferograms, $I_{forw.}$ and I_{back}, are overlayed as in Fig.2.11 g). The second step lies in correcting for the phase shift $\Delta\theta$ between the interferograms such that they properly overlap as visualized in Fig.2.11 h). This is done by performing the Fourier transform of both interferograms to obtain their respective spectra,

$$I_{sum}(\nu) = \mathscr{F}\left(I_{sum}(x)\right) = I_{s,0}\, e^{i\theta_1(\nu)} \tag{2.13}$$

$$I_{diff}(\nu) = \mathscr{F}\left(I_{diff}(x)\right) = I_{d,0}\, e^{i\theta_2(\nu)} \tag{2.14}$$

The phase shift $\Delta\theta$ is defined as the difference in phase between the two spectra (or in time between the two interferograms) as shown in Fig.2.11 h) and is defined such that $\theta_2 = \theta_1 + \Delta\theta$ and

$$\Delta\theta = \theta_2 - \theta_1. \tag{2.15}$$

By taking the product of I_{diff} with the conjugate of I_{sum},

$$I_{diff}(\nu) \cdot I_{sum}(\nu)^* = I_{d,0}\, I_{s,0}\, e^{i\theta_2(\nu)}\, e^{-i\theta_1(\nu)} = I_{prod}\, e^{i\Delta\theta(\nu)}$$

the phase shift in terms of data points can be extracted:

$$\Delta\Theta(x) = \mathscr{F}^{-1}(I_{diff}(\nu) \cdot I_{sum}.(\nu)^*) \tag{2.16}$$

Finally, the absolute value of the superimposed, phase-corrected interferograms is taken and from that value, the minimum of the two is chosen as the final interferogram,

$$I_{filt.} = min(|I_{forw}|, |I_{back}|). \tag{2.17}$$

On the one hand, with the software filter, a broader spectral range is conserved and the cut-off that comes with the hardware filter is avoided. On the other hand, it requires a number of post-processing steps and the different steps of the FFT need to be taken into consideration, such as apodization, phase-correction algorithm and more.

4.2 Combination of Synchrotron and Optical-based techniques

In this thesis work, HESXRD and 2D-SOR and AP-XPS and PM-IRRAS have been combined. Similar to the challenges described above, the optical access of both techniques and the lack of interferences are crucial requirements.

4.2.1 Combining HESXRD and 2D-SOR

When HESXRD and 2D-SOR were combined, an electrochemical cell made of PEEK was designed with a top-optical fused silica window for 2D-SOR access [48][61].

The benefit of combining an X-ray and LED-based technique in the visible is the fact that there are no interferences. In space, one technique probes the sample from above while the other probes it at grazing incidence. While we have seen that 2D-SOR is sensitive to oxide formation and even very thin oxides, it is an indirect method. In other words, 2D-SOR lacks direct structural information, but the reflectance change needs to be calibrated [47]. HESXRD is sensitive to very thin structures at the surface an is therefore suitable for calibration purposes of ordered surface oxide structures.

4.2.2 Combining AP-XPS and PM-IRRAS

To our knowledge, there are two beamlines worldwide that allow for the combination of AP-XPS and PM-IRRAS: The beamline 11.0.2 at the Advanced Light Source in Berkeley [24] and the A-branch endstation at the HIPPIE beamline at the MAX IV synchrotron [58]. In order to make room for the IR beam to be aligned and to impinge onto the sample, the sample stage is retracted 0.5 mm from the analyzer nozzle. This requires readjustment of the X-ray focus. In order to align the PM-IRRAS technique, first, a near infrared source is used for rough alignment. Finally, the alignment is optimized using the CO adsorption peak on a Pt(111) single crystal. Using the python library *pandas*, the MS, PM-IRRAS and AP-XPS spectra could be synchronized according to their timestamp.

The simultaneous measurement of PM-IRRAS and AP-XPS allows us to correlate the assignment of adsorption sites with a high SNR and high resolution (PM-IRRAS) to information about the chemical environment at the surface (AP-XPS). From AP-XPS spectra, different adsorption sites can in principle be distinguished. However, the distance in binding energy is very small which then requires high resolution measurement at lower time resolution. At ambient pressures, the signal-to-noise ratio, thus the sensitivity, is even lower due to an increase of scattered electrons which makes PM-IRRAS the more sensitive choice at sub-min time resolution. While PM-IRRAS measures IR-active molecular adsorbates,

AP-XPS complements this information with information about atomic species and oxide formation at the catalyst surface.

4.3 Techniques Overview

An overview of the different techniques with relevant properties, such as the name of the *operando* technique, the photon wavelength of the probing signal, the spatial resolution, the temporal resolution, the repetition rate and the sensitivity are presented in the table below.

Table 2.1: Characteristics of the *operando* techniques used as part of this thesis. An overview of the excitation wavelength (λ), the spatial (Δx) and temporal (Δt) resolution, the repetition rate f and the sensitivity of the different techniques is provided.

Operando Technique	λ	Δx	Δt	f	Sensitivity
PLIF	2.7 μm	100 μm	10^{-9} s	10 Hz	0.1 mbar
2D-SOR	660 nm	5 μm	10^{-6} s	200 Hz	2-3 Å
PM-IRRAS	7800 - 350 cm^{-1}	1-2 mm	0.5 s	$\frac{1}{4}$ Hz	0.01 ML
AP-XPS	50-5.5 Å	60 μm	30-60 s	$\frac{1}{30}$ Hz	ML
HESXRD	0.15 Å	100 μm	0.5 s	1 Hz	ML

Chapter 3

Gas phase heterogeneous catalysis

Heterogeneous catalytic reactions between a catalyst in the solid state and reactants in the gas phase lie behind the production of most chemical materials that we use in our everyday life. Not the least, for the production of ammonia through the Haber-Bosch process that is used as a fertilizer in agriculture to feed our growing population.

The popularity and employability of catalysts come from the fact that they lower the activation energy barrier needed to overcome for a reaction to happen and to increase its reaction rate [62]. Thereby, they change the reaction kinetics, without themselves being consumed [6]. For CO oxidation, for instance, a crucial energy consuming step is the dissociation of molecular oxygen to atomic oxygen. For a Pt-catalyst, this step can be reduced from consuming 500 kJ/mol without the catalyst to less than 300 kJ/mol with the catalyst [57].

Industrially, catalytic reactions often happen at the surface of deposited nanoparticles on an oxide support. However, these particles have a complex surface structure which makes it difficult to extract detailed information on an atomistic level. Surface science approaches have played an important role in gaining a deeper understanding of the reaction mechanisms on an atomistic level by using flat single crystal surfaces that represent the nanoparticle facets. However, over the years, attempts have been made to study increasingly complex surfaces to bridge the *materials gap* between simple single crystals and nanoparticles, as illustrated in Fig.3.1. Here, the samples that are used in this thesis, except for the industrial monolith catalyst, are illustrated. While most surface science investigations have been based on studies under high or even ultra-high vacuum conditions (10^{-5}-10^{-10} mbar), studies at near-ambient pressures have become important to bridge the *pressure gap* with respect to the industrial applications that often take place at several tens of bars [63]. At such pressures, the amount of gas interacting with the surface increases which can lead to new reaction regimes [64]. Within the scope of this thesis, measurements have been performed

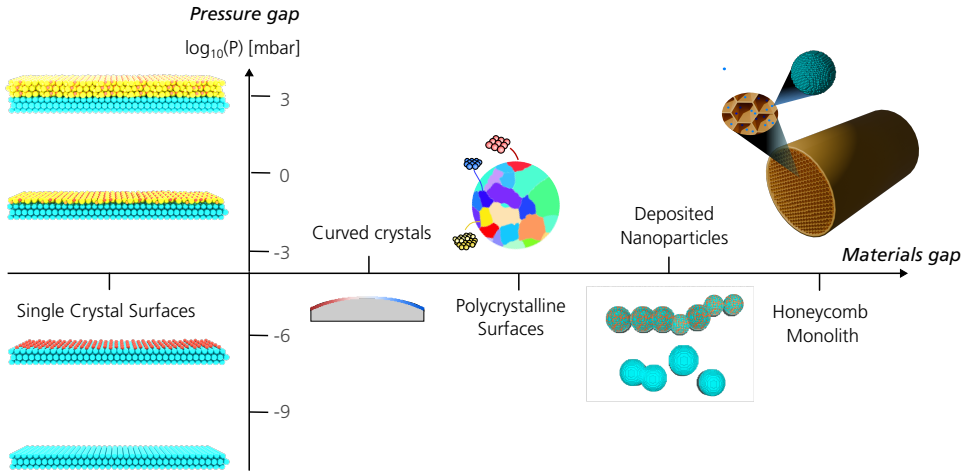

Figure 3.1: Illustration of the materials and pressure gap On the y-axis, increasing orders of magnitude are indicated for the pressure at which experiments are performed in mbar. With increasing pressure, the coverage at the catalyst surface increases which is illustrated by the oxide formation on a single crystal (to the left) from adsorbed oxygen atoms to thicker oxide formation. On the x-axis, the different model catalysts used in this thesis are shown in increasing order of complexity towards an industrial monolith catalyst with a honeycomb structure where nanoparticles are deposited inside the monolith channels.

at near-ambient pressures in the 1-1000 mbar range.

The interaction between the reactant gas and the surface is a crucial step in catalytic reactions. This chapter starts by presenting the different catalytic samples studied in this thesis. Afterwards, the fundamentals of gas-surface interaction mechanisms are explained. Finally, experimental studies on these systems are highlighted.

1 Model Catalyst Systems

Industrial catalysts are often based on so-called monolith reactors [65] with a honeycomb structure that includes channels for the reactant gases to flow through as shown in Fig.3.1. On the walls of these channels, the catalyst material is deposited in form of metal nanoparticles [66]. Nanoparticles are advantageous for catalysis thanks to their high amount of available surface sites [67]. However, their surface composition of different high-index and low-index facets makes them structurally very complex to study. Additionally, they also contain different kind of steps or kinks between those facet planes.

The complexity of these nanoparticle facets can, for example, be simplified by looking at one single surface facet at a time. This aids in identifying how a specific surface structure contributes to the activity of the catalyst under a set of given reaction conditions. Any

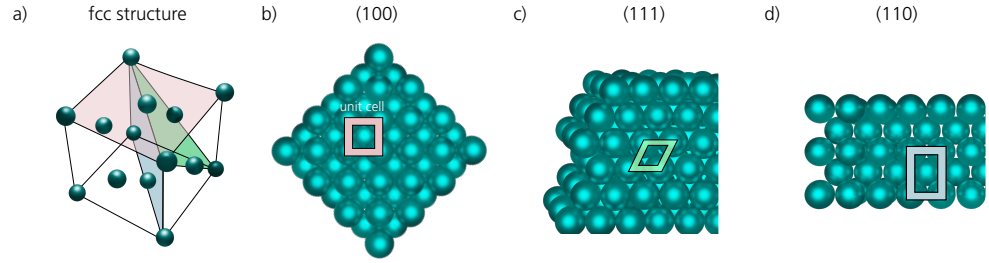

Figure 3.2: **Illustration of a fcc-structured unit cell and single crystal surface structures.** a) A fcc unit cell with three different cut planes, (100) in red, (110) in blue and (111) in green. In b) a (100) surface with a squared, in c) a (111) surface with a hexagonal and in d) a (110) surface with a rectangular unit cell are shown.

structures that are simpler than the real-world industrial catalyst and only mimic their catalytic behaviour are called *model catalysts*. Here, the range of model catalysts used in this thesis are introduced in order of increasing complexity.

1.1 Single crystal surfaces

The simplest structure of a model catalyst are low-index (or high symmetry) single crystal surfaces, which were used to study gas phase catalysis in paper I- IV. Their name is given by the material that they are composed of (e.g. Palladium (Pd), Rhodium (Rh)) and their surface structure. This homogeneous structure across the entire surface is characterized by the so-called Miller indices,

$$(hkl).$$

They define along which plane the unit cell of the bulk crystal is cut [50]. This is illustrated in Fig.3.2 a). The materials used within the scope of this thesis (Pd, Rh) are based on a face-cubic-centered (fcc) unit cell. Three examples of low-index surfaces cut from the fcc unit cell of a Pd crystal are shown in Fig 3.2 b)-d). In a three-dimensional cartesian space, a cut through the plane at $(\infty, \infty, 1)$ (red in Fig.3.2 a)) leads to a (100) plane [50]. A low-index single crystal facet is characterized by Miller indices equal to zero or unity, while high-index facets have at least one index beyond unity [68].

By changing the complexity of the catalyst sample, researchers try to bridge the so-called *materials gap* between conventional crystal surfaces and the industrial samples. In order to access high-index (or low-symmetry) facets and to study several facets at the same time, curved crystals and polycrystalline samples have been proposed.

1.2 Curved crystals

Curved crystals offer an elegant way to study a variety of surface orientations by maintaining a systematic variation of the structural change. Moreover, this variance allows us to monitor the influence of different steps between crystal planes. These properties make curved crystals very suitable model catalysts [69]. Their curvature causes these crystals to exhibit different surface facets in the middle and on each side: The middle surface structure is often low-indexed and the two sides consist of high-index surfaces [70]. These so-called vicinal surfaces differ in the nature of their steps that separate the terrace layers as shown in Fig.3.3.

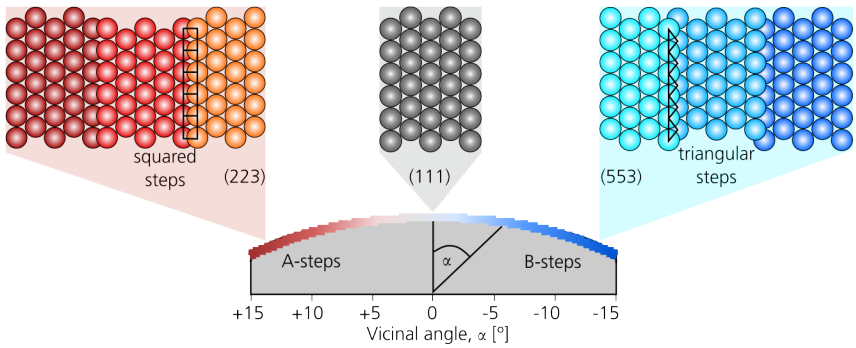

Figure 3.3: Illustration of a curved crystal based on (111) vicinal surfaces. Depending on the vicinal angle α, the surface steps consist of squared A-type steps (marked in red to the left) or triangular B-steps (marked in blue to the right). In the case of c-Rh(111), we observe a (223) and a (553) at +11.4° and -12.3° away from the (111) orientation respectively.

The transition from an upper (111) to a lower (111) terrace is known as *step* and can vary: In the case of a curved Rh(111) sample, it is either determined by A-steps, also square steps, that resemble a {100} microfacet, or by B-steps with a triangular shape, that resemble a {111} microfacet. With higher absolute vicinal angle α, the atom width of the terraces decreases and the steps become more dense.

1.3 Polycrystalline samples

Another model catalyst that allows us to study a variety of single crystal facets simultaneously is a polycrystalline surface. It includes so-called grains of different, but comparable size. Each single grain exhibits a surface facet ranging from low- to high-indexed surface orientations. The orientation of each grain is determined by Electron Back Surface Diffraction (EBSD) that marks every grain orientation with a specific color [71]. Since EBSD is a bulk method, we make the assumption in this case that the surface has the same orientation as the bulk. The color code is explained by an inverse pole figure shown in Fig.3.4 b) [72].

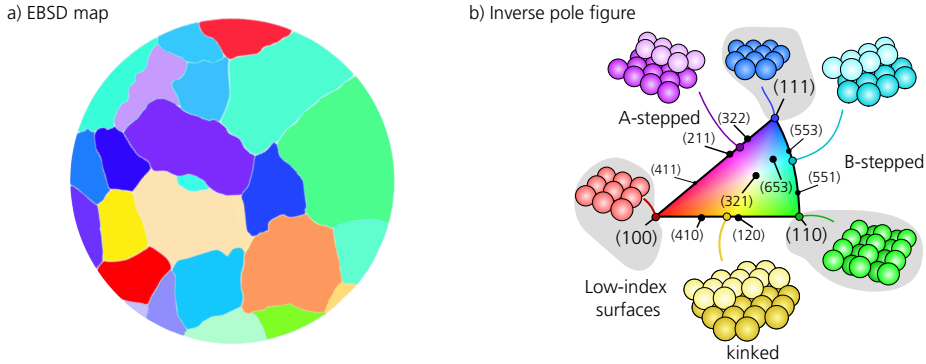

Figure 3.4: Illustration of a polycrystalline sample. In a), a top-view of the sample is shown with the different grains marked with a color that indicates their surface orientation (Courtesy to Hanna Sjö). The inverse pole figure (IPF) in b) relates each color to a surface orientation (adapted from [32]). The surface orientation of the left straight side of the triangle correspond to high-index A-stepped surface. Similarly, on the curved side on the right, the surface orientations correspond to high-index B-stepped surfaces.

The advantage with polycrystalline samples is the possibility to study several surface orientations at the same time. By employing imaging techniques that can spatially resolve the different grains, simultaneous measurements under the same reaction conditions for each grain can be performed. For measurements at ambient pressures, this had led to the development of 2D-SOR as an *operando* technique to study polycrystals thanks to its 2D imaging nature, as described in paper VI and VII.

1.4 Nanoparticles

Metallic nanoparticles form the base of the catalytically active material in industrial catalysts. Depending on their size, these particles can be made of anything from hundred to several millions of atoms. They can come in different shapes, sizes, materials and can be synthesized in different ways. In this thesis, nanoparticles produced with the aerosol-based spark-ablation method have been studied [73]. By controlling the electrode material, the rod diameter and the characteristics of the spark, particles of sub-10 nm size are formed and compacted by agglomeration to 40 nm engineered nanoparticles (ENP) [74] . Nanoparticles can be made of one single material or a mix of materials. In this thesis work, the catalytic activity of Pd, Pd-Cobalt (Co) and Co nanoparticles produced with the spark ablation method have been studied using MS and PLIF. The bimetallic composition of the nanoparticles is achieved by using rods of two different materials. When one rod of the Co is chosen to add magnetic properties to the nanoparticle composition, the particles self-assemble into elongated nanochains by using a directed magnetic field.

2 Gas-surface interactions

Now that we have established how catalysts can look like in increasing structural complexity, it is time to understand how they play a role during the actual catalytic reaction. Heterogeneous catalysis is based on the interaction of molecules and atoms in the gas phase and a metal catalyst in its solid state. In thermal catalysis, a bond between a model catalyst and the reactant gas needs to be formed to create a heterogeneous catalytic reaction. This interaction process is called adsorption and is governed by thermodynamics: It is namely an exothermic process that produces heat [62]. Adsorption can occur in two main forms: Either through physisorption or chemisorption between the surface of the model catalyst and the adsorbant (the gas):

- For **physisorption**, the interaction is determined by the attractive van-der-Waals force [75] without any alternation of the chemical structure.
- Upon **chemisorption**, however, the gas and solid share electrons. In other words the electronic orbitals of the molecule interact with the free valence electrons of the surface which modifies the electronic levels. This interaction can be probed with X-ray and IR spectroscopy which makes it interesting for *operando* measurements.

Surface atoms are highly reactive compared to the crystal bulk atoms because of their lack of neighbouring atoms in the direction of the interface. The surface atoms are undercoordinated with respect to the bulk [62]. This leads to free valence electrons that are highly interactive and that want to create bonds. This way, surfaces aid in breaking or weakening molecular bonds which in return decreases the activation energy necessary for the catalytic reaction to occur. The activation energy is defined as the energy barrier required for the reactant to overcome in order to end up in a certain transient state or product state [6].

2.1 Adsorption sites

Adsorption sites designate the site on the single crystal surface where the gas molecule or atom adsorbs onto. The ratio between surface sites occupied by an adsorbate (N_a) antd the total number of always available adsorbent sites (N_s) is defined as coverage $\theta = \frac{N_a}{N_s}$ [39] which is defined in terms of monolayers (ML). A monolayer corresponds to the number of atoms in the surface layer of the substrate.

In Fig.3.5, several adsorption sites and their respective names are presented. An atop-, bridge- and hollow- adsorbed molecule most often binds onto one, two and three surface atoms respectively. However, depending on the surface structure, hollow sites can vary between a 3-fold (3 bonds) or a 4-fold-hollow (4 bonds) site, although the latter is rarely

seen. Fig.3.5 shows that the observed adsorption sites can vary with surface structure. It has also been shown that the observed adsorption sites can vary with the catalytic metallic material and with the adsorbed molecule [17] .

The vibrational frequency of the chemisorbed adsorbate at a metal surface will vary with adsorption site. When a large number of ligands compete for the charge of the adsorbed molecule, the local charge at that molecule is expected to be small which results in a higher wavenumber [76]. As an example, when the linear molecule CO is chemisorbed on a transition metal, the CO stretching frequency can be observed at increasing wavenumbers for three-fold hollow, two-fold bridge and on-top adsorptions [17]:

$$\nu_{hollow} < \nu_{bridge} < \nu_{atop},$$

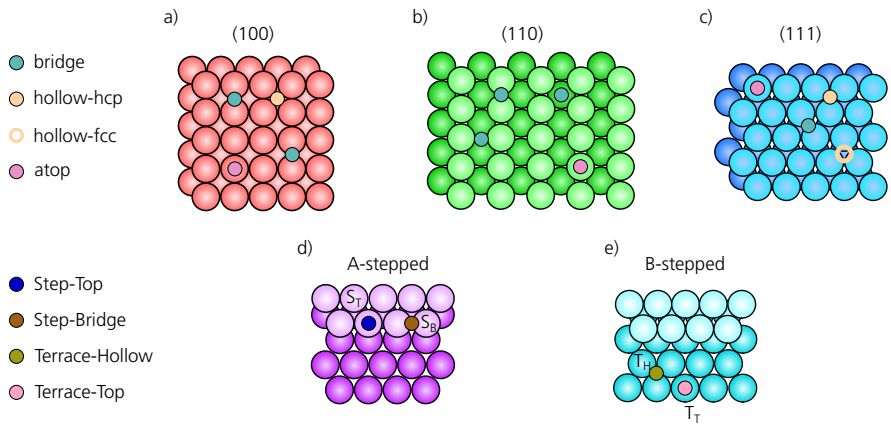

Figure 3.5: Schematic of different surface structures and their respective adsorption sites. In a)-c), three single crystal surfaces: Pd(100) (left), Pd(110) (middle) and Pd(111) (right) are shown. In d) end e), two high-index stepped surfaces are shown, A- and B-stepped respectively with step- (S) and terrace- (T) adsorption sites.

Adsorption sites on curved crystals are distinguished between adsorption on terrace-site (T) and step-sites (S) indicated in Fig.3.5 d) and e). Examples of adsorption sites relevant for the results in this thesis are shown in table 3.1.

Many studies have shown that the occupied adsorption sites can vary with pressure and temperature [64, 82]. With an intent to bridge the *pressure gap*, pressures are increased which results in greater coverages. With increasing coverages, the intermolecular dipole-dipole interactions increase which leads to a shift to higher wavenumbers or frequencies and increased interaction [17, 88].

Under certain conditions during CO oxidation, oxides are observed to form on the catalyst surface. In the following section, the concept of oxidation and surface oxides is discussed.

Table 3.1: **Reference wavenumbers from PM-IRRAS and binding energies from (AP-)XPS measurements for CO and NO adsorption**. The surfacse chosen are Pd(100), Pd(111), Pd(210) and Rh(111). It should be noted that the pressures and temperature for these values vary for each reference. The wavenumbers and binding energies are susceptible to change with coverage and temperature. Here, reference peaks are chosen at similar conditions to the ones in this thesis. The binding energies are taken from different core-levels that are indicated in brackets.

Sample	Molecule	Adsorption Site	Wavenumber	Binding Energy	References
Pd(100)	CO	bridge	1983 cm^{-1}	286 eV (C 1s)	[77, 17, 78, 79]
Pd(100)	NO	bridge	1672-1630 cm^{-1}	335.7 eV (Pd 3d)	[77, 79]
Pd(100)	NO	atop	-	336 eV (Pd 3d)	[79]
Pd(111)	CO	bridge	$1950 - 1960$ cm^{-1}	285.76 eV (C 1s)	[80, 17, 81]
Pd(111)	CO	3-fold hollow	1880-1895 cm^{-1}	285.59 eV (C 1s)	[80, 81]
Pd(111)	NO	atop	1735 cm^{-1}	-	[82]
Pd(111)	NO	3-fold hollow	1590 cm^{-1}	-	[82]
Pd(210)	CO	bridge	1878-1996 cm^{-1}	-	[17]
Rh(111)	CO	atop	2050-2100 cm^{-1}	286.0 eV (C 1s)	[82, 83, 84]
Rh(111)	CO	3-fold-hollow	$1850 - 1900$ cm^{-1}	285.4 eV (C 1s)	[82, 84]
Rh(111)	NO	atop	1813-1850 cm^{-1}	400.3 eV (N 1s)	[85, 86, 87]
Rh(111)	NO	3-fold-hollow	1650 cm^{-1}	400.3 eV (N 1s)	[85, 86, 87]

2.2 Oxidation and Reduction

Several results presented in this thesis are based on the concept of oxidation and reduction. If an atom or a molecule is oxidized, it gains an atom of oxygen or looses an atom of hydrogen. In other words, it looses electrons. On the other side, reduction is the gain of electrons which can occur either through a loss in oxygen or a gain in hydrogen.

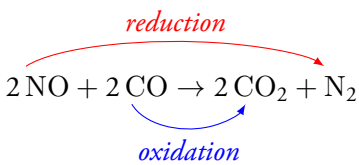

Above, an example of a so-called redox reaction is presented. This includes a reduction step where NO looses an oxygen bond and reacts to N_2 and an oxidation step where CO oxidizes to CO_2.

2.3 Oxide formation

Metal oxides play an important role in multiple catalytic reactions [89, 90]. In the case of metallic surfaces, oxides can form at high temperature through exposure with atomic oxygen or O_2-rich reaction conditions [91]. Depending on the local gas composition above the catalyst surface and the temperature, the oxygen coverage of the surface is different. The adsorbed oxygen forms different surface structures as shown in Fig.3.6 as a function of

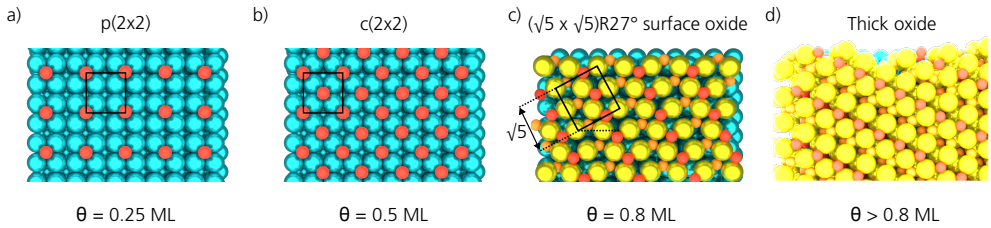

Figure 3.6: Schematic of different oxide structures forming with increasing oxygen coverages on Pd(100). The Pd atoms are shown in blue while the Pd atoms in the oxide layer are coloured in yellow and the oxygen atoms in red or orange. In a), a p(2x2), in b) a c(2x2), in c) a $(\sqrt{5}x\sqrt{5}))R27^{\circ}$ and in d) a thick oxide are illustrated.

coverage and temperature. Here, the oxide formation on Pd(100) is taken as an example since it is relevant for the results in this thesis.

On Pd(100), at lower coverages around 0.25 and 0.5 ML, a p(2x2) and c(2x2) structure forms respectively, depicted in Fig.3.6 a) and b). At a significant O-coverage of 0.8 ML, a well-defined ultra-thin surface oxide is formed that consists of a single PdO(101) layer containing rows of both 2-fold and 4-fold oxygen-coordinated Pd atoms [92, 53]. At very high oxygen pressures and high temperature conditions, even thicker oxides can grow on the Pd(100) surface. Several studies show that the thicker oxide comes in the form of a multilayer PdO(101) surface which can grow up to 5 ML [93, 94, 95]. However, a recent study has shown that at slightly higher temperatures, a PdO(100) can coincide with the PdO(101) to form an epitaxial and rough oxide of thicknesses up to 15 ML [91].

The oxide structure and O-coverage vary with surface structure and material. For example, compared to Pd(100), the Rh(111) surface forms a surface oxide with 1.6 ML O-coverage [96] and a trilayer O-Rh-O structure. While oxide structures may form at the surfaces, even without an oxide being present, the surface structure itself can vary from the original bulk structure because that newly formed structure is energetically favourable.

2.4 Surface reconstruction

When the surface of a bulk crystal does not have the "expected" periodicity, one refers to the surface being reconstructed. For example, an Ir(100) bulk crystal has a square unit cell structure, however at the surface the inter-atomic distance becomes a bit smaller which makes it energetically more favourable for the crystal surface to be have a hexagonal structure [97].

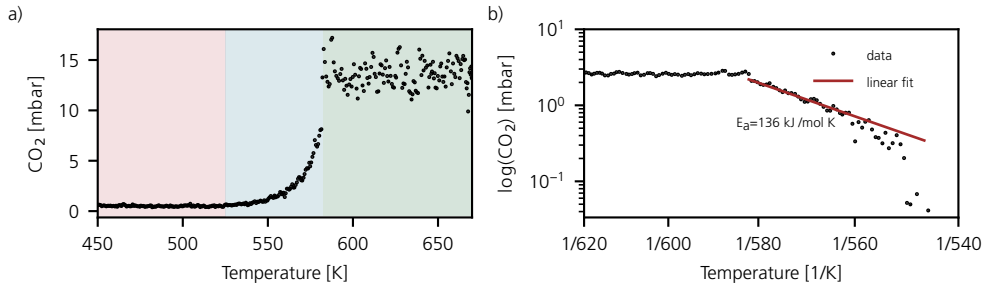

Figure 3.7: **PLIF trend and Arrhenius plot during all three reaction regimes of CO oxidation on Pd(100).**) a) PLIF trend of CO_2 during CO oxidation at 910 mbar and a CO:O_2 ratio of 1:2. The reaction goes through all three reaction regimes: CO poisoning (red), kinetic-limited regime (blue) and the mass-transfer-limited regime (MTL) (green). b) The natural logarithm of the data in a) is plotted in log-scale and as a function of inverse temperature in K. In brown, a linear fit along the kinetic regime is performed and the activation energy is extracted from the slope to be 136 kJ mol^{-1} K^{-1}.

3 Heterogeneous catalysis

A heterogeneous catalytic reaction between a solid and a gas from its product to its reactant state is described by a reaction rate r that depends on a rate coefficient k. In this thesis, a ramp in temperature has mainly been used to control and study different reaction regimes as shown in Fig.3.7 a). When the reactivity changes with temperature, collision theory is at the basis of the reaction kinetics [62]: If we increase the temperature, we increase the kinetic energy of the molecules. In return, they are more likely to collide. If they have enough energy upon collision, there is a chance for them to react. When this is the case, the activity can be described by the Arrhenius equation,

$$k(T) = A \exp(-E_a/RT), \tag{3.1}$$

where E_a is the activation energy of the reaction, R the gas constant, T the temperature in Kelvin and A a pre-exponential factor that can include other dependencies of the rate [62]. By plotting the natural logarithm of the CO_2 formation using the PLIF trend ($\ln(CO_2)$), a linear fit to the kinetic regime can be compared to equation 3.1 by using

$$\ln(k(T)) = \ln(A) - \frac{E_a}{R}\frac{1}{T} \tag{3.2}$$

which is often used to extract the activation energy. Here in Fig.3.7, an example of CO oxidation on Pd(100) with a CO:O_2 ratio of 1:2 at 13 mbar CO partial pressure is presented. The logarithmic trend can be fitted with a linear function. By extracting the value of the slope, the activation energy is determined to be 136 kJ mol^{-1} K^{-1} which comes close to the activation energy previously determined under similar measurement conditions [98].

But what is the measure of catalytic activity in order to differentiate how well a material performs catalytically? The activity of a catalyst is often defined in terms of the turnover

frequency (TOF): The amount of product molecules produced per second per active site. In a flow reactor where CO oxidation is the studied reaction, with CO_2 as the product gas (p_{CO_2}), the TOF is given by [99]:

$$TOF = \frac{1}{RT}\frac{p_{CO_2}}{p_{tot}}\frac{N_a}{N_s}F, \tag{3.3}$$

where R is the gas constant, T the temperature, p the partial and p_{tot} the total pressure and F the total flow.

Not all materials are suitable for adsorption and surface reactions to effectively occur. It has been shown that transition metals or so-called d-band metals are especially suitable for molecules to not adsorb too strongly, but strongly enough to interact (Sabatiers principle). Due to their partially filled d-band, there is a high density of states of the d-band just below the Fermi level. As an example, the d-bands of Pd, Pt and Rh are to 90%, 90% and 80% filled respectively [97]. Part of the very localized and narrow d-band is even situated above the Fermi level. This creates a strong interaction between the adsorbate and the surface.

These properties have been shown useful for CO oxidation as explained in more detail by the Hammer-Norskov model [100]. The narrow d-band of the metal highly interacts with the 5σ and $2\pi^*$ molecular orbital of CO where the valence electrons are located (CO electronic configuration is given by $KK(3\sigma)^2(4\sigma)^2(1\pi)^4(5\sigma)^2$ [101, 102]. Upon this strong interaction, both molecular orbitals split up into a bonding and antibonding orbital. By filling the antibonding orbitals two things occurs: The molecular-surface interaction is strengthened, but the intrinsic bond of the CO molecules is weakened, making it "lagom" (*just right*) reactive.

4 CO oxidation

CO oxidation is historically studied due to its importance in the cleaning of exhaust from a combustion engine three-way car catalysts [2]. Even with the production of combustion engine based cars on the decline, the motivation remains to study the reaction for better emission control in different industrial combustion contexts. Besides that, CO oxidation on single-crystal transition metals, such as Rh, Pt and Pd, is well studied for different systems and conditions [103]. Given the dipole moment of the CO molecule, it is an excellent reaction to benchmark surface adsorption sites and coverages. Due to its well-studied nature and literature access, it is very suitable as a proof-of-principle reaction [103] for technique development where reliable references are needed. It has therefore been used in paper I- VIII.

Stochiometrically, the reaction is written as follows:

$$2\,CO + O_2 \rightarrow 2\,CO_2.$$

At surfaces, the reaction mechanism for CO oxidation can be classified into three main ones, briefly described below:

- In the **Langmuir-Hinshelwood-mechanism (LH)**, the two molecules CO and O_2 in the gas phase chemisorb on free sites where molecular oxygen dissociates upon adsorption (CO*, O*). When they diffuse and collide, they can form an adsorbed product CO_2* that finally desorbs into the gas phase (CO_2).
- During the **Mars-van-Krevelen (MvK)** mechanism, the reaction occurs on an oxide surface structure where only one product gas is adsorbed (O_2*). A second species collides in the gas phase (CO) to form a chemisorbed product ($CO_{2,g}$*) with that structure, that then finally desorbs (CO_2). This leaves an oxygen vacancy that is then replenished by the O_2 gas.
- The **Eley-Rideal mechanism (ER)** suggests that only one species strongly adsorbs (in this case O_2) without necessarily forming an oxide structure, whereas CO stays in the gas phase or very weakly bound. When the species react, their residence time at the surface is close to zero.

The reaction outcome depends on several factors, such as the temperature (T), the partial pressure (p), the CO:O_2 ratio and the gas flow. Those are parameters that can be controlled in the in-house laboratory setup in section 1.1. At the beginning of the reaction, the sample resides at room temperature and the reaction gases are dosed, diluted with Ar to adjust their partial pressure. In most presented measurements, the temperature is ramped in isobaric conditions with the help of a resistive Boron nitride heater cross that heats the sample from underneath.

At pressures in the mbar range, three main reaction regimes are observed as presented in Fig.3.7 a):

1. CO poisoning: An inactive regime where no catalytic activity is observed and the sample is fully covered in CO.
2. Kinetic regime: A regime where CO starts to react with oxygen atoms that have formed from dissociatively adsorbed O_2 to form CO_2. More CO_2 is produced with increasing temperature due to more CO desorbing from the surface, leaving free surface sites for the O_2.
3. Mass-Transfer-Limited (MTL) regime: A regime where the CO_2 production remains invariant with increasing temperature. Here, the activity of the catalyst is limited by the diffusion of reactant molecules to the catalyst surface which is why this regime is also called the diffusion-limited regime.

The transition from the kinetic to the mass-transfer-limited regime happens very suddenly. At this point, we can observe a strong increase in catalytic activity at a specific temperature that is referred to as light-off or ignition temperature.

As mentioned earlier, transition metals are suitable for heterogeneous catalytic reactions, especially CO oxidation. Based on the model catalysts presented in section 1, various studies of CO oxidation are presented below.

5 Combined measurements

5.1 CO oxidation on Pd(100)

CO oxidation on Pd(100) is chosen as a benchmark reaction for combined technique development as part of this thesis in paper I-VIII. The main reason for that lies behind the well-studied nature of the reaction and its documentation in literature both at (U)HV conditions [104] and at near-ambient pressures [105, 106, 107, 108, 98].

5.1.1 Optical- and Laser-based Combined study

CO oxidation has been studied at different pressures with the combined optical- and laser-based setup presented in section 4.1 in chapter 2. However, before PLIF and PM-IRRAS can be measured simultaneously, different filter options, as presented in section 4.1, need to be tested. In Fig.3.8, the vibrational spectra of CO adsorbed on bridge sites on Pd(100) are shown without any laser interference and with two filter options during laser interference. The results based on the software and the hardware filter (see section 4.1 in chapter 2) are compared to the case where no laser interference occurs.

By comparing the CO adsorption peaks, we can observe that the signal is clearly visible in all three options in Fig.3.8 until the CO coverage is too low to be detected. Given a worse signal-to-noise ratio for the software filter Fig.3.8 b), low coverages cannot be resolved. Additionally, the adsorption peak seems broader than in the other cases. This is most likely due to the fact that we have not yet incorporated a phase-correction algorithm into the software filter, such as the Mertz algorithm, which is common for the processing of the Fast-Fourier-Transform (FFT) of FT-IR data. While the hardware filter gives a better signal-to-noise ratio and a better resolved peak ($\sigma_{hard} < \sigma_{soft}$), it limits the wavenumber range to $3235 - 1200$ cm^{-1} which might exclude IR signals beyond this range. Moreover, one should be aware that the hardware filter reduces the IR counts and might thereby decrease the sensitivity for minor species.

For the combined measurements presented in paper III, the hardware filter has been chosen

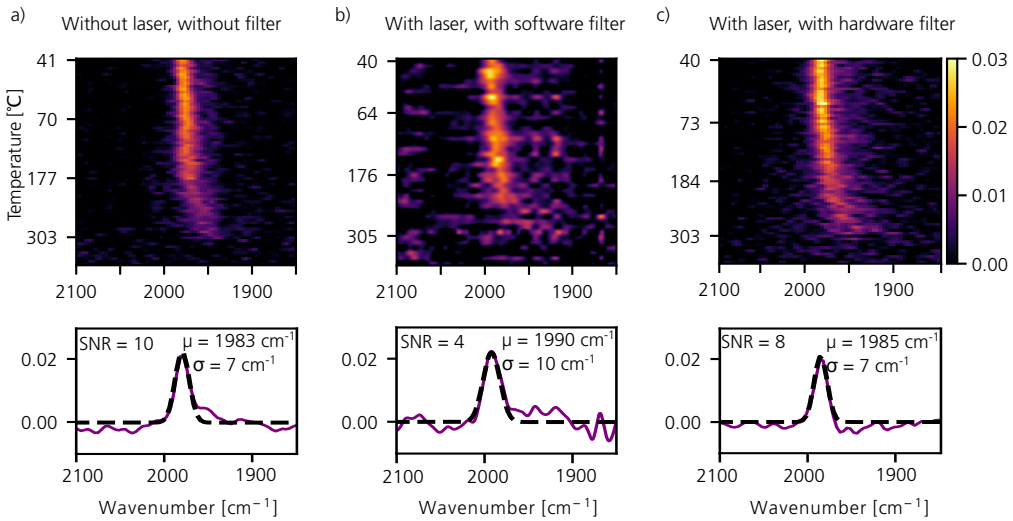

Figure 3.8: PM-IRRAS spectra of CO adsorbed on Pd(100) during CO oxidation at 150 mbar for different filter options. a) Without any laser interference, b) with laser interferences and the employed software filter option and c) with laser interferences and an employed hardware filter option.

to facilitate the online data analysis in the local acquisition and visualization software (LABVIEW). The results for one temperature ramp presented in Fig.3.9 are measured at 150 mbar (6 mbar CO partial pressure) and 910 mbar (13 mbar CO partial pressure). As presented in Fig.3.9 d), the temperature is continuously ramped at a rate of 0.5°C/s. By integrating a spectral and spatial region of interest for each optical technique, shown in grey boxes in Fig.3.9 a)- c), we can create the different trends. This allows us to correlate the events at and on the surface to the changes in the gas phase as a function of temperature. These results have been published in paper III. Here, some data analysis possibilities and limitations of the study are discussed.

The three reaction regimes described in section 4 have been identified and labelled in Fig.3.9. Between the kinetic regime II and the MTL regime III, a sudden jump in CO_2 pressure can be observed indicating that the Pd(100) is more active in regime III than in regime II. This ignition of the catalyst varies with partial pressure of CO and occurs at 298°C and 311°C at 150 and 910 mbar respectively. The rise from regime II to III takes spans 1.5 °C, thus 3 s. The repetition rate (or the frame rate) for PLIF and 2D-SOR is set to 10 Hz in this particular measurement. However, in paper II, the repetition rate was increased to 200 Hz and can resolve that the "heat-wave" led by gas diffusion and the surface oxide evolving from the center towards the edges of the crystal. This could be increased quite significantly and is limited by the repetition rate of the laser (f_{rep}). An increase in f_{rep} can be achieved by using another laser system, but the pulse energy might be affected ($E_P = \frac{P_{avg}}{f_{rep}}$) .

At the same time, the PM-IRRAS spectra are limited by the speed of the FT-IR mirror

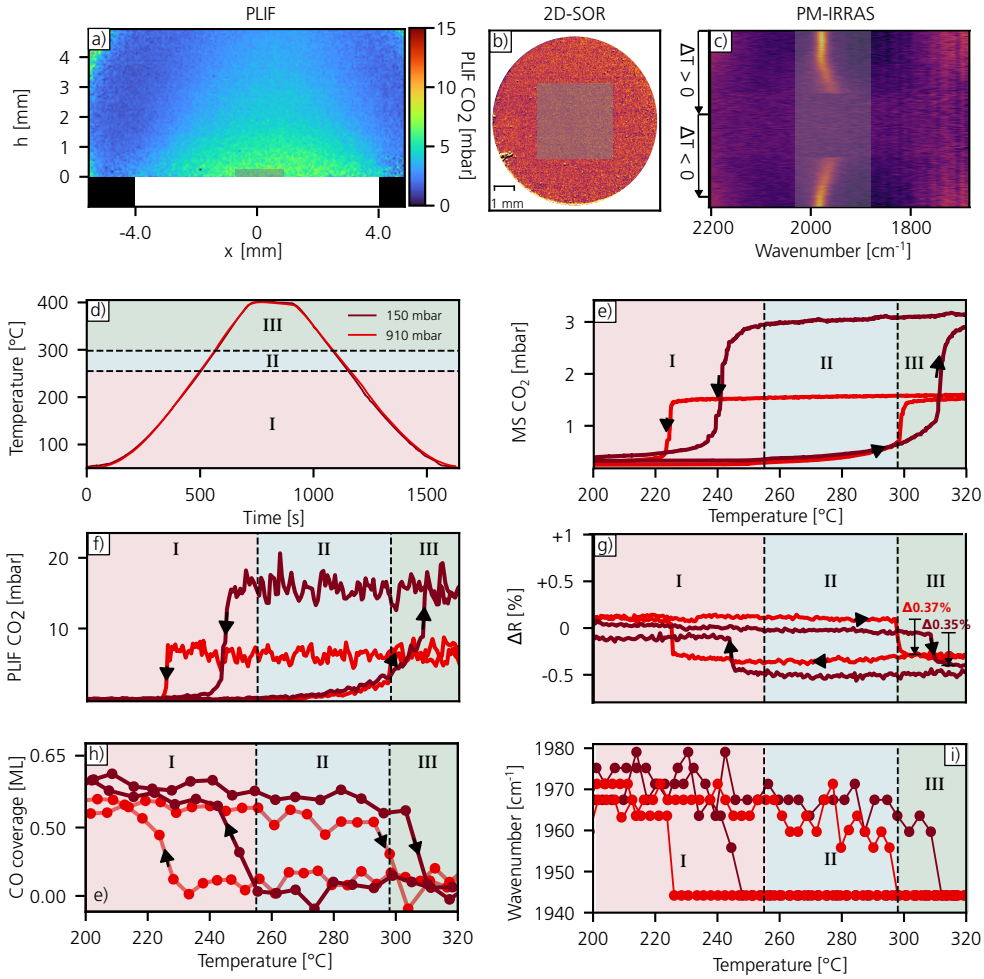

Figure 3.9: Trends of all techniques during CO oxidation at 150 mbar (red) and 910mbar (purple). In a)-c), the data images and spectra for PLIF, 2D-SOR and PM-IRRAS are shown respectively. The grey area indicates the integrated zone to create the trends in d)-i). In d), the temperature ramp over time is shown. The subfigures e), f), g) show the trends from MS, PLIF and 2D-SOR measurements respectively. In h) and i), both the peak area of the ν_{bridge} peak and the central wavenumber of the peak have been plotted as a function of temperature. The reaction regimes I, II and III are highlighted in red, blue and green for each plotted trend.

and the processing of the PM-IRRAS spectra post interferogram acquisition. In our case, two forward-backward scans make up one spectrum resulting in 0.5 s per scan and 1 s per spectrum. The additional processing of the PM-IRRAS spectra in the OPUS software takes another 1-2 s. This process could be parallelized to gain time resolution. Additionally, the setup could be updated to the rapid-scan FT-IR option to achieve ms time resolution, although this comes with a trade-off between sensitivity and resolution.

The MS and PLIF trends in Fig.3.9 e) and f) monitor how the CO_2 gas phase evolves. At the

surface, the local gas concentration measured by PLIF exceeds the global gas composition inside the reactor, measured by MTL, by a factor 5-6. Moreover, one can clearly see that a higher partial pressure of the reactant gas (CO) creates more product gas (CO_2). In this case, PLIF has been used to quantify the product gas at the catalyst surface. This is only possible because of the comparably low partial pressure to remain in the regime where the PLIF intensity evolves linearly as written in equation 2.8. At higher partial pressures, effects like self-adsorption and quenching decrease the fluorescence signal [109, 42]. During MTL, it is striking that the fluctuations in the fluorescence signal are of ± 4 mbar at 910 mbar and ± 1 mbar at 150 mbar. A stronger CO_2 fluorescent signal at 910 mbar leads to stronger fluctuations in laser energy.

While there are significant differences in the gas phase above the catalyst (see paper III), the surface behaviour seems to be rather invariant with the change in pressure. During the light-off, a clear dip in reflectance is observed, measured by 2D-SOR as shown in Fig.3.9 g). As reported using HESXRD [47], this dip coincides with the appearance of the $(\sqrt{5} \times \sqrt{5}\mathrm{R}27^\circ)$ surface oxide indicated by a decrease of $0.3 - 0.4\%$ with an uncertainty of $\pm 0.05\%$. For the PM-IRRAS spectra, the trend of the integrated CO peak based on the grey area in Fig.3.9 c) is shown in Fig.3.9 h). The y-axis has been calibrated to the coverage using the change in central wavenumber presented in Fig.3.9 i).

At both pressures, the extinction of the catalytic activity from regime III to II during the decrease in temperature is indicated by downwards arrows and occurs at a lower temperature than the ignition. This hysteresis behaviour is common and comes from the fact the the environment is CO-rich during the ramp up and oxygen-rich during the ramp down [110]. Here, the hysteresis effect is observed to be larger at lower partial pressure.

During MTL, no PM-IRRAS signal is observed. In previous studies at the same gas ratios at $CO:O_2$ 1:2, similar observations have been made with IR and XPS spectroscopy [64, 52]. We speculate that this disappearance of the PM-IRRAS peak could be due to two main reasons: First, CO has a too low residence time and only weakly adsorbs on the surface oxide leading to a very low coverage of CO on the surface oxide, also confirmed by previous XPS studies [52, 98]. However, it could also be due to the IR signal being lowered by the presence of the oxide. As shown in section 1.2 in chapter 2, PM-IRRAS is based on the enhanced dipole moment perpendicular to the surface which is especially strong for metal surfaces. The reflected IR signals from oxides are lowered by two orders of magnitude. Interestingly, once the O_2 content during CO oxidation was increased (lower $CO:O_2$ ratio), two additional CO adsorption peaks could be observed on Pd-oxide in [64]. This was more closely examined in a combined measurement presented in the next section.

5.1.2 Combined AP-XPS and PM-IRRAS study

In order to understand the relationship between the oxide formation and the lack of any PM-IRRAS signal during oxide formation, AP-XPS and PM-IRRAS have been combined during CO oxidation using an oxygen-rich reaction environment. As mentioned in section 4.2.2 in chapter 2, PM-IRRAS can aid in understanding AP-XPS measurements by assigning several adsorption sites of several species in a single PM-IRRAS spectrum instead of having to measure several AP-XPS core-levels. Moreover, the spectral resolution of the peaks due to their separation in wavenumber facilitates the assignment of adsorption sites [24]. This is why AP-XPS beamlines have chosen to add a (PM-)IRRAS setup to their end-station to enable simulatenous measurements [24, 58]. The measurements presented below are performed at the A-branch of the HIPPIE beamline at the MAX IV laboratory in Lund, Sweden.

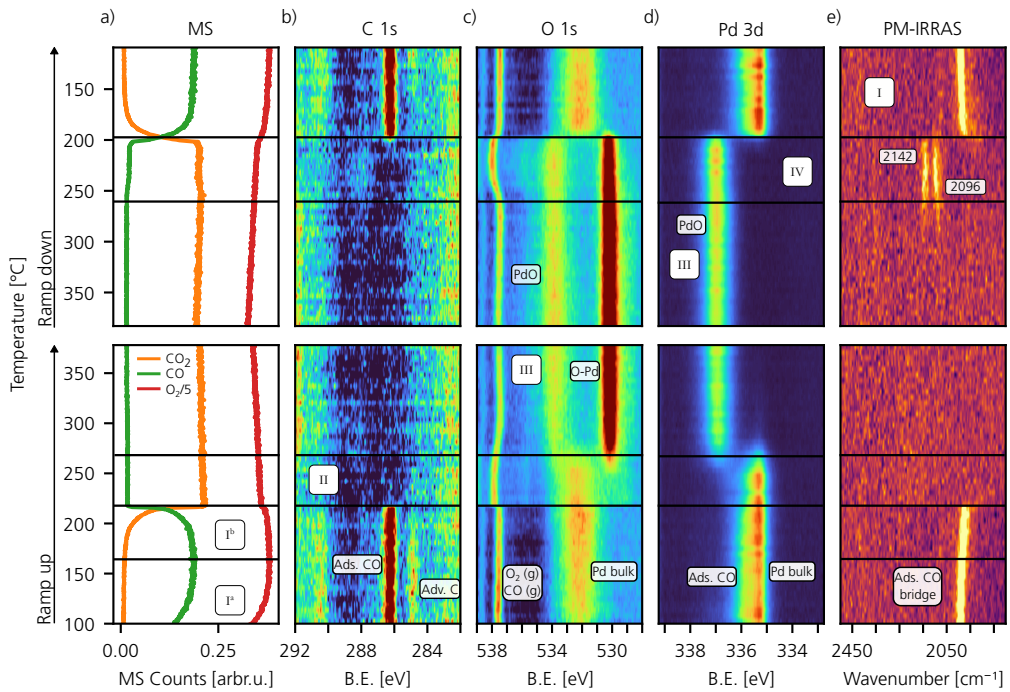

Figure 3.10: Combined AP-XPS and PM-IRRAS spectra during CO oxidation on Pd(100). The simultaneously measured AP-XPS and PM-IRRAS spectra during $CO:O_2$ 1:10 are shown during a temperature ramp from 100 - 400°C. The measurements are supported by MS measurements presented in a) where the reactant gases CO and O_2 and the product gas CO_2 are monitored. In b)-d), the AP-XPS spectra of core-levels C 1s, O 1s and Pd 3d are presented. In e) the PM-IRRAS spectra indicating CO adsorption are shown.

I Similar to the lab-based measurement in Fig.3.9, we observe a CO-poisoned regime (I^a), indicated by a strong CO_{bridge} signal in the PM-IRRAS and C 1s spectra. This

is followed by a kinetic-limited regime where the CO_2 production increases with temperature as shown in the MS trend in Fig.3.10 a). The consumption of CO in I^b can be observed by the shift of the CO_{bridge} to lower wavenumbers in Fig.3.10 e) and the simulatenous drop in the CO MS signal. As previously shown in Fig.3.9, this indicates a drop in CO coverage across the Pd(100) surface.

II Here, the reaction has transitioned into the MTL. This happens at a lower temperature here than in Fig.3.9 due to the high O_2 content and lower CO:O_2 ratio [110]. From the O 1s spectra, it becomes clear that the Pd 3p bulk signal decreases and the signal for Pd 3p PdO and O-Pd increases. At the same time, the signal for adsorbed CO vanishes from the Pd 3d and instead a 2f O-Pd signal appears. There is a shift in the O 1s gas phase by +0.5 eV that originates from a change in the work function of the surface due to a change in coverage [60].

III In this MTL regime that remains constant over a long temperature range, the catalytic activity is limited by diffusion of the CO molecules to the surface. During this period, a thick PdO is formed on the surface which is indicated by a strong peak at 336.7 eV in the Pd 3d including a small component that originates from the surface layer of the PdO [111]. At the same time, a strong peak from 4-fold O atoms can be seen at 530 eV in the O 1s spectra.

IV Most interestingly and different from the results in paper III is the appearance of two new CO adsorption peaks during the ramp down in temperature. These two peaks at 2142 and 2096 cm^{-1} have previously been observed during PM-IRRAS measurements of oxygen-rich CO oxidation on Pd(100) [64]. They also correspond to CO adsorption peaks measured with IRRAS on a several ML thick PdO(101) bulk oxide, grown on a Pd(111) surface in vacuum conditions [94, 95, 112]. Here, they are characterized thanks to support by DFT calculations. Since it has been reported that the PdO(101) also grows on Pd(100), we assume that the measured adsorption sites in Fig.3.10 are identical to the ones reported in literature: The first peak at 2142 cm^{-1} is identified as adsorbed atop-CO on a coordinatively unsaturated (cus) Pd site, referred to as Pd_{cus}/O_{cus}. The second peak at 2096 cm^{-1} is claimed to belong to atop bound CO on Pd_{cus} next to an oxygen vacancy (O_v), named CO-Pd_{cus}/O_v. Interestingly, these peaks only appear on the ramp down and are accompanied by a slight drop in CO_2 production and a rise in CO signal as measured by the MS. At the same time, the re-appearing work function shift of the O_2 gas phase signal in the O 1s spectrum suggests a change in coverage landscape on the sample.

We can conclude that during oxygen-rich conditions, a thick oxide forms and CO adsorbs on this oxide, but merely when the sample temperature decreases. While it has been observed in literature that these peaks appear even during the ramp up [64], the reactor and ramping conditions are different in our case. We postulate that during the ramp up, the

change in temperature happens quickly due to the exothermic nature of the reaction. This leads to a high reaction rate and CO reacts away immediately on the surface oxide. Whereas on the ramp down, the temperature decrease is slow enough allowing the CO to adsorb. Here, a Mars-van-Krevelen mechanism could be the suggested reaction mechanism.

The presented measurement gives us time-resolved information about the molecular adsorption sites thanks to the PM-IRRAS spectra. While Gao et al. had to speculate about the oxide that CO sits on [64], the combination with AP-XPS provides us with chemical information about oxide formation thanks to the Pd 3d and O 1s PM-IRRAS spectra. However, the presented measurement does not allow us to retrieve structural and spatial resolution across the entire sample to conclude whether this oxide forms homogeneously or in form of islands. It is known from previous studies that the thick oxide grows according to the Stranski-Krastanov growth mode [113, 51]. In that case, the $\sqrt{5}$ surface oxide first covers the Pd(100) surface completely, followed by the PdO(101) growing on top as islands. The combination of AP-XPS and PM-IRRAS is the combination of a point and line-averaging measurement technique. It therefore lacks information about how the activity could vary simulataneously across non-homogeneous surface structures. This can be investigated with the help of imaging and microscopy techniques studying more complex surface structures, such as polycrystalline surfaces that are presented in the upcoming sections.

5.2 CO oxidation on a polycrystalline Pd surface

A random distribution of different surface orientations is achieved through polycrystalline surfaces. Those crystals contain small grains with varying single crystal surface orientations from grain to grain across the entire surface, as previously shown in Fig.3.4. Polycrystals have the potential to serve as an activity-structure library thanks to their variety of different low- and high-index structure terminations [114, 115]. They are positioned right next to each other and can therefore be studied simultaneously under the same reaction conditions. The spatial variance across surface structures suggests that spatially-resolved imaging techniques, such as microscopy-based methods, are suitable to follow their activity.

This has been shown with electron microscopy such as with PEEM and SPEM [116]. However, measurements with these techniques are limited in pressure due to their electron collection nature. A near ambient pressure (NAP)-PEEM has been reported to measure up to maximum 1 mbar. At pressures close to 1000 mbar and beyond, optical microscopy (2D-SOR) serves as a good alternative to observe the change in oxide formation based on a change in sample reflectivity. It can therefore be employed to study oxide formation between different surface orientations (grains) of the polycrystalline surface as presented in paper VI and VII.

Here, an example of a lab-based measurement is presented to introduce how *operando* meas-

urements on polycrystals can be performed and analyzed. A hat-shaped polycrystalline Pd crystal with a diameter of 8 mm and a height of 2 mm has been studied during CO oxidation under oxygen-rich conditions (CO:O_2 1:10). The results in paper VI and VII present a sample with grain sizes varying from 10 to several 100 μm. This increases the amount of grains being studied simultaneously and allows us to create a reflectivity library linked to the surface orientation and the IPF. In the present study, a polycrystalline Pd sample with grain sizes on the order of 1 mm is chosen with an attempt to potentially distinguish the PM-IRRAS spectra.

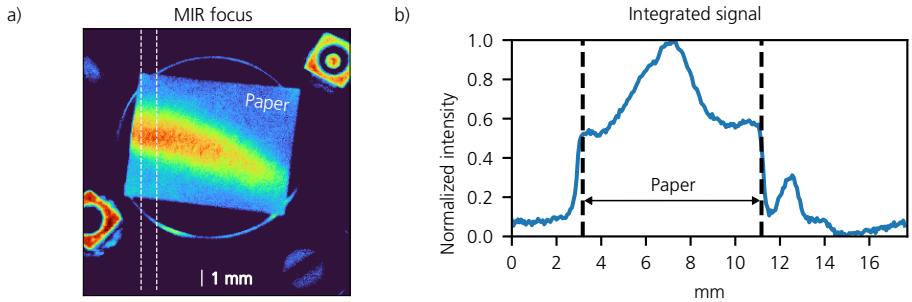

Figure 3.11: PM-IRRAS MIR beam focus visualization. a) The scattered signal from the MIR focus of the PM-IRRAS beam from a white piece of paper of size 8 mm x 10 mm is shown. The white dotted lines define the area that is integrated to show the intensity distribution in b).

On this polycrystal with larger grains, combined 2D-SOR and PM-IRRAS measurements have been performed with the combined optical laboratory setup, supported by MS. 2D-SOR reflectance in Fig.3.12 i)-m) reveals differences in oxide formation for various grains while PM-IRRAS studies the adsorption sites in Fig.3.12 a)-e). In order to know which crystal grains the PM-IRRAS signal comes from, the IR focus is imaged using the MIR camera (Santa Barabara Focalplane) that usually is employed for PLIF measurements, but this time with a different filter. This is shown in Fig.3.11 a). In Fig.3.11 b), the integrated trend of the image in a) between the dotted lines is shown to obtain an estimate of the IR focus which we estimate to be 2 mm at full-width half maximum (FWHM). The direction of where the beam passes is drawn in Fig.3.12 i).

Here, each low-index surface at the IPF extremities, (111), (100) and (110), together with a kinked, A-stepped and B-stepped surface are followed of indices (120), (211) and (431) respectively. Their corresponding regions of interest (ROIs) that lie the ground for the trends in Fig.3.12 h) are drawn onto the 2D-SOR images in Fig.3.12 i)-m).

In previous studies, it has been shown that a small decrease in reflectance can be coupled to the formation of a well-defined ultra-thin surface oxide [47, 46]. The decrease in reflectance can be linked to oxide thickness as explained in paper VII. In the presented data, there are two different decreases in reflectance: First, during the ignition of the catalyst, all grains experiences a small loss in reflectance below 1% and secondly, around 100 s into the MTL,

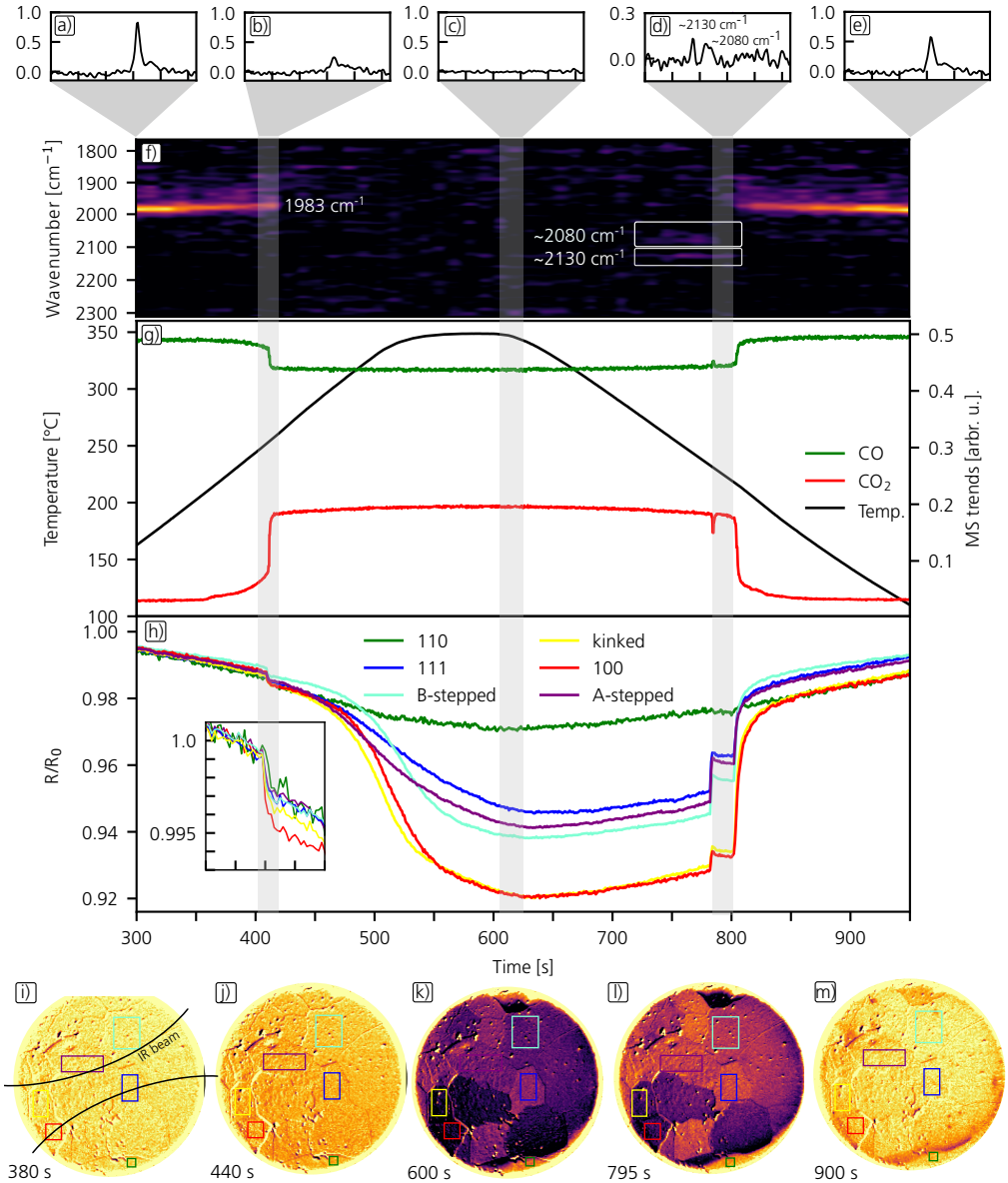

Figure 3.12: Trends and images of a combined PM-IRRAS and 2D-SOR measurement. In f), the PM-IRRAS intensity map across the reaction is shown with several spectra picked at 5 different points in time and temperatures shown in a)-e). In g), the temperature ramp (black) and the CO_2 (red) and CO (green) MS trends are shown. In h), the integrated 2D-SOR trends from ROIs for six different surface structures are shown. The ROIs and their position on the polycrystal are displayed together with the 2D-SOR images in i)-m). The surface orientations chosen are (100), (110), (111), a kinked (120), an A-stepped (211) and a B-stepped (431). These 2D-SOR images are taken at the same reaction times as the PM-IRRAS spectra in a)-e). In i), the beam path of the IR beam is indicated.

a larger loss in reflectance of up to 8 % can be observed. For the zoom-in onto the change in reflectance at the ignition, all trends have been normalized to the trend value at 390 s to more easily compare the drop in reflectance. The (100) surface experiences the largest decrease in reflectance indicating surface oxide and thick oxide formation while the Pd(110) surface experiences the smallest change both during light-off and MTL. This corresponds well to the results mentioned in paper VII. Although there was no surface oxide formation observed for Pd(111) in that paper, we observe a small decrease. According to Lundgren et al. [117], Pd(111) forms a $\sqrt{6}$ surface oxide and can also form a thicker bulk oxide [95]. Similar to paper VII though, the grain close to a Pd(111) surface orientation looses much less in reflectance than the stepped, kinked and surfaces towards Pd(100).

Given the oxygen-rich conditions, we observe thick oxide formation (PdO) similar to the PM-IRRAS and AP-XPS combined measurement on Pd(100) in Fig.3.10. During this formation CO oxidation is limited by gas diffusion to the surface (MTL). The PdO is indicated by a drop in reflectance of close to 10 %. When simulated with equation 2.9, the loss in reflectance for a thick oxide of 5 nm equals -10 % in reflectance. In this case, Pd(100) builds the thickest oxide with a loss of almost 8 %. The most striking result is that the (110) surface sticks out with no significant drop in reflectance which matches previous observations of missing PdO formation on Pd(110) surfaces [118].

While there is a good understanding on how the thick PdO forms, there are various explanations on how the reduced metal reforms [119]. In this configuration, 2D-SOR cannot give us any information about whether there are island-like structures. For this purpose, a combination with a surface structure sensitive technique such as HESXRD would be necessary. During the temperature ramp down, we can observe a small oscillation that leads to a sudden and short increase of CO gas at the surface. Consequently, the sample reduces slightly which is indicated by an increase in reflectance to a plateau before it gets completely reduced. During this period and slightly before the extinction, two CO adsorption sites similar to the data shown in Fig.3.10 are observed. After the plateau, the reflectance continuously increases and the sample reduces to a metal surface which is confirmed by the reflectance reaching similar levels as at the start of the reaction.

When looking at the PM-IRRAS, it is striking that barely any other signal from 300-500 s besides the CO bridge adsorption peak can be seen, similar to the bridge site on Pd(100). If we zoom onto the region between 2000-1900 cm^{-1} in Fig.3.12 a) and e), we can see that there is a broad peak at lower wavenumbers next to the strong CO_{bridge} signal at 1983 cm^{-1}. This signal has been observed at coverages above $\theta = 0.5$ [80, 120] and most likely comes from surfaces close to Pd(111). While one might expect an atop signal from the Pd(111) grains, it has been shown that at temperatures from 300 K onwards, only the bridge site signal remains [80]. This site is also dominant at a coverage of $0.5-0.6$ ML where it shifts between 1918-1951 cm^{-1} [17]. In order to de-convolute the PM-IRRAS signal, one would need to include the reference spectrum of each single surface structure.

One grain sticks out in the entire reflectance data: The Pd(110) surface. It looses very little reflectance during ignition which we associate to surface oxide formation. Although no loss of reflectance has been reported in paper VII, here, a small dip is osberved which might originate from the fact that the data is not yet corrected for temperature changes. However, it is clear that the Pd(110) inhibites thick oxide formation when compared to the other surface orientations. This is confirmed by Toyoshima et al. [121] and by the measurement in paper VII.

6 CO-NO reaction on Rh(111)

Another study where infrared and X-ray spectroscopy were combined, similar to section 5.1.2, is the reaction of NO and CO on Rh(111). This study forms the base for the results in manuscript IV. By adding NO to the gas mixture, the complexity of the reaction is increased and the interplay of various adsorption sites of CO and NO can be studied. We combined AP-XPS and PM-IRRAS to follow the reaction of CO-NO at 0.6 mbar and at a CO:NO ratio of 5 : 1 at the HIPPIE beamline at MAX IV. The measurement is performed both in fixed and in sweep mode XPS mode. In paper IV, the fixed mode is chosen for the AP-XPS spectra to match the time-resolution of the PM-IRRAS spectra. The sweep mode measurements are presented here to discuss the advantages of combining AP-XPS and PM-IRRAS to assign multiple adsorption sites of NO and CO. The fixed measurements are presented in paper IV where the focus has been to follow different reactions at high time-resolution.

Rhodium catalysts have shown to be very selective towards reducing NO [122, 123]. NO and nitric oxide-containing species are a common undesirable by-product of combustion, also of alternative fuels such as ammonia and hydrogen [124]. IR spectroscopy has been shown useful when investigating the reaction of NO and CO since both molecules have well-assigned IR bands [125]. However, IR spectroscopy is limited to IR-active species. Therefore, the combination with AP-XPS is complementary since it detects atomic species and oxide formation.

Thanks to the PM-IRRAS references in table 3.1 and initial NO adsorption measurements, the three adsorption sites at 1564 cm^{-1}, 1848 cm^{-1} and 2054 cm^{-1} could be identified as 3-fold hollow adsorbed NO (NO_{holl}), atop-adsorbed NO (NO_{top}) and atop adsorbed CO (CO_{top}), respectively. The adsorption sites are well-resolved in the PM-IRRAS spectra with a large distance in wavenumbers between the peaks,

$$|\nu(CO_{top}) - \nu(NO_{top})| = 206\,cm^{-1}$$

compared to the AP-XPS core-level spectra where the difference between NO_{top} and CO_{top} can hardly be resolved in the O 1s spectra. Three reaction regimes can easily be identi-

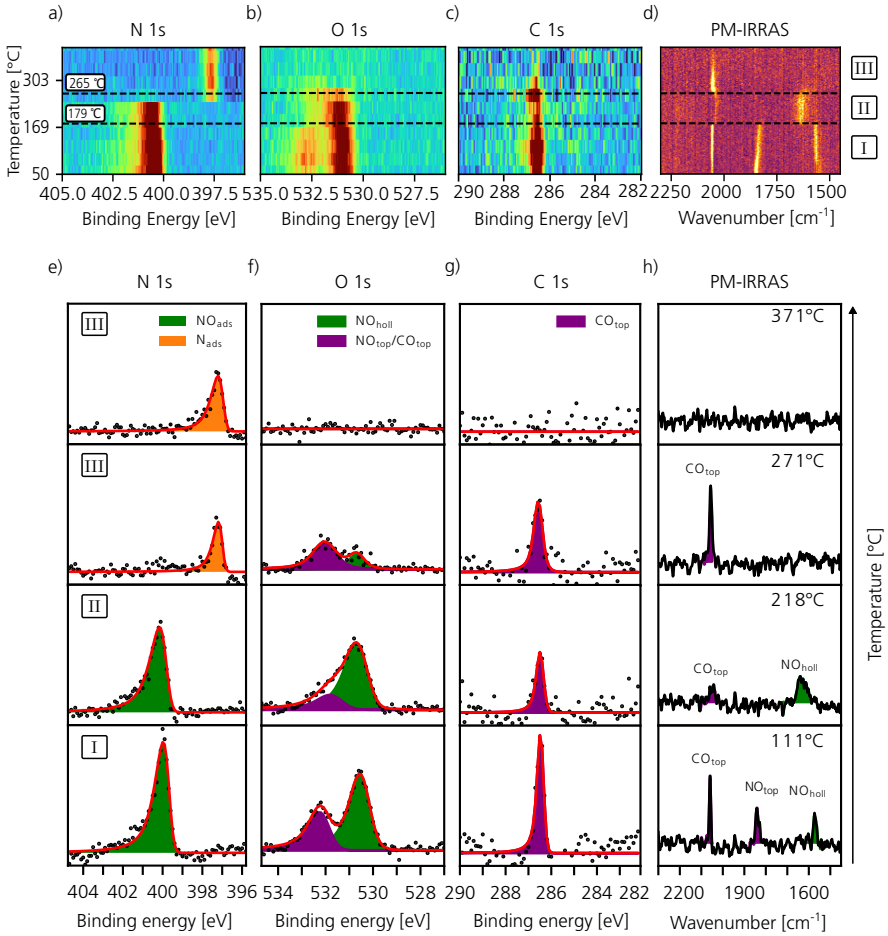

Figure 3.13: Combined AP-XPS and PM-IRRAS measurement of CO-NO reduction on Rh(111). The presented data is taken from a measurement performed at 0.6 mbar total pressure at a CO:NO ratio of 5:1 with a photon energy of 810 eV. In a)-c), the AP-XPS core-levels N 1s, O1s and C1s are depicted respectively. They are measured in sweep mode. In h), an average of 5 PM-IRRAS spectra from the raw data shown in d) are plotted. Each row in e)-h) corresponds to a measurement at a specific temperature increasing from the bottom at 111 °C to the top at 371 °.

fied with the help of the spectral intensity plots in Fig.3.13 a)-d). Starting close to room temperature, during regime I, the surface is covered in both CO and NO. Here, NO dominates the coverage and occupies both atop and hollow sites [126]. From 179 °C onwards in regime II, NO_{top} has desorbed completely, CO_{top} significantly, while NO remains adsorbed on NO_{holl} sites. A change in the NO_{holl} peak towards higher wavenumbers and an increase in width indicates a change in coverage landscape. Finally, NO dissociates shown by the appearance of a N_{ads} signal in the N 1s core-level at lower binding energy. Only CO remains at the surface on atop sites, but slowly desorbs as well. The fact that the atomic oxygen signal is invisible in the O 1s spectrum during regime III has been observed before

and is explained by its rapid consumption through CO to form CO_2[126].

When looking at the AP-XPS spectra, adsorbed NO can both be identified from the combination of N 1s and O 1s spectra and similarly adsorbed CO from the combination of C 1s and O 1s. However, the N 1s does not reveal any details about the adsorption sites due to final state effects [86]. The O 1s AP-XPS core-level spectra reveal two adsorption sites: A hollow and an atop one. However, the signal coming from CO_{top} and NO_{top} overlap which makes it difficult to assign the atop site without any support from the N 1s and C 1s signals. To obtain this information with plain AP-XPS, several core-levels need to be measured which can take up to several minutes for one complete scan in sweep mode. One goal of the measurements presented in paper IV was to follow the reaction time-resolved.

To make the AP-XPS sweep mode measurements comparable to the AP-XPS fixed mode and for calibration purposes, the sweep mode measurements are performed at 1200 eV and some at 810 eV. The same photon energy for all core-levels has been chosen to save time by avoiding the change in photon energy prior to each spectrum collection. This implies, however, a varying kinetic energy for each spectrum and thereby changes the surface sensitivity.

7 Bridging the materials gap with PLIF

While combined measurements have been the main focus of this thesis, some side-turns were taken and the techniques by themselves were explored in various measurements. PLIF has been used to study samples that allow us to bridge the materials gap towards more industrially-alike samples, such as deposited nanoparticles. Two examples that are covered in paper V and VIII are presented below.

7.1 Curved crystals

By cutting and polishing a single crystal, curved crystals can be obtained. Thereby, A-stepped and B-stepped surfaces are exposed in a structured and organized manner along the crystals curvature (see Fig.3.3). The advantage here is that a number of vicinal surfaces including steps and terraces are exposed at the same time to the same conditions. Since the terrace size decreases successively along the curvature of the crystal, well-defined high-index surfaces surrounding the low-index surface along the edge of the IPF figure are exposed .

A variety of studies have shown an asymmetric behaviour during CO adsorption on curved Rh(111) [84], but also during CO oxidation on curved Pd(111)) [127], similar to the study in paper IV. This asymmetry can be explained by earlier CO desorption from B-steps compared to A-steps that remain CO saturated for longer. This results in a lower ignition

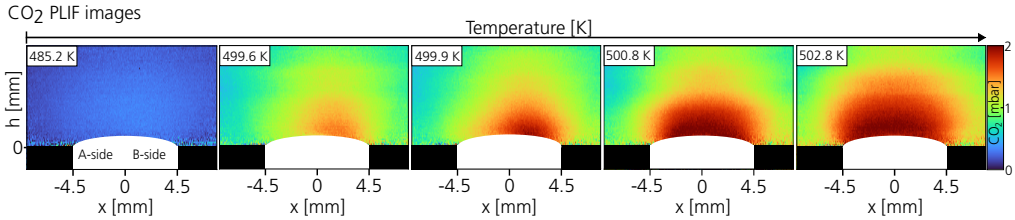

Figure 3.14: **PLIF images of CO oxidation on a curved Rh(111).** Five images around the light-off temperature during CO oxidation on a curved Rh(111) are shown. The B-stepped surfaces become active at lower temperatures than the A-stepped surfaces which is shown by an assymmetric CO_2 cloud.

temperature for B-steps than for A-steps which has been explained by a difference in adsorption energy [127]. However, there are examples where the ignition is symmetric as well, such as on curved Pt(111) [128].

Although the MS CO_2 trend shows a two-step ignition separated in time and temperature, it does not provide any spatial information of where the sample becomes active first. For that purpose, PLIF is very suitable as it provides a 2D image of the gas phase across the range of surface orientations. AP-XPS is very useful in gaining chemical information, but it lacks the ability to simultaneously measure both A-stepped and B-stepped surfaces which means that the measurement needs to be repeated at each point. Due to the curved nature of the crystal and the missing depth of field, the current 2D-SOR setup is not suitable to measure changes in reflectance. PM-IRRAS could be an alternative measurement technique if properly aligned along one terrace structure so that the beam can properly reflect off at grazing incidence.

7.2 CO oxidation on Pd and PdCo nanoparticles

Finally, as part of this thesis, the samples that come closest to an industrial catalyst in terms of surface structure are aerosol-based nanoparticles. They are produced with the help of the spark ablation method [73, 129]. Compared to a single crystal surface, these nanoparticles are deposited on a substrate, in this case a silcon waver (see Fig.3.15). There, they are deposited evenly with a specific density given by the number of engineered nanoparticles (ENP) per μm^2.

In the presented experiment, Pd, PdCobolt (PdCo) and Cobolt (Co) nanoparticles were used to study CO oxidation. The mix of a magnetic and catalytic active material (50 : 50) is chosen due to the promising increase in stability and decrease of sintering when so-called nanochains are formed. This can be achieved with the help of a magnetic self-field alignment where the magnetic interaction with Co particles is used. At the same time, Pd nanoparticles are known to be catalytically active. In paper viii, we have shown that the

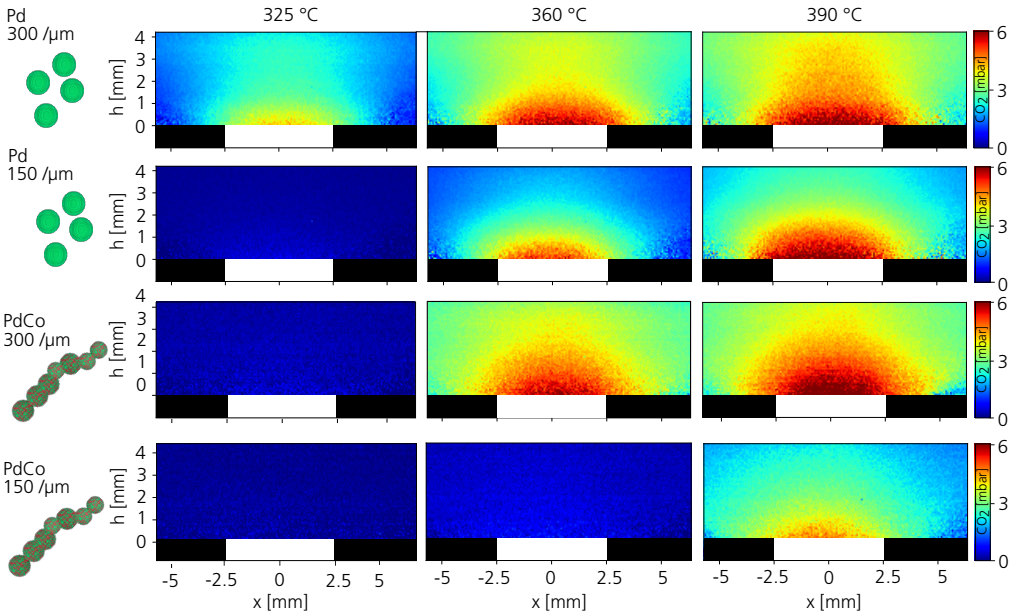

Figure 3.15: Illustration of nanoparticles and overview of catalytic measurements. In a), an illustration of the Pd nanoparticles and PdCo nanochains are shown. In b), the ignition temperature is plotted as measured with PLIF for PdCo and Pd samples of different densities. In c), the MS and PLIF trends for different samples are displayed similar to paper VIII.

addition of Co to the composition of the nanoparticles (NP) does not significantly change their catalytic activity and ensures their stability.

Several samples with different densities were studied: 150 and 300 NP/m^2 Pd and PdCo nanoparticles and 300 NP/m^2 Co. Catalytic measurements with PLIF and MS have been performed to investigate whether the particles are active and how their activity varies with particle density. Here, mainly the amount of produced CO_2 and the light-off temperature are observed.

From Fig.3.15, it becomes clear that the ignition temeprature varies with particle density. For larger particle densities the light-off temperature decreases. When producing PdCo particles, the distribution between Pd and Co is chosen and measured to be close to 50/50 as described in paper VIII. From Fig.3.15, it is striking that the light-off temperature for the sample of 300 ENP/μm^2 PdCo is the same as for 150 ENP/μm^2 Pd. This suggests that it is the amount of Pd that mainly contributes to the catalytic behaviour. The effect of the catalytic reaction on the particles is studied with XPS and SEM, as presented in paper VIII. The particles remain stable in their nanochain structure, but become oxidized which is why they appear larger in the SEM.

Chapter 4

Applications in Electrochemistry

Until here, heterogeneous reactions have been presented at the gas-solid interface. However, heterogeneous reactions can equally occur at the liquid-solid interface [6]. Those reactions form the basis of electrochemical studies. Per definition, electrochemistry is based on the transfer of electrons between a solution and an electrode interface [130].

Electrochemistry lies at the heart of batteries, corrosion and plays an important role in the transition to a sustainable and fossil-free society [131]. In our everyday life, batteries are probably the electrochemical system that we use the most. First invented by Allesandro Volta in 1800, their importance to a CO_2-free emission transportation sector is undeniable. However, batteries have a relatively low energy density compared to other technologies such as fuels [132]. When transitioning to more renewable energy power sources, such as wind and solar, the conversion of electrical energy to chemical energy will be one key technology, both for storage and the extraction of important chemicals. Even in this case, electrochemistry plays an important part as the foundation of water-splitting to obtain hydrogen and oxygen [133].

Corrosion is another phenomenon that motivates part of this thesis work in paper VII as it limits the lifetime of metals in various application causing a great amount cost and a significant carbon footprint [134, 135]. Every Lundastudent has experienced their bike chain getty rusty after a wet autumn; an example of corrosion. If an iron metal object, let's say a screw, corrodes under wet conditions, it oxidizes. Hence, it looses electrons to the electrode that then can be transferred to a species in the electrolyte in contact on another spot on the screw: $\mathrm{Fe} \rightarrow \mathrm{Fe}(2+) + 2e^-$.

For an electrochemical reaction to occur, one needs a medium that transports electrons and another medium that conducts ions. To conduct electrons, metals electrodes are most suitable. As an ionic conductor, an aqueous electrolyte has mainly been used. By using an

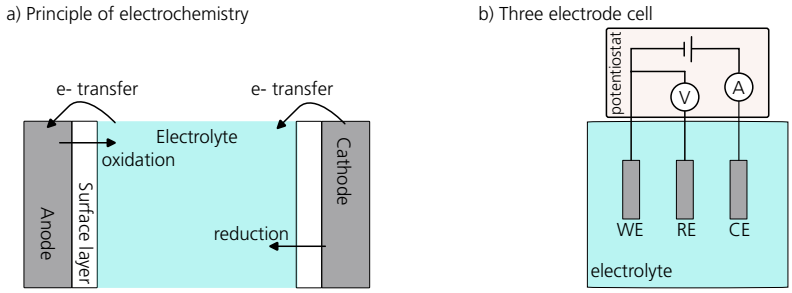

Figure 4.1: Illustration of electrochemical concepts. a) Illustration of a battery/electrochemical reaction b) Illustration of three-electrode electrochemical cell including a working (WE), reference(RE) and counter electrode (CE).

anode that provides electrons and a cathode that receives electrons, a flow of electrons can be insured (see Fig.4.1 a)). Fundamentally, the choice of electrode material and its structure can affect the activity [136]. A more detailed understanding at the atomistic level of how the electrode structure influences the charge transfer can be gaines by studying model systems. These model electrodes consist of a simplified structure and similar to chapter 3, they can come in the form of single crystals, alloyed or polycrystalline metal samples.

Operando and in-situ techniques in electrochemistry are required to study how the electrode surface changes under reaction conditions [137]. These techniques can be based on X-ray interactions, such as XAS, HESXRD and XPS [138, 139] or IR spectroscopy [140]. However, the issue with most of the foremost mentioned techniques is their lack of two-dimensional spatial information about what is happening across the entirety of the surface during the reaction.

Imaging techniques that spatially resolve the reaction become relevant when the reaction no longer behaves homogeneously across the electrode surface. For that purpose, 2D-SOR has been employed as an in-situ technique in fundamental electrochemical studies. Thanks to its sensitivity to very thin layers, structural changes right at the electrode surface can be observed [141]. Other effects such as beam damage and oxygen gas (bubble) formation could also be monitored (see paper x). The use of in-situ 2D-SOR in electrochemical applications is presented in paper vi,ix and x where in the last one, it has been combined with HESXRD.

1 Electrochemical cell

As explained above, a potential difference needs to exist or to be applied to drive a current and thereby an electrochemical reaction. This often takes place in an electrochemical cell that is composed for the following ingredients: An aqueous solution containing an

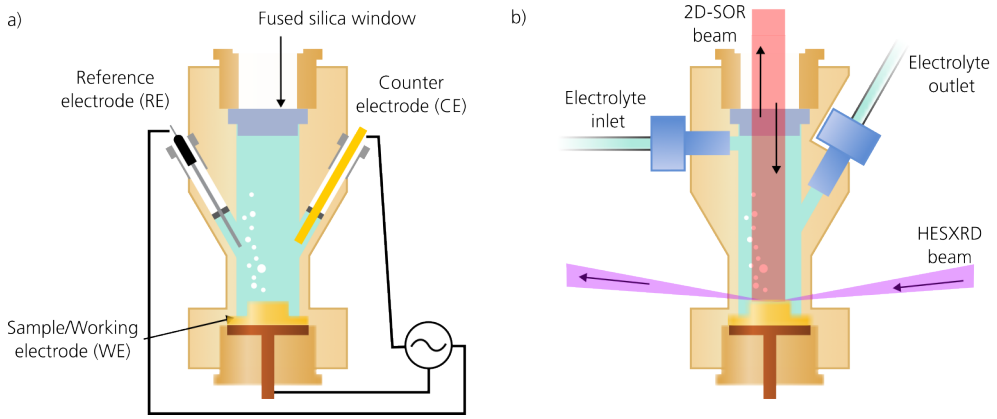

Figure 4.2: Schematic of an electrochemical cell with optical access for 2D-SOR. a) The electrochemical cell includes openings for the RE, the CE and has the sample (WE). The WE is in direct contact with the electrolyte, so is the silicon window that ensures that the 2D-SOR window. Adapted from [141].

electrolyte with ionic species (e.g. H_2SO_4), two/three electrodes and a potentiostat.

The electrochemical cell used in this thesis work is based on a three-electrode cell made of polyether ether ketone (PEEK). It includes an enclosed electrolyte volume, a working electrode (WE), a reference electrode (RE) and a counter electrode (CE). This cell design is chosen because it enable us to more thoroughly control the applied potential (ref). This is achieved thanks to the reference electrode (RE) that is set to a static potential throughout the reaction conditions. The applied potential is therefore chosen in reference to the reference potential at the RE. Here, an Ag/AgCl reference electrode is used, composed of a silver wire inserted into a potassium chloride solution (KCl). The single crystal samples act as a WE in the experiments. In order to get a current flowing and a reaction started, a potential difference needs to be applied between the CE and the WE. At the same time, the reaction window at which we measure looks at the electrolyte-WE interface. The electrolyte is constantly flowing around the cell which is controlled by a peristaltic pump. In order to study how the surface changes with different reaction conditions, the applied potential is varied which can be achieved by a method called Cyclic Voltammetry (CV), presented in the next section.

2 Cyclic Voltammetry

CV measurements are based on the application of a controlled potential and the measurement of the resulting current by a potentiostat between the WE and the CE as indicated in Fig.4.1 b). That way, the electrochemical process occurring in the cell including its stability and present species can be followed [142, 143]. In order to control the potential well and

Table 4.1: Electrochemical cell components used in the different papers as part of this thesis.

Paper	WE	CE	RE	Electrolyte
paper VI	poly-Au/super duplex stainless steel	Gold rod	Ag/AgCl	H_2SO_4
paper IX	Pt(110)/Au(111)/	Pt wire	Ag/AgCl	$0.05 H_2SO_4$
paper IX	Al	Pt wire	Ag/AgCl	Citric Acid + NaOH
paper X	Au(111)	Gold rod	Ag/AgCl	$0.5\ HClO_4$

ensure repeatable measurements, the set potential is applied between the working electrode and a well-defined reference electrode. The word cyclic describes the sweeping of the potential at a continuous rate that is positive at the start (anodic scan) and negative on the way back (cathodic scan). Depending on the scan direction, different electrochemical processes can be studied which is shown in Fig.4.3.

As an example, the four characteristic features throughout a CV scan are explained:

- (1) **Oxygen reduction reaction**: Molecular oxygen that's been forming is reduced to water ($O_2 + 4e^- + 4H^+ \rightarrow 2\,H_2O$)
- (2) **Oxidation**: The surface oxidizes, loosing electrons which is indicated by a negative current.
- (3) **Oxygen evolution reaction**: Molecular oxygen is formed through the presence of the aqueous electrolyte and ions that loose electrons: ($2H_2O \rightarrow O_2 + 4e^- + 4H^+$).
- (4) **Reduction**: The surface reduces and gains electrons, indicated by a positive peak.

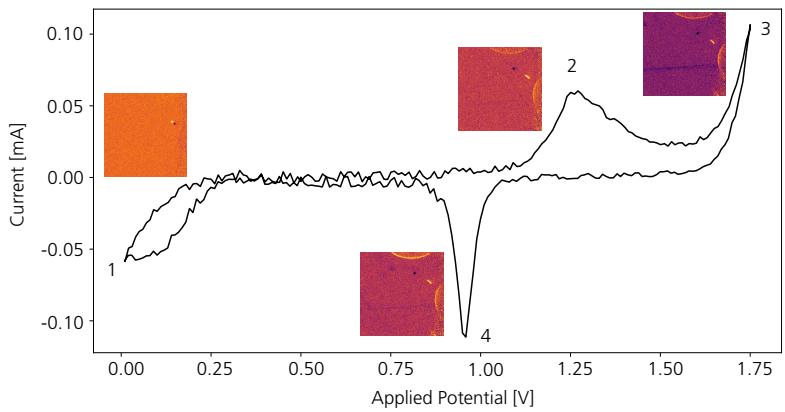

Figure 4.3: **CV scan of a Au(111) sample with a Ag/AgCl reference electrode.** The CV with a scanning potential between 0-1.75 V and the four characteristic features in the CV scan: (1) Oxygen reduction reaction, (2) Oxidation, (3) Reduction and (4) Oxygen evolution reaction

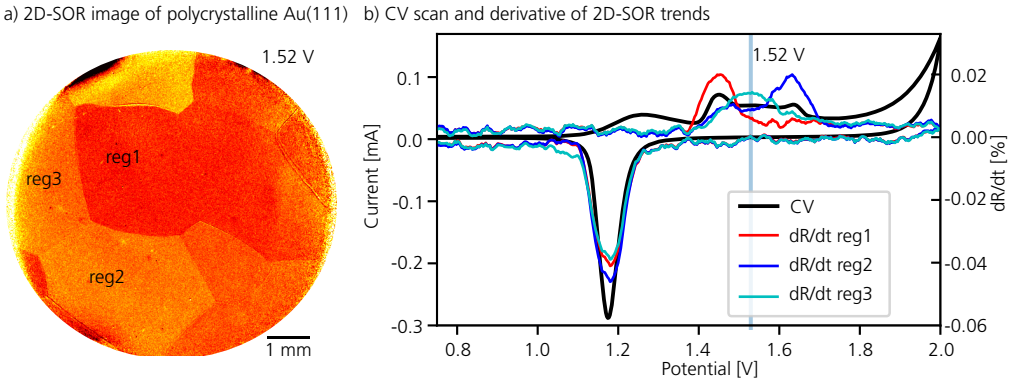

Figure 4.4: 2D-SOR as an in-situ technique for electrochemical studies during a CV scan shown on a polycrystalline Au sample. In a), a 2D-SOR image of a polycrystalline Au sample at 1.52 V is shown. The differently coloured grains indicate differences in reflectivity and therefore oxidation. In b), the CV scan together with the derivative of the 2D-SOR reflectivity over time has been plotted as a function of applied potential for the three indicated regions in a).

3 2D-SOR studies

Thanks to its optical nature and probing wavelength in the visible, 2D-SOR is suitable to track structural changes at a an liquid-solid interface. Several studies report about sensitivity to structural changes down to the level of several Ångströms in electrochemical environments [61, 144]. The change in reflectance can be coupled to structural changes at the surface, shown in all mentioned papers in table 4.1.

During the CV scan of Au(111) in paper IX two points stand out: Point 1 where the reflectance is highest (the sample brightest) and point 4 when it is lowest (the sample darkest) as shown in Fig.4.3. The Au(111) crystal is known to form a Herringbone (HB) reconstruction under cathodic potentials or reducing conditions [145]. This reconstructed surfaces can be seen as flat, tighter arrangements of atoms with a little "lift" of the structure here and there. At that point, the surface atoms are most densely aligned as they accomodate more atoms at the surface. This gives rise to a high reflectance. When reaching OER, the reflectance does not vary much (low $\frac{dR}{dt}$ as reported in paper IX), but it is at its lowest total value. Low reflectance has earlier been shown to indicate surface oxidation, which is also the case here. Moreover, the loss of reflectance could originate from a roughening of the surface during OER which is confirmed by the HESXRD pictures in paper IX that indicate roughening of the surface by powder diffraction rings.

Besides the change in the surface structure, it has become clear from all 2D-SOR electrochemistry studies that the change in reflectance measured with 2D-SOR ($\frac{dR}{dt}$) is proportional the current measured with CV scans. This has been explained in paper VI by stating that the current is representative of the change of the system while 2D-SOR meas-

ures the absolute state of the system. More specifically, the current is representative of the change in charge. From the measurements in paper VI, IX an X, we know that for some processes(oxidation and reduction), the change in reflectivity (R_{SOR}) as a function of applied potential (V) equals the measured current (I) which can be expressed as follows:

$$\frac{dR_{SOR}}{dV} \propto I$$

One could therefore suggest that the SOR reflectivity is proportional to the charge at the surface since $I \propto \frac{dq}{dt}$.

With certainty, the 2D-SOR signal has been shown useful to study surface structural changes and the reduction and oxidation step during CV scans. The advantage is that it is a cheap tool that can be tested in a small laboratory environment where the repetition of measurements is easily possible. Thanks to its compact setup, it can easily be transported and brought to synchrotron facilities and other electrochemical lab environments where it could potentially be combined with other techniques.

Chapter 5

Conclusion and Outlook

This thesis deals with the combination of *operando* techniques to study model catalytic reactions. By combining different techniques, a puzzle of different pieces of information is put together, allowing for a more complete understanding of the reaction mechanism at the gas-solid and liquid-solid interface. This is demonstrated by studying CO oxidation on Pd(100), but also other model catalysts. Especially 2D-SOR has been proven useful when studying non-homogeneous oxide formation and electrochemical systems where the change in reflectance mostly follows the CV scan and is sensitive to structural changes.

A milestone of this thesis work has been to develop a table-top setup where PLIF, PM-IRRAS and 2D-SOR can be combined. This setup is unique in its nature. Having access to a near-ambient pressure cell with different *operando* techniques has several advantages: It gives the chance to repeat measurements a number of times without having to wait for the next beamtime. It is possible to use the techniques in different combined configurations and finally, the setup can be extended in a custom way. For catalytic measurements, it allows us to relate the formation of oxides to changes in the gas phase and in the adsorbate landscape.

In terms of technique development, a noticeable achievement of this thesis has been the use of the 2D-SOR technique in different contexts showing its potential to detect changes on the Ångström level up to spatial resolutions of below 10 μm. Not only have we seen that it is sensitive to the formation of ultra-thin surface oxide layers such as the $\sqrt{5}$ surfac oxide on Pd(100), but also to changes in charge density and conductivity. The unique combination of AP-XPS and PM-IRRAS has laid the ground stone for further investigations at the HIPPIE beamline at Max IV where PM-IRRAS spectra can aid in assigning adsorption sites and species of more complex catalytic reaction.

While the presented results focus on CO oxidation as a reaction to validate the experimental

techniques, the lab-based combined setup can be used to study other reactions. PLIF is species-specific and has been used to monitor the CO_2 gas phase. However, the Nd:Yag system, in combination with a Dye laser, has been shown useful to measure PLIF of several other species such as NH, OH, CO and NO. While CO oxidation and CO-NO reduction are important reactions for emission control and useful when benchmarking experimental setups, they will not solve the increase of CO_2 emission levels that we are facing. Now that the optical setup works, different reactions could be studied, such as CO_2 hydrogenation reactions by monitoring the consumption of CO_2 and also the production of minor species in the process.

At near-ambient pressures, one major result has been to show that the ignition of the catalyst is driven by the gas diffusion from the middle towards the edges of the sample. This result has been achieved thanks to the increase of the camera framerate to 200 Hz and the addition of thermal imaging, spatially resolved by imaging from above the entire catalyst surface. The spatial gas phase imaging from above the surface could be even further explored with PLIF for example on polycrystalline samples to see which grain "ignites" first and how the gas cloud evolves across the different surface orientations, similar to previous studies on curved crystals. This configuration of gas phase imaging might also be interesting to study nanoparticles. The increase to a frame-rate of 200 Hz of the PLIF and 2D-SOR cameras has been crucial in following these events. This highlights once more the need for higher repetition rates and time resolution to follow transient states.

It is no secret that lasers allow for high time resolution up to the femto, but even to the attosecond scale. Since charge and electron dynamics occur at the low femto- to atto-scale, these time scales are required to study these adsorbate dynamics fundamentally [146, 147]. Ultrafast spectroscopy both in in-house laser labs, but also at free electron laser facilities could be a possibility to study transient and precursor states [148]. Ultrafast infrared spectroscopy based on the pump-probe principle has already been used to study monolayer dynamics of molecules on heterogeneous catalyst samples [149].

Compared to 2D-SOR and PLIF, PM-IRRAS has the lowest spatial and temporal resolution in the current setup. This can, however, be improved updating to a fast-scan possibility and also phase-sensitive detection [149]. Thanks to the MIR camera, we are able to track where the IR beam hits the sample. By using apertures, the beam focus width could be narrowed down even further. This opens up for measurements where the entire sample could be scanned by consecutively rotating it, to measure "PM-IRRAS tomography". Another improvement regarding the PM-IRRAS technique as part of the combined setup would be to couple the Q-switch to a trigger signal that initiates the spectral scan in order to more accurately synchronize all the different data sets.

Finally, techniques such as PLIF, with background in combustion diagnostics, have the real advantage of being non-intrusive and long ranged thanks to their laser-based nature. They

have previously been used in optical engines to image the gas flows over time in combustion chambers [150, 151]. There could be a chance to bridge the materials gap for real and try out a similar studies in industrial catalyst beds.

References

[1] Yuping Wu and Rudolf Holze. Surface science in batteries. *Surface and Interface Science*, pages 381–427, 2 2020.

[2] Jihui Wang, Hong Chen, Zhicheng Hu, Mingfa Yao, and Yongdan Li. A review on the pd-based three-way catalyst. *Catalysis Reviews - Science and Engineering*, 57:79–144, 1 2015.

[3] Ronald M. Heck, Robert Farrauto, and Suresh Gulati. *Catalytic Air pollution control commercial technology*. John Wiley and Sons, Inc., 2009.

[4] Collin Smith, Alfred K. Hill, and Laura Torrente-Murciano. Current and future role of haber–bosch ammonia in a carbon-free energy landscape. *Energy and Environmental Science*, 13:331–344, 2 2020.

[5] K. F. Kalz, R. Kraehnert, M. Dvoyashkin, R. Dittmeyer, R.Gläser, U. Krewer, K. Reuter, and J. D. Grunwaldt. Future challenges in heterogeneous catalysis: Understanding catalysts under dynamic reaction conditions. *ChemCatChem*, 9:17–29, 1 2017.

[6] I. Chorkendorff and J. W. Niemantsverdriet. *Concepts of Modern Catalysis and Kinetics*. Wiley-VCH Verlag GmbH & Co., Weinheim, Germany, 10 2013.

[7] Francisco Zaera. In-situ and operando spectroscopies for the characterization of catalysts and of mechanisms of catalytic reactions. *Journal of Catalysis*, 404:900–910, 12 2021.

[8] Feng Gao and D. Wayne Goodman. Model catalysts: Simulating the complexities of heterogeneous catalysts. *Annual Review of Physical Chemistry*, 63:265–286, 4 2012.

[9] Jeong Young Park and Gabor A. Somorjai. Bridging materials and pressure gaps in surface science and heterogeneous catalysis. *Current Trends of Surface Science and Catalysis*, 9781461487425:3–17, 7 2014.

[10] D. Esposito. Mind the gap. *Nature Catalysis 2018 1:11*, 1:807–808, 11 2018.

[11] Miguel A. Bañares. Operando methodology: combination of in situ spectroscopy and simultaneous activity measurements under catalytic reaction conditions. *Catalysis Today*, 100:71–77, 2 2005.

[12] Bert M. Weckhuysen. Determining the active site in a catalytic process: Operando spectroscopy is more than a buzzword. *Phys. Chem. Chem. Phys.*, 2003.

[13] D. Degerman, P. Amann, C. M. Goodwin, P. Lömker, H. Y. Wang, M. Soldemo, M. Shipilin, C. Schlueter, and A. Nilsson. Operando X-ray photoelectron spectroscopy for high-pressure catalysis research using the POLARIS endstation. *Synchrotron Radiation News*, 35:11–18, 2022.

[14] B. L. M. Hendriksen and J. W. M. Frenken. CO oxidation on Pt(110): Scanning tunneling microscopy inside a high-pressure flow reactor. *Physical Review Letters*, 89, 2002.

[15] E. Fabbri, D.F. Abbott, M. Nachtegaal, and T. J. Schmidt. Operando x-ray absorption spectroscopy: A powerful tool toward water splitting catalyst development. *Current Opinion in Electrochemistry*, 5:20–26, 10 2017.

[16] F. C. Meunier. Pitfalls and benefits of in situ and operando diffuse reflectance FT-IR spectroscopy (DRIFTS) applied to catalytic reactions. *Reaction Chemistry and Engineering*, 1:134–141, 3 2016.

[17] Friedrich M. Hoffmann. Infrared reflection-absorption spectroscopy of adsorbed molecules. *Surface Science Reports*, 3:107–192, 1 1983.

[18] Xia Li and Günther Rupprechter. Sum frequency generation spectroscopy in heterogeneous model catalysis: a minireview of co-related processes. *Catalysis Science and Technology*, 11:12–26, 1 2021.

[19] J. Gustafson, M. Shipilin, C. Zhang, A. Stierle, U. Hejral, U. Ruett, O. Gutowski, P. A. Carlsson, M. Skoglundh, and E. Lundgren. High-energy surface X-ray diffraction for fast surface structure determination. *Science*, 343:758–761, 2014.

[20] Louise van Beek, Disha Jain, Pratik Gholkar, Thomas J. Eldridge, Hai P. Nguyen, Kei Muramoto, and Atsushi Urakawa. Spatiotemporal operando uv–vis spectroscopy: Development and mechanistic alternation of co oxidation on pt/al203 on the reactor scale. *Catalysis Today*, 429:114466, 3 2024.

[21] Johan Zetterberg, Sara Blomberg, Jianfeng Zhou, Johan Gustafson, and Edvin Lundgren. Planar laser induced fluorescence applied to catalysis. *Springer Series in Chemical Physics*, 114:131–149, 1 2017.

[22] Willem G. Onderwaater, Andriy Taranovskyy, Gertjan C. Van Baarle, Joost W.M. Frenken, and Irene M.N. Groot. In situ optical reflectance difference observations of CO oxidation over Pd(100). *Journal of Physical Chemistry C*, 121, 2017.

[23] Jianfeng Zhou, Sara Blomberg, Johan Gustafson, Edvin Lundgren, and Johan Zetterberg. Simultaneous imaging of gas phase over and surface reflectance of a pd(100) single crystal during co oxidation. *Journal of Physical Chemistry C*, 121:23511–23519, 10 2017.

[24] Ashley R. Head, Osman Karslıoğlu, Timm Gerber, Yi Yu, Lena Trotochaud, Joseph Raso, Philipp Kerger, and Hendrik Bluhm. CO adsorption on Pd(100) studied by multimodal ambient pressure x-ray photoelectron and infrared reflection absorption spectroscopies. *Surface Science*, 665:51–55, 11 2017.

[25] Stan J. Tinnemans, J. Gerbrand Mesu, Kaisa Kervinen, Tom Visser, T. Alexander Nijhuis, Andrew M. Beale, Daphne E. Keller, Ad M.J. Van Der Eerden, and Bert M. Weckhuysen. Combining operando techniques in one spectroscopic-reaction cell: New opportunities for elucidating the active site and related reaction mechanism in catalysis. *Catalysis Today*, 113:3–15, 3 2006.

[26] Andreas M. Gänzler, Maria Casapu, Alexey Boubnov, Oliver Müller, Sabrina Conrad, Henning Lichtenberg, Ronald Frahm, and Jan Dierk Grunwaldt. Operando spatially and time-resolved X-ray absorption spectroscopy and infrared thermography during oscillatory CO oxidation. *Journal of Catalysis*, 328:216–224, 8 2015.

[27] Vijay K. Velisoju, Shekhar R. Kulkarni, Mengmeng Cui, Abdallah I.M. Rabee, Pasi Paalanen, Jabor Rabeah, Matteo Maestri, Angelika Brückner, Javier Ruiz-Martinez, and Pedro Castaño. Multi-technique operando methods and instruments for simultaneous assessment of thermal catalysis structure, performance, dynamics, and kinetics. *Chem Catalysis*, 3:100666, 8 2023.

[28] Sara Blomberg, Johan Zetterberg, Johan Gustafson, Jianfeng Zhou, Mikhail Shipilin, Sebastian Pfaff, Uta Hejral, Per-Anders Carlsson, Olof Gutowski, Florian Bertram, and Edvin Lundgren. Combining synchrotron light with laser technology in catalysis research. *J. Synchrotron Rad*, 25:1389–1394, 2018.

[29] S Pfaff, J Zhou, U Hejral, J Gustafson, M Shipilin, S Albertin, S Blomberg, O Gutowski, A Dippel, E Lundgren, and J Zetterberg. Combining high-energy X-ray diffraction with surface optical reflectance and planar laser induced fluorescence for operando catalyst surface characterization. *The Review of scientific instruments*, 90, 2019.

[30] P. Pietsch, M. Hess, W. Ludwig, J. Eller, and V. Wood. Combining operando synchrotron X-ray tomographic microscopy and scanning X-ray diffraction to study lithium ion batteries. *Scientific Reports 2016 6:1*, 6:1–10, 6 2016.

[31] Olaf Brummel, Leon Jacobse, Alexander Simanenko, Xin Deng, Simon Geile, Olof Gutowski, Vedran Vonk, Yaroslava Lykhach, Andreas Stierle, and Jörg Libuda. Chemical and structural in-situ characterization of model electrocatalysts by combined infrared spectroscopy and surface X-ray diffraction. *Journal of Physical Chemistry Letters*, 14:8820–8827, 10 2023.

[32] Sebastian Pfaff. On the chemical romance between gas and surface, and how to illuminate it. *Lund Reports on Combustion Physics; (244) (2022)*, 2022.

[33] Jianfeng Zhou. *Operando Gas Imaging in Heterogeneous Catalysis*. PhD thesis, Lund University, 10 2018.

[34] Hanna Karlsson. Calibration measurements in a catalysis reaction chamber using thermographic phosphors, 2015.

[35] Sebastian Pfaff, Hanna Karlsson, Fahed Abou Nada, Edvin Lundgren, and Johan Zetterberg. Temperature characterization of an operando flow reactor for heterogeneous catalysis. *Journal of Physics D: Applied Physics*, 52:324003, 2019.

[36] Sebastian Pfaff, Alfred Larsson, Dmytro Orlov, Gary S. Harlow, Giuseppe Abbondanza, Weronica Linpé, Lisa Rämisch, Sabrina M. Gericke, Johan Zetterberg, and Edvin Lundgren. Operando reflectance microscopy on polycrystalline surfaces in thermal catalysis, electrocatalysis, and corrosion. *ACS Applied Materials and Interfaces*, 13:19530–19540, 4 2021.

[37] Robert G. Greenler. Infrared study of adsorbed molecules on metal surfaces by reflection techniques. *THE JOURNAL OF CHEMICAL PHYSICS*, 44:310–315, 1966.

[38] H. A. Pearce and N. Sheppard. Possible importance of a "metal-surface selection rule" in the interpretation of the infrared spectra of molecules adsorbed on particulate metals; infrared spectra from ethylene chemisorbed on silica-supported metal catalysts. *Surface Science*, 59:205–217, 9 1976.

[39] Gary Attard and Colin Barnes. *Surfaces*. Oxford University Press, 1998.

[40] Robert G. Greenler. Reflection method for obtaining the infrared spectrum of a thin layer on a metal surface. *THE JOURNAL OF CHEMICAL PHYSICS*, 50:28, 1969.

[41] Peter R. Griffiths and James A. De Haseth. *Fourier transform infrared spectrometry*. Wiley-Interscience, 2007.

[42] Alan C. Eckbreth. Laser diagnostics for combustion temperature and species. *Laser Diagnostics for Combustion Temperature and Species*, 1 2022.

[43] Joseph D. Miller, Johannes W. Tröger, Johannes W. Tröger, Sascha R. Engel, Sascha R. Engel, Thomas Seeger, Thomas Seeger, Alfred Leipertz, Alfred Leipertz, Terrence R. Meyer, and Terrence R. Meyer. Ch and no planar laser-induced fluorescence and rayleigh-scattering in turbulent flames using a multimode optical parametric oscillator. *Applied Optics, Vol. 60, Issue 1, pp. 98-108*, 60:98–108, 1 2021.

[44] Z. S. Li, M. Rupinski, J. Zetterberg, Z. T. Alwahabi, and M. Aldén. Mid-infrared polarization spectroscopy of polyatomic molecules: Detection of nascent CO2 and H2O in atmospheric pressure flames. *Chemical Physics Letters*, 407:243–248, 5 2005.

[45] Johan Zetterberg, Sara Blomberg, Johan Gustafson, Jonas Evertsson, Jianfeng Zhou, Emma C. Adams, Per Anders Carlsson, Marcus Aldén, and Edvin Lundgren. Spatially and temporally resolved gas distributions around heterogeneous catalysts using infrared planar laser-induced fluorescence. *Nature Communications*, 2015.

[46] Lisa Rämisch, Sabrina M. Gericke, Sebastian Pfaff, Edvin Lundgren, and Johan Zetterberg. Infrared surface spectroscopy and surface optical reflectance for operando catalyst surface characterization. *Applied Surface Science*, 578:152048, 3 2022.

[47] S Albertin, J Gustafson, J Zhou, S Pfaff, M Shipilin, S Blomberg, L R Merte, O Gutowski, A-C Dippel, J Zetterberg, E Lundgren, and U Hejral. Surface optical reflectance combined with X-ray techniques during gas-surface interactions. *Journal of Physics D: Applied Physics*, 53:224001, 4 2020.

[48] Weronica Linpe, Lisa Rämisch, Giuseppe Abbondanza, Alfred Larsson, Sebastian Pfaff, Leon Jacobse, Johan Zetterberg, Lindsay Merte, Andreas Stierle, Zoltan Hegedues, Ulrich Lienert, Edvin Lundgren, and Gary S. Harlow. Revisiting optical reflectance from Au(111) electrode surfaces with combined high-energy surface X-ray diffraction. *Journal of The Electrochemical Society*, 168:096511, 9 2021.

[49] David J. Griffiths. Introduction to electrodynamics. *Introduction to Electrodynamics*, 6 2017.

[50] Vimal Kumar Jain. *Solid state physics*. Springer, 10 2022.

[51] Mikhail Shipilin, Johan Gustafson, Chu Zhang, Lindsay R. Merte, Andreas Stierle, Uta Hejral, Uta Ruett, Olof Gutowski, Magnus Skoglundh, Per Anders Carlsson, and Edvin Lundgren. Transient structures of PdO during CO oxidation over Pd(100). *Journal of Physical Chemistry C*, 119:15469–15476, 7 2015.

[52] S. Blomberg, M. J. Hoffmann, J. Gustafson, N. M. Martin, V. R. Fernandes, A. Borg, Z. Liu, R. Chang, S. Matera, K. Reuter, and E. Lundgren. In situ x-ray photoelectron spectroscopy of model catalysts: At the edge of the gap. *Physical Review Letters*, 2013.

[53] Petr Kostelník, Nicola Seriani, Georg Kresse, Anders Mikkelsen, Edvin Lundgren, Volker Blum, Tomáš Šikola, Peter Varga, and Michael Schmid. The Pd(100)-(5×5)R27°–o surface oxide: A leed, dft and stm study. *Surface Science*, 601:1574–1581, 3 2007.

[54] Mikhail Shipilin, Uta Hejral, Edvin Lundgren, Lindsay R. Merte, Chu Zhang, Andreas Stierle, Uta Ruett, Olof Gutowski, Magnus Skoglundh, Per Anders Carlsson, and Johan Gustafson. Quantitative surface structure determination using in situ high-energy SXRD: Surface oxide formation on pd(100) during catalytic co oxidation. *Surface Science*, 630:229–235, 12 2014.

[55] Jens Als-Nielsen and Des McMorrow. Elements of modern X-ray physics: Second edition. *Elements of Modern X-ray Physics: Second Edition*, 4 2011.

[56] Uta Hejral, Mikhail Shipilin, Johan Gustafson, Andreas Stierle, and Edvin Lundgren. High energy surface X-ray diffraction applied to model catalyst surfaces at work. *Journal of Physics: Condensed Matter*, 33:073001, 12 2020.

[57] Uta Elisabeth Hejral. *Operando characterization of supported alloy nanoparticles during catalytic CO oxidation by surface sensitive X-ray diffraction*. PhD thesis, Universität Hamburg, 2015.

[58] S. Zhu, M. Scardamaglia, J. Kundsen, R. Sankari, H. Tarawneh, R. Temperton, L. Pickworth, F. Cavalca, C. Wang, H. Tissot, J. Weissenrieder, B. Hagman, J. Gustafson, S. Kaya, F. Lindgren, I. Kallquist, J. Maibach, M. Hahlin, V. Boix, T. Gallo, F. Rehman, G. D'Acunto, J. Schnadt, and A. Shavorskiy. HIPPIE: a new platform for ambient-pressure X-ray photoelectron spectroscopy at the MAX IV laboratory. *urn:issn:1600-5775*, 28:624–636, 2 2021.

[59] Grzegorz Greczynski and Lars Hultman. A step-by-step guide to perform X-ray photoelectron spectroscopy. *Journal of Applied Physics*, 132, 7 2022.

[60] Youngseok Yu, Dongwoo Kim, Hojoon Lim, Geonhwa Kim, Yoobin E. Koh, Daehyun Kim, Kohei Ueda, Satoru Hiwasa, Kazuhiko Mase, Fabrice Bournel, Jean Jacques Gallet, François Rochet, Ethan J. Crumlin, Philip N. Ross, Hiroshi Kondoh, Do Young Noh, and Bongjin Simon Mun. Operando study of pd(100) surface during co oxidation using ambient pressure x-ray photoemission spectroscopy. *AIP Advances*, 9:015314, 1 2019.

[61] Weronica Linpe. *Using Light to Probe Surface Electrochemical Processes*. PhD thesis, Lund University, 2021.

[62] G.C. Bond. *Heterogeneous catalysis - principles and applications*. Oxford Chemistry Series, 1974.

[63] Veronique Van Speybroeck. Following the dynamics of industrial catalysts under operando conditions. *Proceedings of the National Academy of Sciences*, 121:e2319800121, 1 2024.

[64] F. Gao, Y. Wang, Y. Cai, and D. W. Goodman. Co oxidation on pt-group metals from ultrahigh vacuum to near atmospheric pressures. 2. palladium and platinum. *Journal of Physical Chemistry C*, 113:174–181, 2009.

[65] Jacob A. Moulijn and Freek Kapteijn. Monolithic reactors in catalysis: excellent control. *Current Opinion in Chemical Engineering*, 2:346–353, 8 2013.

[66] Valérie Meille. Review on methods to deposit catalysts on structured surfaces. *Applied Catalysis A: General*, 315:1–17, 11 2006.

[67] András Sápi, T. Rajkumar, János Kiss, Ákos Kukovecz, Zoltán Kónya, and Gabor A. Somorjai. Metallic nanoparticles in heterogeneous catalysis. *Catalysis Letters*, 151:2153–2175, 1 2021.

[68] Chi Xiao, Bang An Lu, Peng Xue, Na Tian, Zhi You Zhou, Xiao Lin, Wen Feng Lin, and Shi Gang Sun. High-index-facet- and high-surface-energy nanocrystals of metals and metal oxides as highly efficient catalysts. *Joule*, 4:2562–2598, 12 2020.

[69] Sabine V Auras and Ludo B F Juurlink. Recent advances in the use of curved single crystal surfaces. *Progress in Surface Science*, 96, 2021.

[70] Fernando García Martínez. *Heterogeneous catalysis on curved crystals: CO oxidation on Pt and Rh*. PhD thesis, Universidad del País Vasco, 2022.

[71] T. Maitland and S. Sitzman. *Electron Backscatter Diffraction (EBSD) Technique and Materials Characterization Examples*, chapter 2, pages 41–75. Springer, New York, NY, 2007.

[72] S. I. Wright. Orientation texture. *Encyclopedia of Condensed Matter Physics*, pages 221–233, 1 2005.

[73] S. Schwyn, E. Garwin, and A. Schmidt-Ott. Aerosol generation by spark discharge. *Journal of Aerosol Science*, 19:639–642, 10 1988.

[74] Calle Preger. *Magnetic-field-directed Self-assembly of Multifunctional Aerosol Nanoparticles*. PhD thesis, Lund university, 2020.

[75] Julian R.H. Ross. Surfaces and adsorption. *Heterogeneous Catalysis*, pages 17–45, 1 2012.

[76] George Blyholder. Molecular orbital view of chemisorbed carbon monoxide. *Journal of Physical Chemistry*, 68:2772–2778, 1964.

[77] Emrah Ozensoy and D. Wayne Goodman. Vibrational spectroscopic studies on CO adsorption, NO adsorption CO + NO reaction on Pd model catalysts. *Physical Chemistry Chemical Physics*, 6:3765–3778, 7 2004.

[78] S. Blomberg, J. Zetterberg, J. Gustafson, J. Zhou, C. Brackmann, and E. Lundgren. Comparison of ap-xps and plif measurements during co oxidation over pd single crystals. *Topics in Catalysis*, 59:478–486, 3 2016.

[79] Ryo Toyoshima, Masaaki Yoshida, Yuji Monya, Kazuma Suzuki, Kenta Amemiya, Kazuhiko Mase, Bongjin Simon Mun, and Hiroshi Kondoh. Photoelectron spectroscopic study of co and no adsorption on pd(100) surface under ambient pressure conditions. *Surface Science*, 615:33–40, 9 2013.

[80] Marta Borasio. *Polarization Modulation Infrared Reflection Absorption Spectroscopy on Pd Model Catalysts at Elevated Pressure*. PhD thesis, Freie Universität Berlin, May 2016.

[81] S. Surnev, M. Sock, M. G. Ramsey, P. P. Netzer, M. Wiklund, M. Borg, and J. N. Andersen. CO adsorption on Pd(111): A high-resolution core level photoemission and electron energy loss spectroscopy study. *Surface Science*, 470:171–185, 12 2000.

[82] Emrah Ozensoy and Evgeny I. Vovk. In-situ vibrational spectroscopic studies on model catalyst surfaces at elevated pressures. *Topics in Catalysis*, 56:1569–1592, 7 2013.

[83] F. Gao, Y. Cai, K. K. Gath, Y. Wang, M. S. Chen, Q. L. Guo, and D. W. Goodman. CO oxidation on Pt-group metals from ultrahigh vacuum to near atmospheric pressures. 1. Rhodium. *J. Phys. Chem. C*, 113, 2009.

[84] F.Garcia-Martinez, F. Schiller, S. Blomberg, M. Shipilin, L. R. Merte, J. Gustafson, E. Lundgren, and J. Enrique Ortega. CO chemisorption on vicinal Rh(111) surfaces studied with a curved crystal. *Journal of Physical Chemistry C*, 124:9305–9313, 4 2020.

[85] Ryo Toyoshima, Masaaki Yoshida, Yuji Monya, Kazuma Suzuki, Kenta Amemiya, Kazuhiko Mase, Bongjin Simon Mun, and Hiroshi Kondoh. High-pressure no-induced mixed phase on rh(111): Chemically driven replacement. *Journal of Physical Chemistry C*, 119:3033–3039, 2 2015.

[86] Félix G. Requejo, Eleonore L.D. Hebenstreit, D. Frank Ogletree, and Miquel Salmeron. An in situ XPS study of site competition between CO and NO on Rh(111) in equilibrium with the gas phase. *Journal of Catalysis*, 226:83–87, 8 2004.

[87] W. T. Wallace, Y. Cai, M. S. Chen, and D. W. Goodman. No adsorption and dissociation on rh(111): Pm-iras study. *Journal of Physical Chemistry B*, 110:6245–6249, 3 2006.

[88] R. P. Eischens and W. A. Pliskin. The infrared spectra of adsorbed molecules. *Advances in Catalysis*, 10:1–56, 1 1958.

[89] Iris C.ten Have, Josepha J.G. Kromwijk, Matteo Monai, Davide Ferri, Ellen B. Sterk, Florian Meirer, and Bert M. Weckhuysen. Uncovering the reaction mechanism behind coo as active phase for co2 hydrogenation. *Nature Communications 2022 13:1*, 13:1–11, 1 2022.

[90] Victor E. Henrich and P. A. Cox. The surface science of metal oxides. page 464, 1994.

[91] Vikram Mehar, Helen Edström, Mikhail Shipilin, Uta Hejral, Chengjun Wu, Aravind Kadiri, Stefano Albertin, Benjamin Hagman, Kim von Allmen, Tim Wiegmann, Sebastian Pfaff, Jakub Drnec, Johan Zetterberg, Edvin Lundgren, Lindsay R Merte, Johan Gustafson, and Jason F Weaver. Formation of epitaxial pdo(100) during the oxidation of pd(100). *J. Phys. Chem. Lett*, 14:8499, 2023.

[92] M. Todorova, E. Lundgren, V. Blum, A. Mikkelsen, S. Gray, J. Gustafson, M. Borg, J. Rogal, K. Reuter, J. N. Andersen, and M. Scheffler. The pd(100)–(5×5)r27°-o surface oxide revisited. *Surface Science*, 541:101–112, 9 2003.

[93] V. Mehar, M. Kim, M. Shipilin, M. Van Den Bossche, J. Gustafson, L. R. Merte, U. Hejral, H. Grönbeck, E. Lundgren, A. Asthagiri, and J. F. Weaver. Understanding the intrinsic surface reactivity of single-layer and multilayer pdo(101) on pd(100). *ACS Catalysis*, 8:8553–8567, 9 2018.

[94] Jason F. Weaver, Juhee Choi, Vikram Mehar, and Chengjun Wu. Kinetic coupling among metal and oxide phases during co oxidation on partially reduced pdo(101): Influence of gas-phase composition. *ACS Catalysis*, 7:7319–7331, 10 2017.

[95] Jason F. Weaver, Feng Zhang, Li Pan, Tao Li, and Aravind Asthagiri. Vacancy-mediated processes in the oxidation of co on pdo(101). *Accounts of Chemical Research*, 48:1515–1523, 5 2015.

[96] Johan Gustafson. *Oxidation of some Late Transition Metal Surfaces: Structural Studies from UHV to Atmospheric Pressure*. PhD thesis, Lund University, 2006.

[97] Yimin Li Garbo A. Somorjai. *Surface Chemistry and catalysis*. John Wiley and Sons Inc., New Jersey, 2010.

[98] S. Blomberg, U. Hejral, M. Shipilin, S. Albertin, H. Karlsson, C. Hulteberg, P. Lömker, C. Goodwin, D. Degerman, J. Gustafson, C. Schlueter, A. Nilsson, E. Lundgren, and P. Amann. Bridging the pressure gap in co oxidation. *ACS Catalysis*, 2021.

[99] Rasmus Westerström. *Compound Formation in Model Catalysts*. PhD thesis, Lund University, 2010.

[100] B. Hammer, Y. Morikawa, and J. K. Nørskov. CO chemisorption at metal surfaces and overlayers. *Physical Review Letters*, 76:2141, 3 1996.

[101] Prof.Dr. Wolfgang Demtröder. *Atoms, Molecules and Photons*. Springer Verlag, Heidelberg, 2010.

[102] Sune Svanberg. *Atomic and Molecular Spectroscopy*. Springer-Verlag Berlin Heidelberg, 2004.

[103] Hans Joachim Freund, Gerard Meijer, Matthias Scheffler, Robert Schlögl, and Martin Wolf. CO oxidation as a prototypical reaction for heterogeneous processes. *Angewandte Chemie International Edition*, 50:10064–10094, 10 2011.

[104] T. Engel and G. Ertl. Elementary steps in the catalytic oxidation of carbon monoxide on platinum metals. *Advances in Catalysis*, 28:1–78, 1979.

[105] R. Van Rijn, O. Balmes, A. Resta, D. Wermeille, R. Westerström, J. Gustafson, R. Felici, E. Lundgren, and J. W.M. Frenken. Surface structure and reactivity of pd(100) during co oxidation near ambient pressures. *Physical Chemistry Chemical Physics*, 13:13167–13171, 7 2011.

[106] Ryo Toyoshima and Hiroshi Kondoh. In-situ observations of catalytic surface reactions with soft x-rays under working conditions. *Journal of Physics: Condensed Matter*, 27:083003, 2 2015.

[107] János Szanyi and D Wayne Goodman. CO oxidation on palladium. 1. A combined kinetic-infrared reflection absorption spectroscopic study of Pd(100). *J. Phys. Chem*, 98:2972–2977, 1994.

[108] Matthijs A. Van Spronsen, Joost W.M. Frenken, and Irene M.N. Groot. Surface science under reaction conditions: Co oxidation on pt and pd model catalysts. *Chemical Society Reviews*, 46:4347–4374, 7 2017.

[109] Jianfeng Zhou, S. Pfaff, E. Lundgren, and J. Zetterberg. A convenient setup for laser-induced fluorescence imaging of both co and co2 during catalytic co oxidation. *Applied Physics B: Lasers and Optics*, 123, 3 2017.

[110] Diana Vogel, Christian Spiel, Yuri Suchorski, Adriana Trinchero, Robert Schlögl, Henrik Grönbeck, and Günther Rupprechter. Local catalytic ignition during co oxidation on low-index pt and pd surfaces: A combined peem, ms, and dft study. *Angewandte Chemie International Edition*, 51:10041–10044, 10 2012.

[111] R Westerström, M E Messing, S Blomberg, A Hellman, H Grönbeck, J Gustafson, N M Martin, O Balmes, R Van Rijn, J N Andersen, K Deppert, H Bluhm, Z Liu, M E Grass, M Hävecker, and E Lundgren. Oxidation and reduction of pd(100) and aerosol-deposited pd nanoparticles. *PHYSICAL REVIEW B*, 83:115440, 2011.

[112] N. M. Martin, M. Van Den Bossche, H. Grönbeck, C. Hakanoglu, F. Zhang, T. Li, J. Gustafson, J. F. Weaver, and E. Lundgren. CO adsorption on clean and oxidized Pd(111). *Journal of Physical Chemistry C*, 118:1118–1128, 1 2014.

[113] Nicola Seriani, Judith Harl, Florian Mittendorfer, and Georg Kresse. A first-principles study of bulk oxide formation on pd(100). *Journal of Chemical Physics*, 131:54701, 8 2009.

[114] Yuri Suchorski and Günther Rupprechter. Heterogeneous surfaces as structure and particle size libraries of model catalysts. *Catalysis Letters*, 148:2947–2956, 10 2018.

[115] Marek Trzcinski, Grażyna Balcerowska-Czerniak, and Antoni Bukaluk. Xps studies of the initial oxidation of polycrystalline rh surface. *Catalysts 2020, Vol. 10, Page 617*, 10:617, 6 2020.

[116] P. Winkler, J. Zeininger, Y. Suchorski, M. Stöger-Pollach, P. Zeller, M. Amati, L. Gregoratti, and G. Rupprechter. How the anisotropy of surface oxide formation influences the transient activity of a surface reaction. *Nature Communications 2021 12:1*, 12:1–8, 1 2021.

[117] Edvin Lundgren, Anders Mikkelsen, Jesper N Andersen, Georg Kresse, Michael Schmid, and Peter Varga. Surface oxides on close-packed surfaces of late transition metals. *Journal of Physics: Condensed Matter*, 18:R481, 7 2006.

[118] R. Westerström, C. J. Weststrate, J. Gustafson, A. Mikkelsen, J. Schnadt, J. N. Andersen, E. Lundgren, N. Seriani, F. Mittendorfer, G. Kresse, and A. Stierle. Lack of surface oxide layers and facile bulk oxide formation on pd(110). *Physical Review B - Condensed Matter and Materials Physics*, 80:125431, 9 2009.

[119] C. M. Goodwin, M. Shipilin, S. Albertin, U. Hejral, P. Lömker, H. Y. Wang, S. Blomberg, D. Degerman, C. Schlueter, A. Nilsson, E. Lundgren, and P. Amann. The structure of the active Pd state during catalytic carbon monoxide oxidization. *Journal of Physical Chemistry Letters*, 12:4461–4465, 5 2021.

[120] A. M. Bradshaw and F. M. Hoffmann. The chemisorption of carbon monoxide on palladium single crystal surfaces: Ir spectroscopic evidence for localised site adsorption, 1978.

[121] Ryo Toyoshima, Masaaki Yoshida, Yuji Monya, Kazuma Suzuki, Kenta Amemiya, Kazuhiko Mase, Bongjin Simon Mun, and Hiroshi Kondoh. In situ photoemission

observation of catalytic co oxidation reaction on pd(110) under near-ambient pressure conditions: Evidence for the langmuir-hinshelwood mechanism. *Journal of Physical Chemistry C*, 117:20617–20624, 10 2013.

[122] Tingting Zheng, Bing Lu, Gavin Harle, Dongxia Yang, Chengxiong Wang, and Yunkun Zhao. A comparative study of rh-only, pd-only and pd/rh catalysts. *Applied Catalysis A: General*, 602:117649, 7 2020.

[123] M. Shelef and G. W. Graham. Why rhodium in automotive three-way catalysts? *Catalysis Reviews*, 36:433–457, 8 1994.

[124] S. Mashruk, M. Kovaleva, C.T. Chong, A. Hayakawa, E.C. Okafor, and A. Valera-Medina. Nitrogen oxides as a by-product of ammonia/hydrogen combustion regimes. *Chemical Engineering Transactions*, 89:613–618, 2021.

[125] Dimitris I. Kondarides, Tarik Chafik, and Xenophon E. Verykios. Catalytic reduction of NO by CO over rhodium catalysts: 2. Effect of oxygen on the nature, population, and reactivity of surface species formed under reaction conditions. *Journal of Catalysis*, 191:147–164, 4 2000.

[126] Kohei Ueda, Kazuhisa Isegawa, Kenta Amemiya, Kazuhiko Mase, and Hiroshi Kondoh. Operando nap-xps observation and kinetics analysis of no reduction over rh(111) surface: Characterization of active surface and reactive species. *ACS Catalysis*, 8:11663–11670, 12 2018.

[127] S. Blomberg, J. Zetterberg, J. Zhou, L. R. Merte, J. Gustafson, M. Shipilin, A. Trinchero, L. A. Miccio, A. Magaña, M. Ilyn, F. Schiller, J. Enrique Ortega, F. Bertram, H. Grönbeck, and E. Lundgren. Strain dependent light-off temperature in catalysis revealed by planar laser-induced fluorescence. *ACS Catalysis*, 7:110–114, 1 2017.

[128] F. Garcia-Martinez, C. García-Fernández, J. P. Simonovis, A. Hunt, A. Walter, I. Waluyo, F. Bertram, L. R. Merte, M. Shipilin, S. Pfaff, S. Blomberg, J. Zetterberg, J. Gustafson, E. Lundgren, D. Sánchez-Portal, F. Schiller, and J. E. Ortega. Catalytic oxidation of CO on a curved Pt(111) surface: Simultaneous ignition at all facets through a transient CO-O complex**. *Angewandte Chemie International Edition*, 59:20037–20043, 11 2020.

[129] Maria E. Messing, Kimberly A. Dick, L. Reine Wallenberg, and Knut Deppert. Generation of size-selected gold nanoparticles by spark discharge - for growth of epitaxial nanowires. *Gold Bulletin*, 42:20–26, 2009.

[130] Madalina Ciobanu, Jeremy P. Wilburn, Morgan L. Krim, and David E. Cliffel. Fundamentals. *Handbook of Electrochemistry*, pages 3–29, 1 2007.

[131] Gustavo Acosta-Santoyo, José Treviño-Reséndez, Irma Robles, Luis A. Godínez, and Josué D. García-Espinoza. A review on recent environmental electrochemistry approaches for the consolidation of a circular economy model. *Chemosphere*, 346:140573, 1 2024.

[132] Martin Winter and Ralph J. Brodd. What are batteries, fuel cells, and supercapacitors? *Chemical Reviews*, 104:4245–4269, 10 2004.

[133] Zhi Wei She, Jakob Kibsgaard, Colin F. Dickens, Ib Chorkendorff, Jens K. Nørskov, and Thomas F. Jaramillo. Combining theory and experiment in electrocatalysis: Insights into materials design. *Science*, 355, 1 2017.

[134] R. Bender, D. Féron, D. Mills, S. Ritter, R. Bäßler, D. Bettge, I. De Graeve, A. Dugstad, S. Grassini, T. Hack, M. Halama, E. H. Han, T. Harder, G. Hinds, J. Kittel, R. Krieg, C. Leygraf, L. Martinelli, A. Mol, D. Neff, J. O. Nilsson, I. Odnevall, S. Paterson, S. Paul, T. Prošek, M. Raupach, R. I. Revilla, F. Ropital, H. Schweigart, E. Szala, H. Terryn, J. Tidblad, S. Virtanen, P. Volovitch, D. Watkinson, M. Wilms, G. Winning, and M. Zheludkevich. Corrosion challenges towards a sustainable society. *Materials and Corrosion*, 73:1730–1751, 11 2022.

[135] Gerhardus Koch. Cost of corrosion. *Trends in Oil and Gas Corrosion Research and Technologies: Production and Transmission*, pages 3–30, 1 2017.

[136] David M. Heard and Alastair J.J. Lennox. Electrode materials in modern organic electrochemistry. *Angewandte Chemie International Edition*, 59:18866–18884, 10 2020.

[137] Yao Yang, Yin Xiong, Rui Zeng, Xinyao Lu, Mihail Krumov, Xin Huang, Weixuan Xu, Hongsen Wang, Francis J. Disalvo, Joel D. Brock, David A. Muller, and Héctor D. Abrunã. Operando methods in electrocatalysis. *ACS Catalysis*, 11:1136–1178, 2 2021.

[138] Ida Källquist, Tove Ericson, Fredrik Lindgren, Heyin Chen, Andrey Shavorskiy, Julia Maibach, and Maria Hahlin. Potentials in Li-Ion batteries probed by operando ambient pressure photoelectron spectroscopy. *ACS Applied Materials and Interfaces*, 14:6465–6475, 2 2022.

[139] M. V. Varsha and Gomathi Nageswaran. Operando x-ray spectroscopic techniques: A focus on hydrogen and oxygen evolution reactions. *Frontiers in Chemistry*, 8:497887, 1 2020.

[140] Olaf Brummel, Fabian Waidhas, Udo Bauer, Yanlin Wu, Sebastian Bochmann, Hans Peter Steinrück, Christian Papp, Julien Bachmann, and Jörg Libuda. Photochemical energy storage and electrochemically triggered energy release in the

norbornadiene-quadricyclane system: UV photochemistry and IR spectroelectrochemistry in a combined experiment. *Journal of Physical Chemistry Letters*, 8:2819–2825, 7 2017.

[141] Alfred Larsson. *The Formation and Breakdown of Passive Films on Ni Alloys*. PhD thesis, Lund University, 2023.

[142] Noémie Elgrishi, Kelley J. Rountree, Brian D. McCarthy, Eric S. Rountree, Thomas T. Eisenhart, and Jillian L. Dempsey. A practical beginner's guide to cyclic voltammetry. *Journal of Chemical Education*, 95:197–206, 2 2018.

[143] R. G. Compton and C. E. Banks. *Understanding voltammetry*. World Scientific, 2007.

[144] Alfred Larsson, Mariya Vorobyova, Sebastian Pfaff, Giuseppe Abbondanza, Jinshan Pan, Johan Zetterberg, and Edvin Lundgren. Operando surface optical reflectance microscopy study of corrosion film growth on a Ni-Cr-Mo alloy during anodic polarization. *Journal of Physical Chemistry C*, 127:21871–21877, 11 2023.

[145] Felix Hanke and Jonas Björk. Structure and local reactivity of the au(111) surface reconstruction. *Physical Review B - Condensed Matter and Materials Physics*, 87:235422, 6 2013.

[146] Simon Schreck, Elias Diesen, Martina Dell'Angela, Chang Liu, Matthew Weston, Flavio Capotondi, Hirohito Ogasawara, Jerry Larue, Roberto Costantini, Martin Beye, Piter S. Miedema, Joakim Halldin Stenlid, Jörgen Gladh, Boyang Liu, Hsin Yi Wang, Fivos Perakis, Filippo Cavalca, Sergey Koroidov, Peter Amann, Emanuele Pedersoli, Denys Naumenko, Ivaylo Nikolov, Lorenzo Raimondi, Frank Abild-Pedersen, Tony F. Heinz, Johannes Voss, Alan C. Luntz, and Anders Nilsson. Atom-specific probing of electron dynamics in an atomic adsorbate by time-resolved X-ray spectroscopy. *Physical Review Letters*, 129, 12 2022.

[147] C. Hess, S. Funk, M. Bonn, D. N. Denzler, M. Wolf, and G. Ertl. Femtosecond dynamics of chemical reactions at surfaces. *Applied Physics A: Materials Science and Processing*, 71:477–483, 11 2000.

[148] M. Dell'Angela, T. Anniyev, M. Beye, R. Coffee, A. Föhlisch, J. Gladh, T. Katayama, S. Kaya, O. Krupin, J. LaRue, A. Møgelhøj, D. Nordlund, J. K. Nørskov, H. Öberg, H. Ogasawara, H. Öström, L. G.M. Pettersson, W. F. Schlotter, J. A. Sellberg, F. Sorgenfrei, J. J. Turner, M. Wolf, W. Wurth, and A. Nilsson. Real-time observation of surface bond breaking with an x-ray laser. *Science*, 339:1302–1305, 3 2013.

[149] Jan Philip Kraack and Peter Hamm. Surface-sensitive and surface-specific ultrafast two-dimensional vibrational spectroscopy. *Chemical Reviews*, 117:10623–10664, 8 2017.

[150] Zhenkan Wang, Panagiota Stamatoglou, Marcus Lundgren, Ludovica Luise, Bianca Maria Vaglieco, Arne Andersson, Oivind Andersson, Marcus Alden, and Mattias Richter. Ultra-high speed fuel tracer plif imaging in a heavy-duty optical ppc engine. *SAE Technical Papers*, 2018-April, 2018.

[151] Shubham Garg, Mayank Mittal, Srikrishna Sahu, and V. Lakshminarasimhan. Measurement of fuel distribution in a small pfi spark-ignition engine using tracer plif. *SAE Technical Papers*, 2020-April, 4 2020.

Chapter 6

Summary of scientific publications

Paper I: Infrared surface spectroscopy and surface optical reflectance for operando catalyst surface characterization

L. Rämisch, S.M. Gericke, S. Pfaff, E. Lundgren and J. Zetterberg

This paper presents a new setup and experimental study where PM-IRRAS and 2D-SOR have been combined to study the surface oxide formation and the adsorption during CO oxidation on a Pd(100) surface.

I built the setup, arranged the experimental techniques, the data acquisition software and the data analysis code. I performed the experiments, analyzed the data and wrote the manuscript.

Paper II: Visualizing the Gas Diffusion Induced Ignition of a Catalytic Reaction

S. Pfaff, L. Rämisch, S.M. Gericke, A. Larsson, E. Lundgren and J. Zetterberg

In this paper, PLIF and 2D-SOR imaging of the entire surface are presented during the ignition process. The novelty of the paper is that both cameras were triggered at 200 Hz. This allows us to follow how the gas diffusion from the middle of the sample drives the reaction and the build up of a surface oxide towards the edges of the sample.

I helped to build parts of the control software. I participated in parts of the measurements and the scientific discussion regarding the data analysis. I participated in the discussion and revision

of the data analysis and manuscript.

Paper III: Ambient pressure operando catalytic characterization by combining PM-IRRAS with planar laser-induced fluorescence and surface optical reflectance imaging

L. Rämisch, S. Pfaff, S.M. Gericke, E. Lundgren and J. Zetterberg

This publication presents a combined setup of PM-IRRAS, 2D-SOR and PLIF and a simultaneous study of CO oxidation on Pd(100) with all three techniques. It shows how changes at the surface correlate to changes of the gas phase and how the gas phase becomes influenced with higher pressure compared to the surface.

I set up the experimental techniques and setup, the data acquisition software and the data analysis code. I performed the experiments, analyzed the data and wrote the manuscript.

Paper IV: Combined time-resolved Infrared and X-ray spectroscopic operando studies of NO reactions on Rh(111)

L. Rämisch, R. Temperton, S.M. Gericke, S. Pfaff, E. Lundgren, J. Zetterberg and F. García-Martínez

This manuscript presents a combined time-resolved study of PM-IRRAS and AP-XPS. CO oxidation and the reaction of a CO-NO mixture is used as a benchmark reaction. It shows how well the PM-IRRAS data complements the AP-XPS data in identifying adsorption sites with high sensitivity. Additionally, AP-XPS complements PM-IRARS in identifying oxide formation.

I applied for the beamtime that led to the experiment. I participated in the beamtime and contributed beforehand in the alignment of the PM-IRRAS hardware and the setup of the PM-IRRAS software acquisition. I performed the experiments. I analyzed the data, led the scientific discussion and wrote a major part of the manuscript in close collaboration with F. Garcia-Martinez.

Paper v: Structure Matters: Asymmetric CO Oxidation at Rh steps with Different Atomic Packing.

F. García-Martínez, L. Rämisch, K. Ali, I. Waluyo, R.C. Bodero, S. Pfaff, I.J. Villar-García, A.L. Walter, A. Hunt, V. Pérez-Dieste

This paper presents a PLIF and an AP-XPS study of CO oxidation performed on a curved Rh(111) crystal. It shows that the imaging nature of PLIF aids in understanding the assymmetric gas formation.

I participated in the experiment conception. I set up the experimental setup including the data acquisition. I participated in part of the measurements. I was in charge of an initial data analysis and assisted in the more final data analysis process. I wrote part of the manuscript and revised it. All of this was done in close collaboration with F. Garcia-Martinez.

Paper vi: Operando Reflectance Microscopy on Polycrystalline Surfaces in Thermal Catalysis, Electrocatalysis, and Corrosion.

S. Pfaff, A. Larsson, D. Orlov, G.S. Harlow, G. Abbondanza, W. Linpé, L. Rämisch, S.M. Gericke, J. Zetterberg and E. Lundgren

This paper presents a new method to bridge the material gap by simultaneously studying the different surface grains of a polycrystalline sample. The method used is 2D-SOR and the change in reflectance both for surface and thick oxide formation can be directly correlated to the surface structure using the IFP map.

I have been involved in developing the data acquisition software and the hardware setup. I participated in discussions regarding the data analysis code and data analysis, the revision of the manuscript and the scientific discussion especially regarding the catalytic and electrochemistry measurements.

Paper vii: A Polycrystalline Pd Surface Studied by Two-Dimensional Surface Optical Reflectance during CO Oxidation: Bridging the Materials Gap

S. Pfaff, A. Larsson, D. Orlov, L. Rämisch, S.M. Gericke, E. Lundgren and J. Zetterberg

This paper presents the versatility of the surface optical reflectance in the field of heterogen-

eous catalysis and electrochemistry. It shows that the surface oxide formation of different Pd-grains can be studied simultaneously and compared to the IPF figure to create a reflectance and oxide library.

I assisted with setting up the experiment. I participated in the discussion of the data analysis and interpretation and the manuscript. I revised the manuscript.

viii: Magnetic-field-assisted nanochain formation of intermixed catalytic CoPd nanoparticles

C. Preger, L. Rämisch, S. Blomberg, J. Zetterberg, R. Westerström, M. Messing

This paper presents the synthesis of metal engineered PdCo nanoparticles, their functionality and a proof-of-principle test of their catalytic activity. It reveals how they are synthesized, how they are structured and chemically composed and that they are catalytically active and stable during CO oxidation.

I participated in the conception of the PLIF and MS measurements. I set up the experimental setup including the data acquisition. I participated in the measurements together with C. Preger. I was in charge of the PLIF data analysis and made the PLIF figures. I wrote part of the manuscript.

Paper ix: An electrochemical cell for 2-dimensional surface optical reflectance during anodizaion and cyclic voltammetry

W. Linpé, G.S. Harlow, A. Larsson, G.Abbondanza, L.Rämisch, S. Pfaff, J. zetterberg, J. Evertsson and E.Lundgren

This paper presents the first use of 2D-SOR in an electrochemical context during CV scans. It shows that the change in reflectance follows the measured in current during the potential scan during cycli voltammetry.

I was part of the experiments in our lab and helped especially with setting up the 2D-SOR setup. I revised the manuscript and was part of the scientific discussion.

Paper x: Revisiting Optical Reflectance from Au(111) Electrode Surfaces with Combined High-Energy Surface X-ray Diffraction

W. Linpé, L. Rämisch, G. Abbondanza, A. larsson, S. Pfaff, L. Jacobse, J. Zetterberg, L. Merte, A. Stierle, Z. Hegedues, U. Lienert, E. Lundgren and G.S. Harlow

In this publication, the change of reflectance that we observe during CV scans with 2D-SOR has been coupled to the structural changes at the surface by being combined with HESXRD. We could identify that the 2D-SOR reflectance is sensitive to the formation of a so-called Herringbone reconstruction at the Au(111) surface.

I took the main responsibility in the data analysis. I analyzed both the synchronized HESXRD and 2D-SOR data. I wrote an essential part of the manuscript. I participated in the scientific discussion and revised the manuscript.

Appendix

Appendix: Frequency demodulation

In the lock-in amplifier, the intensity signal at the detector I_D is plit up and passes a Low-Pass-Filter (LPF) and a High-Pass-Filter (HPF). The HPF leaves the the high-frequency signal behind given by

$$I_{AC} = (I_s - I_p)J_2(\delta_0)\cos(2\omega_m t).$$

The modulation signal from the PEM at twice the modulation frequency, given by $A\cos(2\omega_m t)$ is then used to demodulate this signal, by using a multiplexer that multiplies the two signals. A multiplication of two cosine signals leads to the sum of two sine signals, such that

$$I_{AC} \times A\cos(2\omega_m t) = (I_s - I_p)J_2(\delta_0)\cos(2\omega_m t) \times A\cos(2\omega_m t)$$

$$\begin{aligned} I_{AC} \times A\cos(2\omega_m t) &= (I_s - I_p)J_2(\delta_0)\cos(2\omega_m t) \times A\cos(2\omega_m t) \\ &= \frac{1}{2}((I_s - I_p)J_2(\delta_0) \cdot A\cos(2\omega_m t + 2\omega_m t) \\ &\quad + A \cdot (I_s - I_p)J_2(\delta_0)\cos(2\omega_m t - 2\omega_m t)) \\ \{A = 1\} &= \frac{1}{2}\left((I_s - I_p)J_2(\delta_0) \cdot A\cos(4\omega_m t) + (I_s - I_p)J_2(\delta_0)\right) \end{aligned} \tag{1}$$

Now, another LPF is applied which then leaves the following signal in the second channel:

$$I_{ch.2} = (I_s - I_p)J_2(\delta_0)$$

as the channel output. When the division between the two channels is computed to obtain the PM-IRRAS, the second-order Bessel function remains which leads to the Bessel function background of the PM-IRRAs spectra.

Printed by Media-Tryck, Lund 2024 NORDIC SWAN ECOLABEL 3041 0903

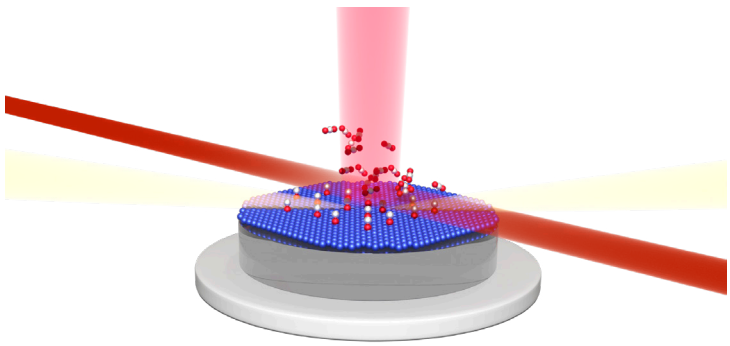

Faculty of Engineering
Department of Physics

LRCP 253
ISBN 978-91-8039-998-2
ISSN 1102-8718